ISSN 8755-6839

SCIENCE OF **TSUNAMI HAZARDS**

Journal of Tsunami Society International

Volume 40 **Number 3** **2021**

WWW.TSUNAMISOCIETY.ORG

TSUNAMI SOCIETY INTERNATIONAL, 1741 Ala Moana Blvd. #70, Honolulu, HI 96815, USA.

SCIENCE OF TSUNAMI HAZARDS is a CERTIFIED OPEN ACCESS Journal included in the prestigious international academic journal database DOAJ, maintained by the University of Lund in Sweden with the support of the European Union. SCIENCE OF TSUNAMI HAZARDS is also preserved, archived and disseminated by the National Library, The Hague, NETHERLANDS, the Library of Congress, Washington D.C., USA, the Electronic Library of Los Alamos, National Laboratory, New Mexico, USA, the EBSCO Publishing databases and ELSEVIER Publishing in Amsterdam. The vast dissemination gives the journal additional global exposure and readership in 90% of the academic institutions worldwide, including nation-wide access to databases in more than 70 countries.

OBJECTIVE: Tsunami Society International publishes this interdisciplinary journal to increase and disseminate knowledge about tsunamis and their hazards.

DISCLAIMER: Although the articles in SCIENCE OF TSUNAMI HAZARDS have been technically reviewed by peers, Tsunami Society International is not responsible for the veracity of any statement, opinion or consequences.

Submit manuscripts of research papers, notes or letters to the Editor. If a research paper is accepted for publication the author(s) must submit a scan-ready manuscript, a Doc, TeX or a PDF file in the journal format. Issues of the journal are published electronically in PDF format. There is a minimal publication fee for authors who are members of Tsunami Society International for three years and slightly higher for non-members. Tsunami Society International members are notified by e-mail when a new issue is available. Permission to use figures, tables and brief excerpts from this journal in scientific and educational works is granted provided that the source is acknowledged.

Recent and all past journal issues are available at: http://www.TsunamiSociety.org CD-ROMs of past volumes may be purchased by contacting Tsunami Society International at postmaster@tsunamisociety.org Issues of the journal from 1982 thru 2005 are also available in PDF format at the U.S. Los Alamos National Laboratory Library http://epubs.lanl.gov/tsunami/

WWW.TSUNAMISOCIETY.ORG

ISSN 8755-6839

SCIENCE OF TSUNAMI HAZARDS

Journal of Tsunami Society International

Volume 40 Number 3 2021

THE PROPOSED DESIGN OF A SMART PARKING AREA AS A MULTIPLE USE BUILDING FOR THE EVENTUAL VERTICAL EVACUATION IN CASE OF TSUNAMI IMPACTS IN SALINAS, ECUADOR

Charli Efrain Del Pino de la Cruz[1], Brayan David Martinez Molina[1], Ana Gabriela Haro Baez[1], Willington Rentería[2], Fabián Rodríguez-Espinosa[1], and Theofilos Toulkeridis[1,3]*

[1] Universidad de las Fuerzas Armadas ESPE, Sangolquí, Ecuador
[2] University of Southern California, Los Angeles, USA
[3] Universidad de Especialidades Turisticas UDET, Quito, Ecuador

*Corresponding author: ttoulkeridis@espe.edu.ec

ABSTRACT

Ecuador is a country with high seismic risk, due to its proximity to the Pacific Ring of Fire. Hereby, strong seismic events are able to occur generating tsunamis, of which an impact may be imminent and whose response time will be short for the evacuation of the population to a safe place. Additionally, there are cities along the Ecuadorian coast that lack safe areas, understood as elevated areas and outside the flood or impact area. Therefore, within the current study in the city of Salinas, we contemplate an architectural and structural multi-hazard proposal, which includes tsunamis and earthquakes, as a multi-use type building that allows the vertical evacuation of the population, as well as the considerations of location, space and height of the building.

Keywords: *Smart parking area, multi-purpose building, vertical evacuation, tsunami, Ecuador*

1. INTRODUCTION

Tsunamis occur with great frequency in the Pacific Ocean due to the geodynamic constellation and the interaction of several tectonic plates (Iwasaki et al., 1992; Sladen et al., 2010; Hagen & Azevedo, 2018; Parwanto & Oyama, 2014). Earthquakes such as tsunamis on the seashore are a severe hazard to human life,

socio-economic activities and as well as strategic infrastructure (Athukorala & Resosudarmo, 2005; Martinez & Toulkeridis, 2020; Plümper et al., 2017; Wong & Said, 2020; Cochard et al., 2008; Navas et al., 2018; Rodriguez et al., 2017; Pararas-Crayannis, 1980; 1983; 1988; 2002; 2013; 2010; 2012; 2014; 2018; Pararas-Crayannis & Zoll, 2017). Therefore, countries such as the United States, implemented a guide for the design of structures capable of resisting seismic events and later the tsunamis caused by the seismic event in order

for these structures to be used as safe zones or vertical evacuation shelters (Park et al., 2012; Mostafizi et al., 2019; Wood et al., 2014; Heintz & Mahoney, 2008).

Ecuador has a high seismic risk, as it is situated along the subduction area of the Nazca oceanic plate with the South American and Caribbean continental plates (Massonne and Toulkeridis, 2012; Acosta, 1983; Gutscher et al., 2000; Padrón et al., 2012; Suhr et al., 2019; Chunga et al., 2019).

Based on the historic record, since the year 1586, some 58 tsunamis were registered in the Ecuadorian coastal profile, of which ten were generated with a nearby source, causing damage and short evacuation times (Chunga & Toulkeridis, 2014, Contreras López, 2013; Rodriguez et al., 2016; Matheus Medina et al., 2016; Toulkeridis et al., 2017; Rodriguez et al., 2017; Chunga et al., 2017). The tsunami hazard is relatively high in Ecuador, since a seismic event is able to cause tsunamis with very short response times for evacuation (Toulkeridis et al., 2017; Edler et al., 2020). Additionally, the small number of natural elevated areas combined with the short evacuation times results for horizontal evacuation to be ineffective (Toulkeridis, 2016; Aviles-Campoverde et al., 2021; Suárez-Acosta et al., 2021).

In Ecuador, several studies have been conducted on tsunamis and their effects, relocations of highly vulnerable areas, vertical evacuations, among other studies of the nature of prevention and mitigation such as resilience to seismic threats and tsunamis on the coast (Toulkeridis et al., 2018; Mato & Toulkeridis, 2018; Celorio-Saltos et al., 2018; Matheus-Medina et al., 2018; Toulkeridis et al., 2019; Toulkeridis et al., 2019; Rentería, 2013).

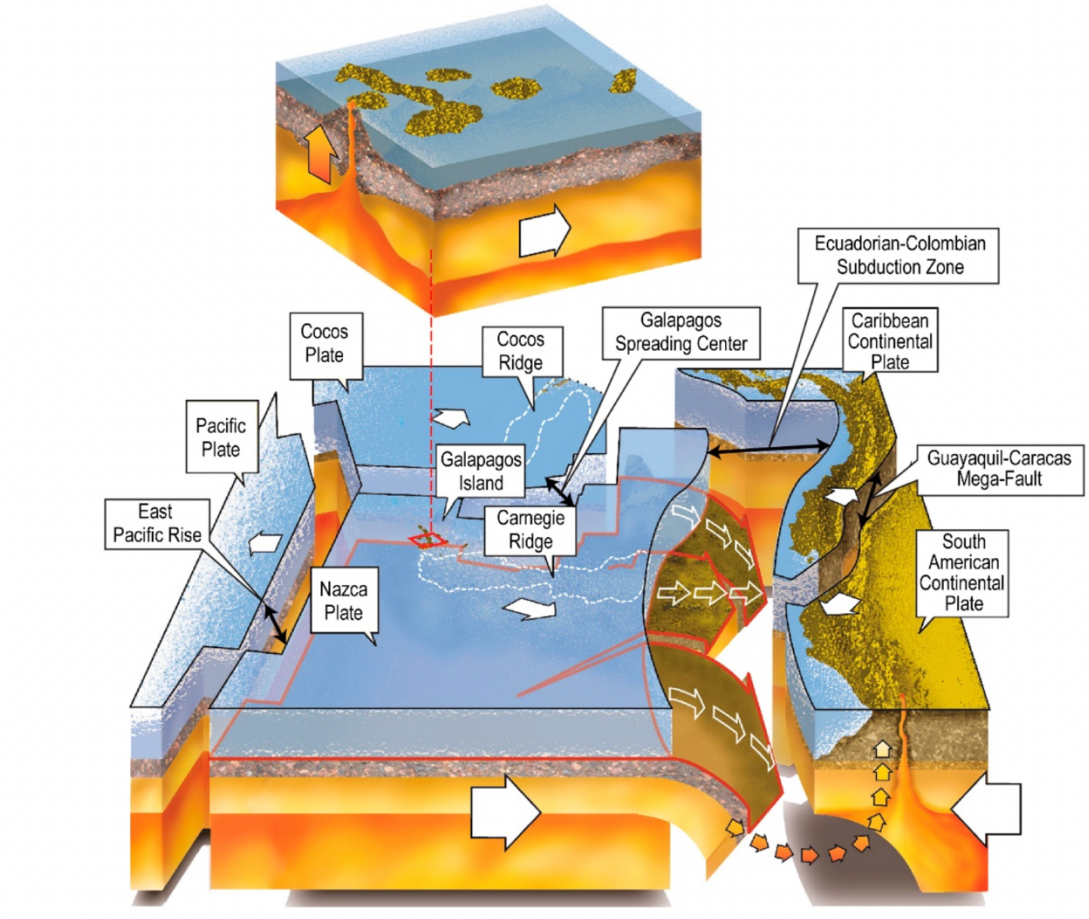

Fig. 1: Geodynamic setting of Ecuador with associated oceanic and continental plates and a variety of plate boundaries, such as the divergent plate boundaries named East Pacific Rise and Galapagos Spreading Center, the convergent plate boundary represented by the Ecuadorian-Colombian Subduction zone, as well as the transcurrent plate boundary represented by the Guayaquil-Caracas Maga-Fault. Also shown the Galapagos Islands and the Carnegie Ridge. Adapted from Toulkeridis, 2013, modified by Toulkeridis et al., 2017.

Based on the aforementioned, the current study analyzed the historical data of earthquakes and tsunamis that occurred in Ecuador, as well as tsunami projections for the city of Salinas. Therefore, the height of potential tsunami waves has been numerically modeled, which served as the basis for the implementation of a smart parking center design, which in turn could serve as a temporary shelter in the event of a necessary vertical evacuation. The same parking center needs to have characteristics of a design that will be able to resist seismic movement and the impact of tsunami waves.

2. STUDY AREA AND NUMERICAL MODELING OF INCOMING WAVE

Salinas is one of the most visited coastal cities by tourists due to its marvelous beaches and modern hotel services. Located in the province of Santa Elena, with a warm climate and low hills, it is a great attraction for domestic as well as international tourists. This last characteristic makes Salinas a highly vulnerable city to the impact of a tsunami because it does not have natural elevated areas. Tsunami risk studies indicate that Salinas is a city with large areas vulnerable to flooding and also with a large influx of people during certain times of the year because it is a highly frequented tourist place (Toulkeridis et al., 2017; Matheus-Medina et al., 2018; Ioualalen et al., 2018). The location of the city of Salinas, and its coastal configuration, expose it to the arrival of tsunamis that could occur throughout the Pacific, so much so that the last two large tsunamis (ie Chile 2010, Japan 2011) arrived at this location, causing strong eddy currents, although they did not cause flooding, these were distant events (Pararas-Carayannis G., 2010; Simons et al., 2011; Norio et al., 2011; Rentería et al., 2012; Lynett et al., 2013).

The only historical record of a local event for the city of Salinas occurred on October 2, 1933 when a strong earthquake off the coast of Santa Elena, caused sea level disturbances, but failed to flood the city (Soloviev, 1984). The historical records are consistent with the GPS observations where a coupling between the tectonic plates cannot be evidenced, however, given the tectonic configuration of the entire region, and the records of paleotsunami events very close to Salinas, experts suggest the possibility of a large earthquake of at least 8.2 Mw. (IOC / UNESCO, 2020).

The characterization of tsunami using numerical models is scarce for this locality. (Renteria, 2007) proposed as a scenario the earthquake of December 12, 1953, of 7.3Mw, located in the Gulf of Guayaquil, and although the simulated disturbances were insignificant, it can be seen how the tsunami covers the entire peninsula, allowing inferring the consequences of a major event. (Ioualalen et al., 2014) proposes a hypothetical scenario of 8.0Mw for the same area, again the effects can be seen in the southern part of the peninsula, although the study does not go into detail about the effects in the city of Salinas. In 2019, INOCAR published a tsunami flood map for the city of Salinas based on a scenario of 8.4Mw in front of the peninsula; this map indicates that the wave height could reach up to 7 meters in some points of the city (INOCAR, 2019).

In this study, a flood map is proposed that considers the rupture plane proposed by the experts (IOC / UNESCO, 2020), and the magnitude proposed by (INOCAR, 2019), that is, 8.4 Mw. For tsunami modeling, the MOST model is used in its ComMIT interface (Titov, et al., 2011). The digital model was built from the topography data of the SIGTIERRAS Program of the Ministry of Agriculture and Livestock of Ecuador, and the bathymetry taken from (Ryan, et al., 2009). The model does not assume any tidal state, and is referred to the mean sea level.

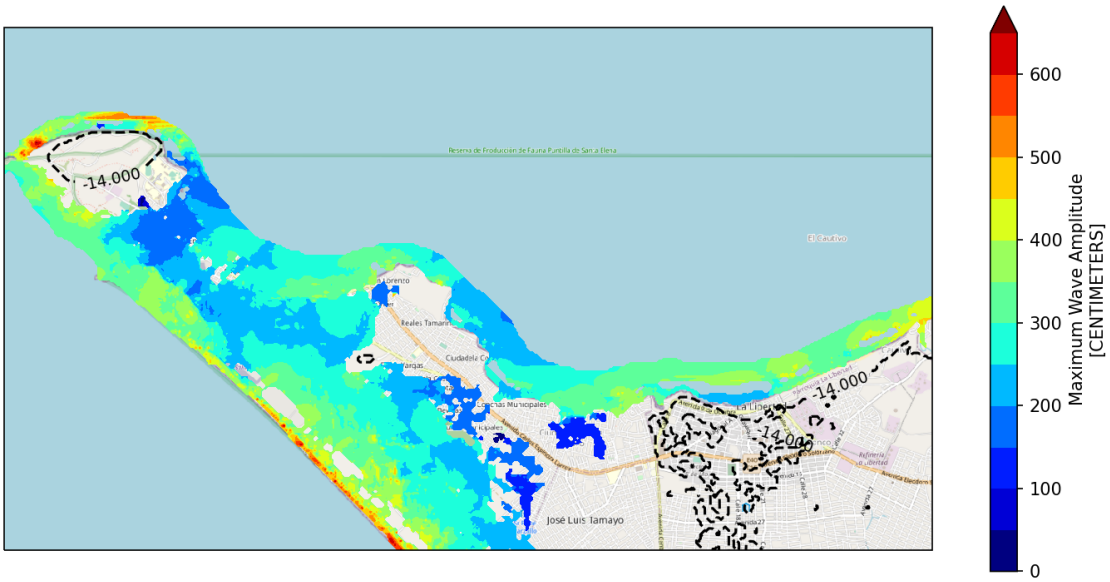

Fig. 2. Tsunami flood map for Salinas, based on an 8.4Mw earthquake off the Santa Elena peninsula.

Figure 2 illustrates the numerical modeling of a tsunami produced by an 8.4Mw earthquake off the Santa Elena peninsula.

The tsunami wave front impacts the peninsula from both the north and south sides, flooding the city of Salinas from both directions. This is an important piece of information for risk management purposes, since under this consideration, the only way out for the population is vertical evacuation and evacuation towards the hill of the Naval Base. It can be seen that some points of the coastline reach heights of up to 6 meters. The depth of flooding within the city, that is, the laminar flow of water, is between 3 and 4 meters, with currents that can fluctuate, within the city between 4 and 6 m / s (Fig. 3).

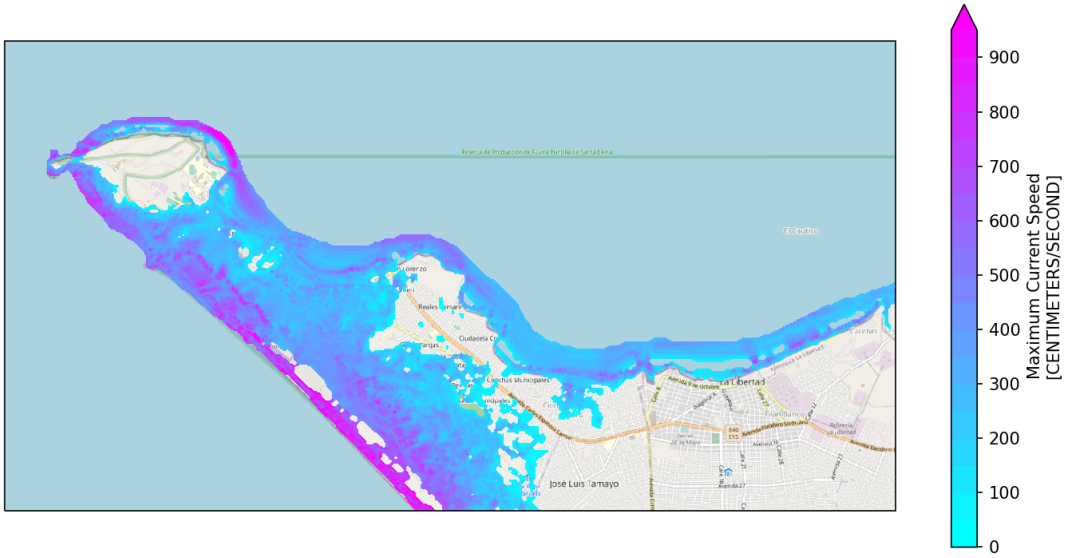

Fig. 3. Tsunami currents map for Salinas, based on an 8.4Mw earthquake off the Santa Elena peninsula.

Previous performed studies appear to project a maximum wave height of up to 6 meters at least for the city of Salinas (Matheus Medina et al., 2016). The results of the current study with modern tools and software, coincides with the height of the tsunami waves of previous studies. Therefore, in the event of a tsunami, the wave would reach the city in an interval of 8 to 12 minutes with an approximate height of 6 meters.

Additionally, like in (Suárez-Acosta et al., 2021), we used the extensively validated tsunami modeling tool, the ComMIT/ MOST model (Community Model Interface for Tsunami), which is an internet-enabled interface to the community tsunami model developed by the NOAA Center for Tsunami Research (NCTR). This interface let one run the MOST model (Method of splitting tsunami), a non-linear shallow water model, which has been extensively, validated from field observations and laboratory experiments (Titov et al., 2011; 2016).

3. METHODOLOGY

A variety of conditions need to be assessed for the design of a structure in the shelter capacity. The distribution of shelters must also be considered, considering evacuation routes and the maximum distance at which the shelters should be located. Therefore, the conditions of the site, space and the elevation of the structure are predominant.

3.1 Site

There are several aspects that must be taken into account, among which the availability of space within the city for the implementation of the project, the speed of movement of people to determine the maximum space between shelters, finally, the existence of structures with a level of adequate performance in the face of multi-threat events and the necessary height to be above the flood level.

In Salinas, the study conducted by Matheus Medina et al. (2016) uses existing structures with sufficient height to define safe zone areas for vertical evacuation. Among which, it stands out that zone 7 covered by the Port Royal Place building does not have the capacity for population density in high seasons, with an approximate deficit of 215 people. Therefore, the proposal must be located in this area. In the figure above, the red dot represents available terrain, approximately 20 meters wide by 45 meters long. In which the development of this proposal is proposed and on which the necessary data for the architectural and structural design will be taken.

3.2. Space

The population density of the area and the number of nearby vertical evacuation structures define the space in the structure. To determine the space, it must be taken into account that the structure is a shelter of short duration, since severe wave cycles do not exceed 24 hours. Another fundamental aspect is that the effective area is considered as a percentage of the total area depending on the concentration of furniture or fixed seats. First, the speed of movement of people in an evacuation event must be estimated, which is approximately 3.2 km / h according to FEMA (FEMA, 2019). And knowing the arrival time of the 11-minute wave previously proposed, it can be concluded that the maximum distance between shelters is 1172 meters or 586 meters from any starting point /Matheus Medina et al., 2016).

On the other hand, the shelter must have a capacity of at least the 215 people mentioned above and once it has been determined that the vertical evacuation shelter is of short duration, a value of 0.93 square meters per person can be used to determine the effective area (F. E. M. A., 2019). Therefore, the minimum effective area of the structure should be 199.95 square meters. Finally, the terrace of the structure will not have fixed seats or furniture, so the effective area is considered 85% of the gross area, thus obtaining that the minimum area of the structure must be 235.26 square meters (FEMA, 2019).

3.3. Elevation

The minimum level that the structure must overcome is the projection of wave height plus percentage of variation of wave height and free edge space as security for the refugees (Fig. 4). The wave height projection for Salinas was estimated at 6 meters high. However, there are several conditions that must be met simultaneously for the wave to reach this maximum height. Among the most important characteristics, it must be fulfilled that the epicenter of the generating earthquake must be close and perpendicular to the coastal profile and the magnitude of the earthquake must be greater than 6.9 Mw. Additionally, as recommended, the design flood level coincides with 30% of the flood level (ASCE SEI., 2016; ASCE SEI., 2000). Thus obtaining 7.8 meters of height of the refuge.

Finally, this value must include a free edge. This value must be the largest of 3 meters or the height of one floor. In this particular case, the free edge is 3.42 meters, resulting in a minimum shelter height of 11.22 meters. In conclusion, the proposal must comply with at least 235 square meters of gross area and 11.22 meters in height.

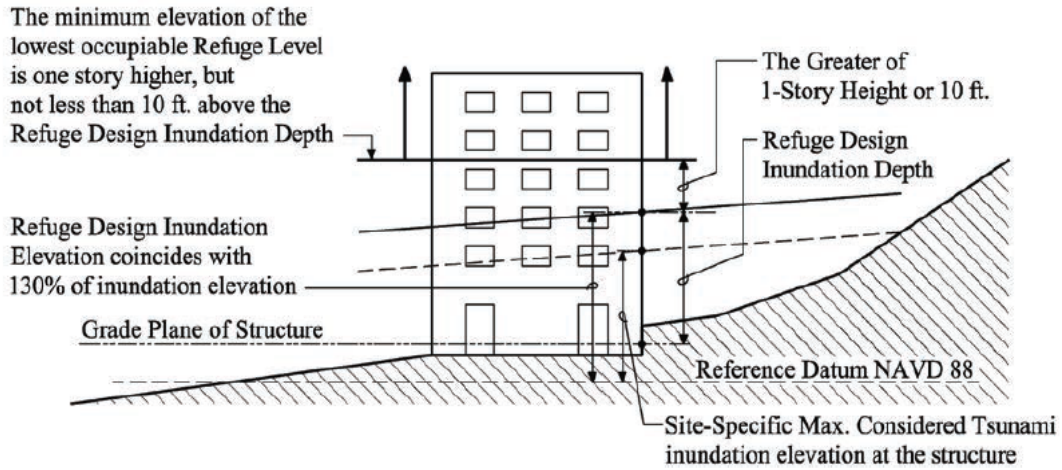

Fig. 4. Elevation consideration (ASCE SEI., 2016).

4. RESULTS AND DISCUSSION

4.1 Architectural proposal

Salinas is a tourist and hotel city, so a parking building or a hotel are ideal to meet the multipurpose objective of the structure, since, the structures will be in permanent use and would allow economic rewards to the city (Fig. 5). For the proposal, the construction of a garage is proposed, since it offers structural security and great performance in the face of multi-threat events (earthquakes and tsunamis).

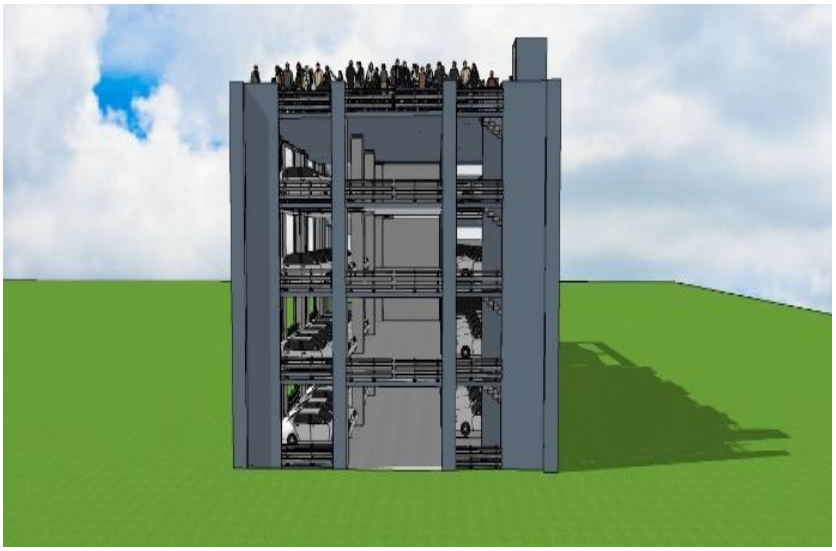

Fig. 5. Architectural proposal, Garage.

As these types of facilities are open structures that allow the free flow of water, making the loads that the building resists due to tsunami actions are significantly lower. Additionally, the vehicle ramps allow an effective vertical evacuation for the large influx of people during the multi-threat event. Once the type of structure to be designed has been defined, it is also necessary to choose the types of vehicles allowed in the parking lot (Fig. 6). The design loads depend on this, and to guarantee a high level of performance, the garage is designed to receive motorcycles and light vehicles, characterized in the following image.

The structure was architecturally designed for the available space presented in section 2.1 with the following layout. The ground floor has space available for 10 light vehicles and 6 motorcycles (Figs. 7, 8).

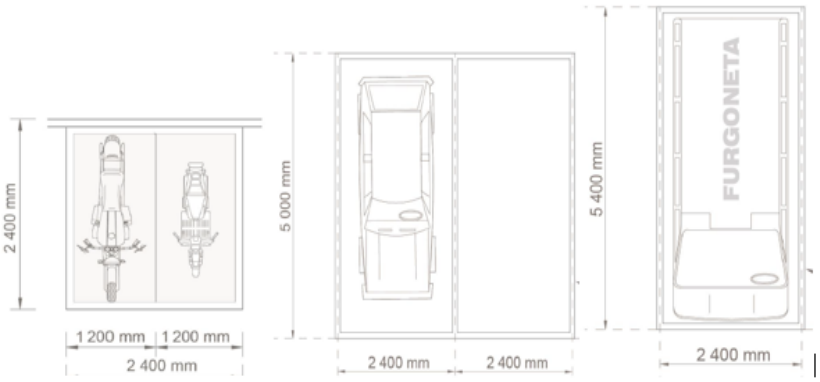

Fig. 6. Types of vehicles (NTE INEN 2248, 2016).

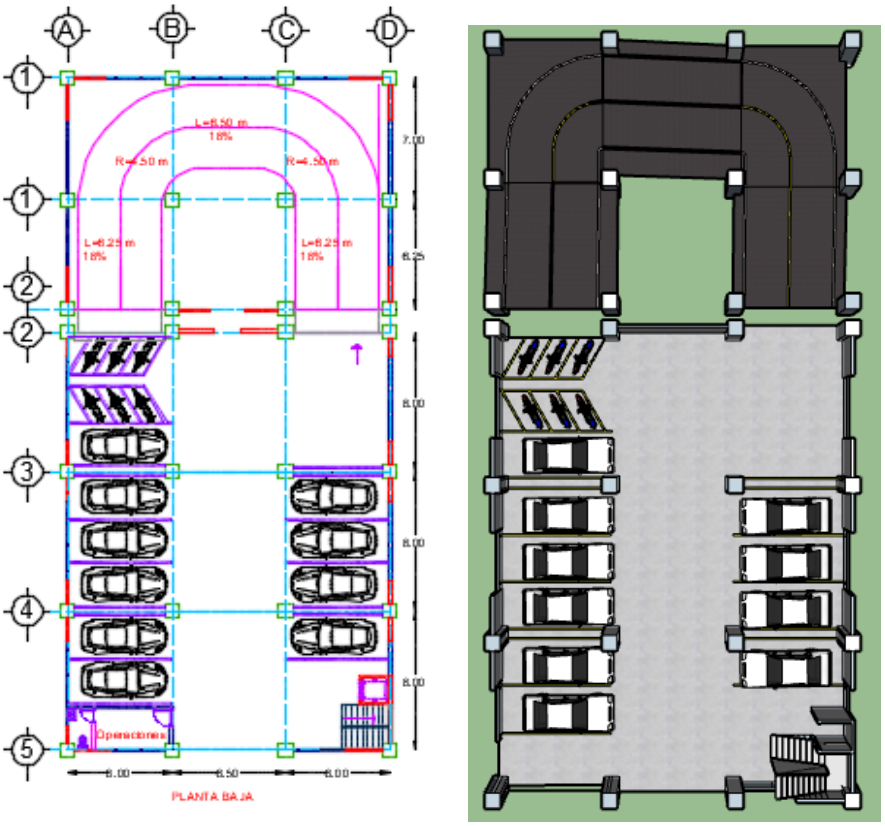

Fig. 7. Layout on the ground floor

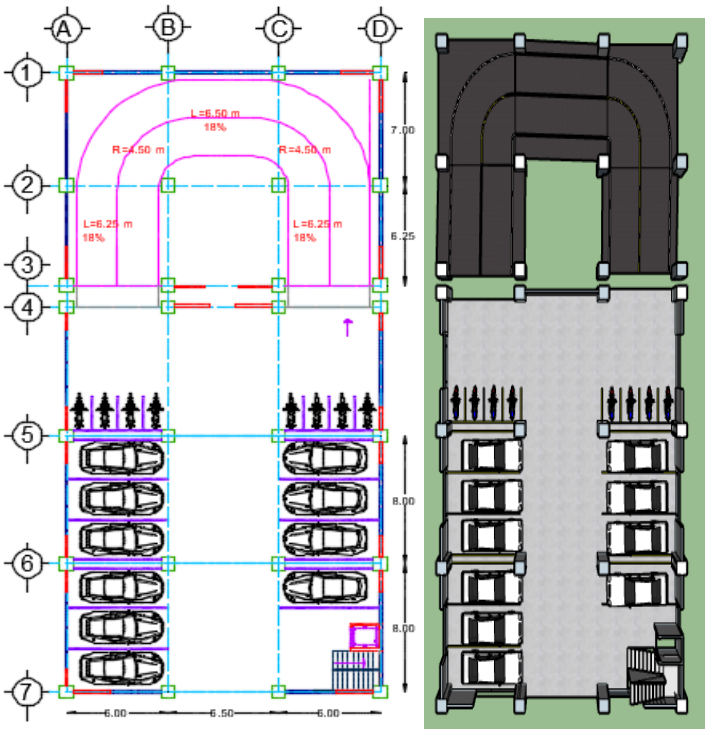

Fig. 8. Distribution in intermediate plants

The intermediate floors have space available for 10 light vehicles and 8 motorcycles. Finally, the upper floor is for the exclusive use as a refuge. And all the space must be free to maximize the number of refugees (Fig. 9).

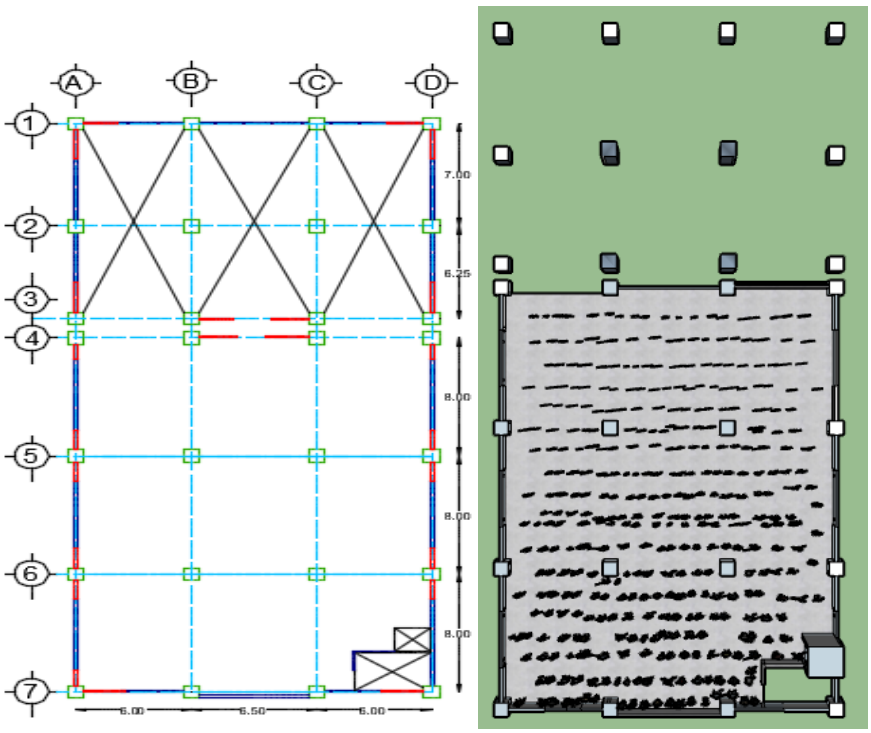

Figure 9. Top floor layout

The architectural proposal is a garage with a dual system of 4 floors and a total height of 13.8 meters; it has a gross area of 424.56 square meters and a capacity for 388 people in the shelter. In addition, it has space for 40 light vehicles, 30 motorcycles (Fig. 10).

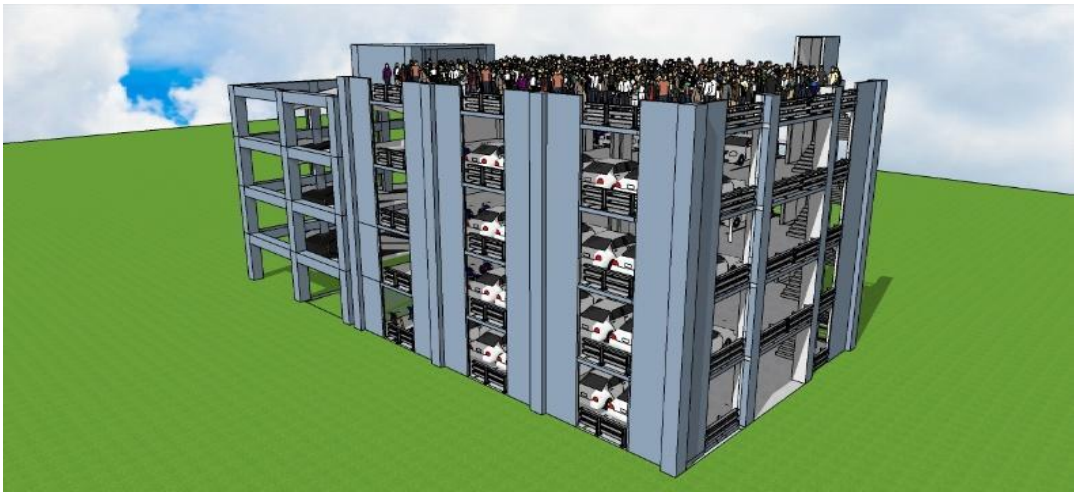

Fig. 10. Final architectural proposal

4.2 Structure design

Once the architectural proposal is established, the respective structural design of the building is conducted with the support of specialized software, which is divided into two blocks. The first consists of ramps for vehicle access and the second is designed on its first three floors for parking and on its upper floor for shelter (Table 1; Fig.11, 12)

Table 1. Types of load for structural design

Type of load	Value	Reference
Live load for parking lots	200 kg/m²	(NEC-SE-CG, 2015)
Live cargo for shelter	480 kg/m²	(ASCE SEI, 2000).
Live load for ladder	480 kg/m²	(NEC-SE-CG, 2015)
Dead load of finishes	100 kg/m²	

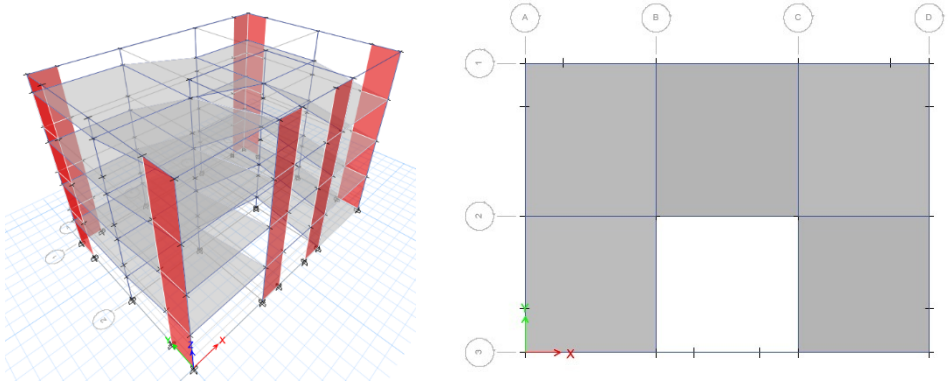

Fig. 11. 3D and plan view of Block 1

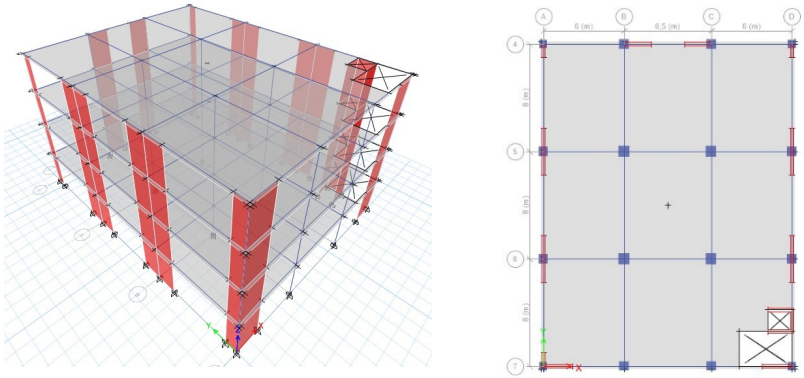

Fig. 12. 3D and plan view of Block 2

Since the structure is multi-purpose, when it is not working as a vertical evacuation shelter, it will be working as a parking lot for vehicles, so different types of cargo are used in its design according to the needs of the structure.

4.3 Performance level

A vertical evacuation structure must meet the levels of operational performance and immediate occupation according to the performance objectives presented by the [45] for both earthquakes and tsunami, this is because the structure must be in good condition. to shelter people seeking to protect themselves from the impact of a tsunami (Fig. 13, 14).

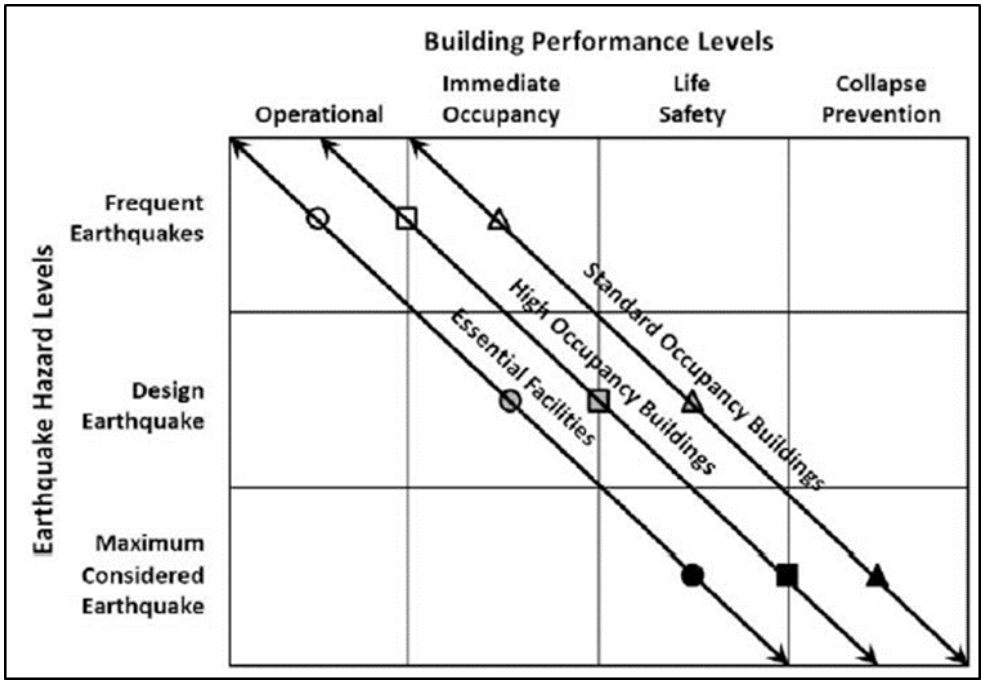

Fig. 13. Performance objectives (FEMA, 2019).

Fig. 14. Tsunami performance targets (FEMA, 2019).

According to the Chilean Association of Seismology and Antiseismic Engineering ACHISINA (2017), it is necessary to have acceptance criteria for essential structures that are at the level of immediate occupation according to the performance objectives. These parameters are classified according to the type of masonry, for the case of ductile masonry the maximum drifts should be 0.7% and for structures with brittle masonry maximum drifts of 0.5% (Fig. 12).

Additionally, certain considerations must be taken for the maximum earthquake considered corresponding to 2500 years, the ASCE SEI. (2000) mentions that the spectrum must be calculated by multiplying the design earthquake corresponding to 475 years by the factor 1.5, and the global acceptance criterion of the structure must be maximum drifts of 1.5% (Fig. 13).

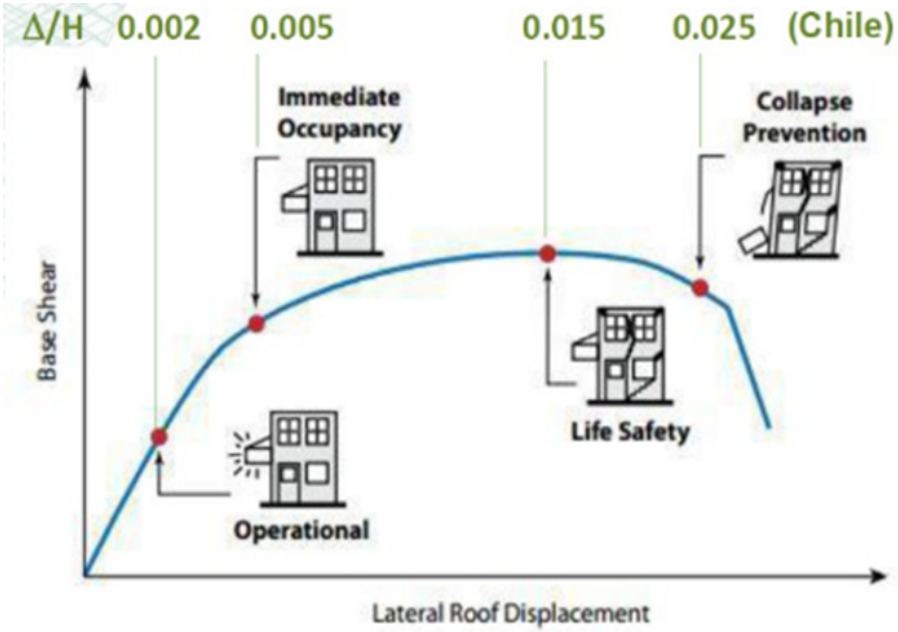

Fig. 15. Drifts for each of the performance levels (ACHISINA, 2017).

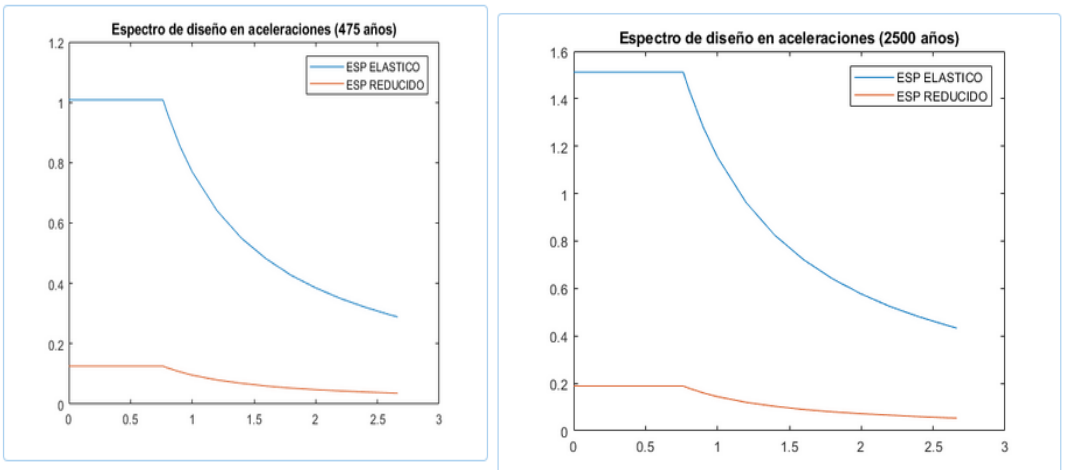

Fig. 16. Design spectra for earthquakes of 475 and 2500 years respectively

4.4 Drift control

The drift control is carried out by applying each of the load combinations with the design spectra for both 475 and 2500, values less than 0.7% and 1.5% respectively must be met in both the X and Y directions of block 1 and 2 (Table 2; Fig. 17).

Table 2. Floor drifts for the 475-year earthquake in Block 1

Float	Load	Drift	Real drift	<0.70%.
1	earthquake X	0.000637	0.38%	Complies
2		0.001065	0.64%	Complies
3		0.001098	0.66%	Complies
4		0.001085	0.64%	Complies
1	earthquake Y	0.000676	0.41%	Complies
2		0.000954	0.57%	Complies
3		0.000977	0.58%	Complies
4		0.000922	0.55%	Complies

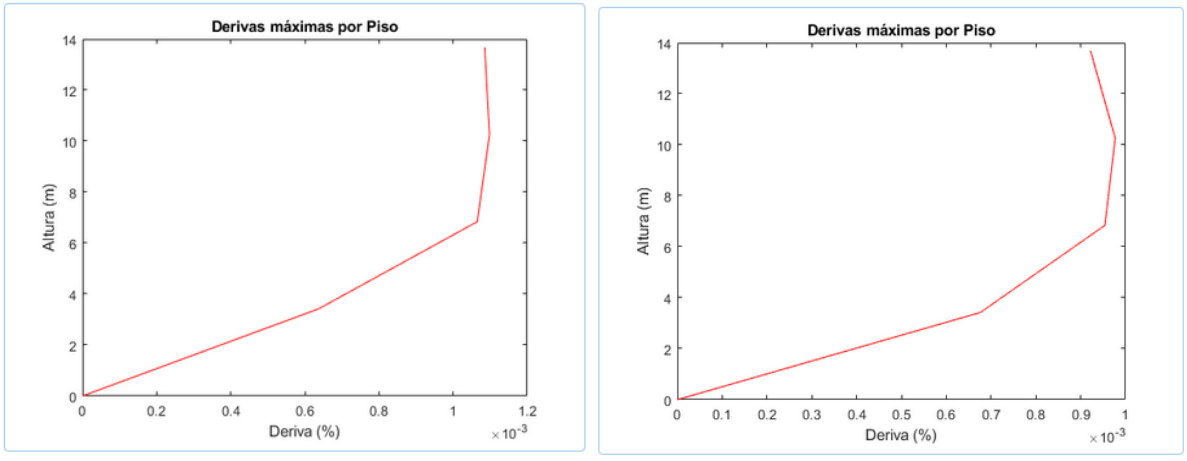

Fig. 17. Drift control in the X and Y direction of Block 1

4.5 Application of tsunami loads

The application of tsunami loads is done according to three cases established by the ASCE (2000), and according to a logical sequence that begins by placing the impact loads and subsequently the sustained loads, both hydrostatic and hydrodynamic, in each one of the porches.

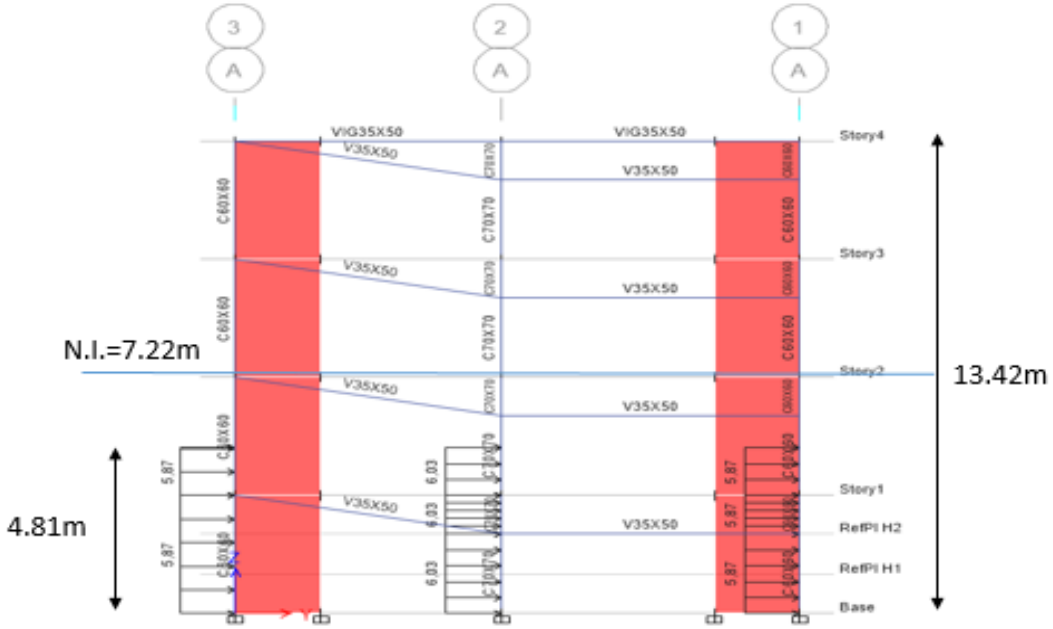

Fig. 18. Application of loads according to case 2

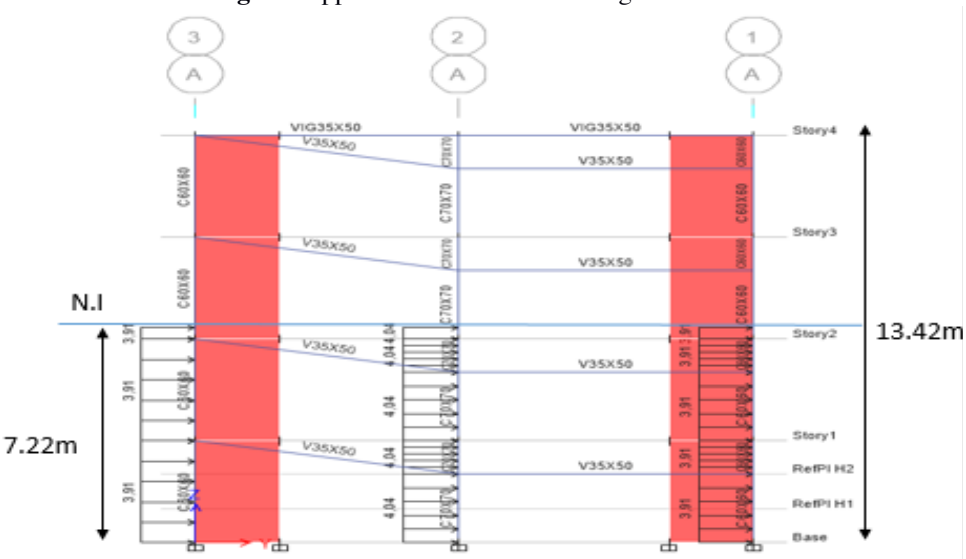

Fig. 19. Application of loads according to case 3

- First case: the exterior flooding is considered without exceeding the maximum height or less than one floor in height, in addition, the hydrodynamic forces combined with buoyancy forces are considered. This case does not apply for open structures.
- Second case: a flood depth equivalent to two thirds of the maximum height is considered in round-trip conditions.
- Third case: the maximum flood height is considered in round-trip conditions.

4.6 Cost analysis

The potential impact of tsunamis has potential wave heights over 5 meters. As a result, flooding may cover two or three floors, so the refuge level needs to consider such height: However, it would a wave of that height and its flooding impact will directly impact on property. This is critical in Salinas, as it was stated before, because the city is especially susceptible to tsunamis and flooding.

Although recent architecture design proposals have been made to deal with flooding. In a recent article in Insider, Danish architecture design firm, Tredje Natur, has proposed a new concept in architecture named as Pop-up design. This proposal has been developed in cooperation with the engineering companies COWI and RAMBØLL seems to deal with flooding efficiently. This proposal is based on Archimedes principle and seems to give a solution to flooding problems in urban areas (Leanna Garfield, 2017). However, this proposal has not been executed and it is quite expensive, alternative solutions needs to be proposed to protect human beings and provide alternative shelters regarding natural hazards.

This study proposes a new parking garage building that will function as well as refuge in case of a tsunami and flooding. The calculation of work volumes and cost calculation of the proposal is presented using the unit price analysis system (APU), to determine the direct cost. The indirect cost was assumed as 10% of the direct cost. Hereby, the next three tables, which are presented below, list the summary of items and volumes of work, required for the cost calculation (Table 3), the summary of costs for each item (Table 4), while the final table calculates the total cost of the structure, including direct and indirect costs (Table 5).

Table 3. Work volumes

No.	**Heading**	**Quantity**	**Unit**
1	Provisional Enclosure	153.20	ml
2	Cleaning and clearing	689.13	m^2
3	Setting out and Leveling	689.13	m^2
4	Reinforcing steel	46,659.26	kg
5	Plaster	2,100.94	m^2
6	Simple concrete columns and walls f´c = 240 kg / cm^2	327.08	m^3
7	Underlayment slab	133.20	m^3
8	Slab concrete f´c 240 kg / cm^2	421.98	m^3
9	Slab formwork	740.77	m^2
10	Concrete bleachers	10.16	m^3
11	Lightening (40x40x25)	4,504.00	u
12	Step formwork	69.28	m^2
13	Metal railings Cars	304.35	ml
14	Railing	128.10	ml
15	Beams	284.15	m^3
16	Beam formwork	1,087.84	m^2

Table 4. Summary of unit price analysis

HEADINGS		COSTS
1	Provisional Enclosure	$ 11.55
2	Cleaning and clearing	$ 1.48
3	Setting out and Leveling	$ 1.34
4	Reinforcing steel	$ 2.34
5	Plaster	$ 19.26
6	Simple concrete columns and walls f´c = 240 kg / cm²	$ 129.99
7	Underlayment slab	$ 233.95
8	Slab concrete f´c 240 kg / cm²	$ 134.90
9	Slab formwork	$ 12.53
10	Concrete bleachers	$ 124.94
11	Lightening (40x40x25)	$ 3.63
12	Step formwork	$ 12.53
13	Metal railings Cars	$ 190.34
14	Railing	$ 31.71
15	Beams	$ 137.93
16	Beam formwork	$ 19.42

Table 5 Budget price and adjustments (total costs)

No	HEADINGS	AMOUNT	COST	TOTAL
1	Provisional Enclosure	153.20	$ 11.55	$ 1,769.54
2	Cleaning and clearing	689.13	$ 1.48	$ 1,020.50
3	Setting out and Leveling	689.13	$ 1.34	$ 924.03
4	Reinforcing steel	46,659.26	$ 2.34	$ 109,147.94
5	Plaster	2,100.94	$ 19.26	$ 40,453.64
6	Simple concrete columns and walls f´c = 240 kg / cm²	327.08	$ 129.99	$ 42,515.79
7	Underlayment slab	133.20	$ 233.95	$ 31,161.80
8	Slab concrete f´c 240 kg / cm2	421.98	$ 134.90	$ 56,927.63
9	Slab formwork	740.77	$ 12.53	$ 9,281.68
10	Concrete bleachers	10.16	$ 124.94	$ 1,269.39
11	Lightening (40x40x25)	4,504.00	$ 3.63	$ 16,349.29
12	Step formwork	69.28	$ 12.53	$ 868.06
13	Metal railings Cars	304.35	$ 190.34	$ 57,929.70
14	Railing	128.10	$ 31.71	$ 4,061.80
15	Beams	284.15	$ 137.93	$ 39,192.00
16	Beam formwork	1,087.84	$ 19.42	$ 21,123.56
	TOTAL BUDGETS (USD)			**$433,996.41**

Since the values of the unit price analysis are calculated to 2020, the coefficients of the polynomial formula for the price readjustment are presented.

Table 6. Data for price readjustment applying the polynomial formula

Components			**%**	**Coefficient**
B	Workforce	$ 93,708.02	23.75%	p1
G	Tools	$ 14,772.67	3.74%	p2
I	Cement	$ 3,813.21	0.97%	p3
J	Stone materials	$ 2,773.24	0.70%	p4
D	Reinforcing steel	$ 79,283.42	20.10%	p5
F	Wood	$ 15,108.41	3.83%	p6
H	Blocks	$ 4,864.32	1.23%	p7
C	Pre-mixed concrete	$ 117,400.14	29.76%	p8
E	Handrail railings for cars	$ 50,403.50	12.78%	p9
X	Others	$ 12,415.27	3.15%	px
	Direct total costs	$ 394,542.19		
	Total budget	$ 433,996.41		

Finally obtaining the following polynomial formula.

$$Pr = \left(0.2375*\frac{B1}{B0} + 0.2976*\frac{C1}{C0} + 0.2010*\frac{D1}{D0} + 0.1278*\frac{E1}{E0} + 0.0383*\frac{F1}{F0} + 0.0374*\frac{G1}{G0} + 0.0123*\frac{H1}{H0} + 0.0097*\frac{I1}{I0} + 0.0070*\frac{J1}{J0} + 0.00315*\frac{X1}{X0}\right)$$

4. CONCLUSIONS

The characteristics of the wave in Salinas were determined as wave height equal to 6 meters and arrival time equal to 8 to 12 minutes.

The multi-use proposal as a refuge area has a capacity for 388 people and as a garage it has a capacity for 40 light vehicles and 30 motorcycles.

Architecturally, the proposal consists of two blocks with a dual system. The first block is the ramps for the vehicles and the second is the parking lot and the refuge area on the terrace.

Structurally, the proposal has drifts of less than 0.7%, which guarantees a performance level of immediate occupancy.

5. REFERENCES

ACHISINA (2017). Performance-Based Seismic Design. November 23. http://www.achisina.cl/index.php/publicaciones/manuales-guias

Acosta, C. E. (1983). Geodynamics of Ecuador. Geodynamics of the Eastern Pacific Region, Caribbean and Scotia Arcs, 9, 53-63.

ASCE SEI. (2000). Minimum design loads for buildings and other structures. In ANSI / ASCE Standard (Issue 7 98, pp. 1-330). https://doi.org/10.1061/9780872629042

ASCE SEI. (2016). Minimum Design Loads and Associated Criteria for Buildings and Other Structures. In ANSI / ASCE Standard. American Society of Civil Engineers. https://doi.org/10.1061/9780872629042

Athukorala, P. C., & Resosudarmo, B. P. (2005). The Indian Ocean tsunami: Economic impact, disaster management, and lessons. *Asian economic papers*, *4*(1), 1-39.

Aviles-Campoverde, D., Chunga, K., Ortiz-Hernández, E., Vivas-Espinoza, E., Toulkeridis, T., Morales-Delgado, A. and Delgado-Toala, D. (2021). Seismically induced soil liquefaction and geological conditions in the city of Jama due to the Mw7.8 Pedernales earthquake in 2016, NW Ecuador. Geosciences, 11, 20

Celorio-Saltos, J.C., García-Arias, J.M., Guerra-Luque, A.B., Barragan-Aroca, G. and Toulkeridis, T. (2018). Vulnerability analysis based on tsunami hazards in Crucita, central coastal of Ecuador. Science of Tsunami Hazards, 38(3): 225-263.

Chunga, K. and Toulkeridis, T. (2014). First evidence of paleo-tsunami deposits of a major historic event in Ecuador. Science of tsunami hazards, 33: 55-69.

Chunga, K., Mulas, M., Alvarez, A., Galarza, J. and Toulkeridis, T. (2019). Characterization of seismogenetic crustal faults in the Gulf of Guayaquil, Ecuador. Andean Geology, 46(1): 66-81.

Chunga, K., Toulkeridis, T., Vera-Grunauer, X., Gutierrez, M., Cahuana, N. And Alvarez, A. (2017). A review of earthquakes and tsunami records and characterization of capable faults on the northwestern coast of Ecuador. Science of tsunami hazards, 36: 100-127.

Cochard, R., Ranamukhaarachchi, S. L., Shivakoti, G. P., Shipin, O. V., Edwards, P. J., & Seeland, K. T. (2008). The 2004 tsunami in Aceh and Southern Thailand: a review on coastal ecosystems, wave hazards and vulnerability. *Perspectives in Plant Ecology, Evolution and Systematics*, *10*(1), 3-40.

Contreras López, M. (2013). Chronology of Tsunamis in Ecuador from 1586 to 2012. La Técnica: Revista de las Agrociencias. ISSN 2477-8982, 11, 50. https://doi.org/10.33936/la_tecnica.v0i11.565

Edler, D., Otto, K.H and Toulkeridis, T. (2020). Tsunami hazards in Ecuador – Regional differences in the knowledge of Ecuadorian high-school students. Science of Tsunami Hazards, 39(2), 86-112.

FEMA, (2019). Guidelines for Design of Structures for Vertical Evacuation from Tsunamis. Third Edition (FEMA P-646). FEMA P-646 Publication, August, 202.

Gutscher, M. A., Spakman, W., Bijwaard, H., & Engdahl, E. R. (2000). Geodynamics of flat subduction: Seismicity and tomographic constraints from the Andean margin. *Tectonics*, *19*(5), 814-833.

Hagen, M., & Azevedo, A. (2018). Deep and ultra-deep earthquakes worldwide, possible anomalies in South America. *Natural Science*, *10*(06), 199.

Heintz, J. A., & Mahoney, M. (2008). Guidelines for design of structures for vertical evacuation from tsunamis. *FEMA P646/June*.

INOCAR. "*MAPA DE INUNDACIÓN POR TSUNAMIS EN SALINAS*." 1:20000. Instituto Oceanográfico de la Armada (2019). https://www.inocar.mil.ec/tsunamis/mapas_inundacion/INOCAR_MI_SALINAS.pdf.

Intergovernmental Oceanographic Commission. Fourth Edition. Tsunami Glossary (2020). Paris, UNESCO, IOC Technical Series, 85. (English, French, Spanish, Arabic, Chinese) (IOC/2008/TS/85 rev.4).

Ioualalen, M., Monfret, T., Béthoux, N., Chlieh, M., Adams, G. P., Collot, J. Y., ... & Gordillo, G. S. (2014). Tsunami mapping in the Gulf of Guayaquil, Ecuador, due to local seismicity. Marine Geophysical Research, 35(4), 361-378.

Ioualalen, M., Pazmino, N. A., Renteria, W. J., Charvis, P., Solis Gordillo, G. X., Delouis, B., ... & Burbano Gallegos, L. A. (2018). Analysis of tsunami tide gauge records following the 2016 Ecuadorian earthquake and tsunami. *Journal of Waterway, Port, Coastal, and Ocean Engineering*, *144*(2), 05017004

Iwasaki, T., Hirata, N., Kanazawa, T., Urabe, T., Motoya, Y., & Shimamura, H. (1991). Earthquake distribution in the subduction zone off eastern Hokkaido, Japan, deduced from ocean-bottom seismographic and land observations. *Geophysical Journal International*, *105*(3), 693-711.

Leanna, G. (2017) This flood-proof parking garage could automatically pop-up when it rains. The Insider, Technology, (Dec 11, 2017)

Lynett, P., Weiss, R., Renteria, W., Morales, G. D. L. T., Son, S., Arcos, M. E. M., & MacInnes, B. T. (2013). Coastal impacts of the March 11th Tohoku, Japan tsunami in the Galapagos Islands. Pure and Applied Geophysics, 170(6-8), 1189-1206.

Martinez, N. & Toulkeridis, T. (2020). Tsunamis in Panama – History, preparation and future consequences. Science of Tsunami Hazards, 39(2), 53-68.

Massonne, H.J. and Toulkeridis, T. (2012). Widespread relics of high-pressure metamorphism confirm major terrane accretion in Ecuador: a new example from the Northern Andes. Int. Geol Rev., 54, 1: 67-80.

Matheus Medina, A.S., Cruz D´Howitt, M., Padilla Almeida, O., Toulkeridis, T., & Haro, A.G. (2016). Enhanced vertical evacuation applications with geomatic tools for tsunamis in Salinas, Ecuador. Science of Tsunami Hazards, 35, (3): 189-213

Matheus-Medina, A.S., Toulkeridis, T., Padilla-Almeida, O., Cruz-D´ Howitt, M., & Chunga, K. (2018). Evaluation of the tsunami vulnerability in the coastal Ecuadorian tourist centers of the peninsulas of Bahia de Caráquez and Salinas. Science of Tsunami Hazards, 38(3): 175-209.

Mato, F. and Toulkeridis, T. (2018). An unsupervised K-means based clustering method for geophysical post-earthquake diagnosis. 2017 IEEE Symposium Series on Computational Intelligence (SSCI). 1-8

Mostafizi, A., Wang, H., Cox, D., & Dong, S. (2019). An agent-based vertical evacuation model for a near-field tsunami: Choice behavior, logical shelter locations, and life safety. *International journal of disaster risk reduction*, *34*, 467-479.

Navas, L., Caiza, P. and Toulkeridis, T. (2018). An evaluated comparison between the molecule and steel framing construction systems – Implications for the seismic vulnerable Ecuador. Malaysian Construct. Res. J. 26 (3), 87–109.

Norio, O., Ye, T., Kajitani, Y., Shi, P., & Tatano, H. (2011). The 2011 eastern Japan great earthquake disaster: Overview and comments. International Journal of Disaster Risk Science, 2(1), 34-42.

NTE INEN 2248. (2016). Accessibility of people to the physical environment. Parking lots. 2. 3.

Padrón, E., Hernández, P.A., Pérez, N.M., Toulkeridis, T., Melián, G., Barrancos, J., Virgili, G., Sumino H. and Notsu, K. (2012). Fumarole/plume and diffuse CO_2 emission from Sierra Negra volcano, Galapagos archipelago. Bull. Of Volcanol., 74: 1509-1519.

Pararas-Carayannis G. (1983). The Tsunami Impact on Society. Tsunamis - Their Science and Engineering.: Terra Scientific Publishing Company, Tokyo, pp. 3-8 ,1983.

Pararas-Carayannis, G. (1980). Earthquake and tsunami of 12 December 1979 in Colombia. Tsunami Newsletter, 13(1), 1-9.

Pararas-Carayannis, G. (1988). Risk assessment of the tsunami Hazard. In Natural and man-made hazards (pp. 183-191). Springer, Dordrecht.

Pararas-Carayannis, G. (2002). Evaluation of the threat of mega tsunami generation from postulated massive slope failures of island stratovolcanoes on La Palma, Canary Islands, and on the island of Hawaii. Science of Tsunami Hazards, 20(5), 251-277.

Pararas-Carayannis, G. (2013). Critical Assessment of Disaster Vulnerabilities in the Kingdom of Saudi Arabia-Strategies for Mitigating Impacts and Managing Future Crises. InThe First Saudi International Conference on crisis and Disaster Management (pp. 762-782).

Pararas-Carayannis, G. and Zoll, P. (2017). Incipient evaluation of temporal el nino and other climatic anomalies in triggering earthquakes and tsunamis – case study: The earthquake and tsunami of 16th april 2016 in Ecuador. Science of Tsunami Hazards, 36(4), 262-291.

Pararas-Carayannis, G. (2010). The earthquake and tsunami of 27 February 2010 in Chile – Evaluation of source mechanism and of near and far-field tsunami effects. Science of Tsunami Hazards, 29, 2: 96-126.

Pararas-Carayannis, G. (2012). Potential of tsunami generation along the Colombia/Ecuador subduction margin and the Dolores-Guayaquil Mega-Thrust. Science of Tsunami Hazards, 31, 3: 209-230.

Pararas-Carayannis, G. (2014). The Great Tohoku-Oki earthquake and tsunami of March 11, 2011 in Japan: A critical review and evaluation of the tsunami source mechanism. Pure and Applied Geophysics, 171(12): 3257-3278.

Pararas-Carayannis, G. (2018). Brief history of early pioneering tsunami research - Part A. Science of Tsunami Hazards, 37(1), 49-129.

Park, S., Van de Lindt, J. W., Gupta, R., & Cox, D. (2012). Method to determine the locations of tsunami vertical evacuation shelters. *Natural hazards*, *63*(2), 891-908.

Parwanto, N. B., & Oyama, T. (2014). A statistical analysis and comparison of historical earthquake and tsunami disasters in Japan and Indonesia. *International Journal of Disaster Risk Reduction*, *7*, 122-141.

Plümper, T., Flores, A. Q., & Neumayer, E. (2017). The double-edged sword of learning from disasters: Mortality in the Tohoku tsunami. *Global environmental change*, *44*, 49-56.

Rentería, W. (2007). Elaboración de mapas digitales de inundación por tsunamis para machala y salinas basados en el tsunami histórico de 1953.

Renteria, W. (2013). Tsunami forecast for the Galapagos Islands. 18 (1), 151-161.

Rentería, W., Lynett, P., Weiss, R. & De La Torre, G. (2012). Informe de la investigación de campo de los efectos del tsunami de Japón Marzo 2011, en las islas Galápagos. Acta Oceanográ ca del Pací co. Vol. 17(1): 177 - 203.

Rodríguez Espinosa, F., Toulkeridis, T., Salazar Martinez, R., Cueva Girón, J., Taipe Quispe, A., Bernaza Quiñonez, L., Padilla Almeida, O., Mato, F., Cruz D´Howitt, M., Parra, H., Sandoval, W. and Rentería, W. (2017). Economic evaluation of recovering a natural protection with concurrent relocation of the threatened public of tsunami hazards in central coastal Ecuador. Science of tsunami hazards, 36: 293-306.

Rodriguez, F., Cruz D´Howitt, M., Toulkeridis, T., Salazar, R., Ramos Romero, G.E., Recalde Moya, V.A. and Padilla, O. (2016). The economic evaluation and significance of an early relocation versus complete destruction by a potential tsunami of a coastal city in Ecuador. Science of tsunami hazards, 35, 1: 18-35.

Ryan, W.B.F., S.M. Carbotte, J.O. Coplan, S. O'Hara, A. Melkonian, R. Arko, R.A. Weissel, V. Ferrini, A. Goodwillie, F. Nitsche, J. Bonczkowski, and R. Zemsky (2009), *Global Multi-Resolution Topography synthesis*, Geochem. Geophys. Geosyst., 10, Q03014, doi: 10.1029/2008GC002332

Simons, M., Minson, S.E., Sladen, A., Ortega, F., Jiang, J., Owen, S.E., Meng, L., Ampuero, J.P., Wei, S., Chu, R., & Helmberger, D.V. (2011). The 2011 magnitude 9.0 Tohoku-Oki earthquake: Mosaicking the megathrust from seconds to centuries. science, 332(6036), pp.1421-1425.

Sladen, A., Tavera, H., Simons, M., Avouac, J. P., Konca, A. O., Perfettini, H., ... & Cavagnoud, R. (2010). Source model of the 2007 Mw 8.0 Pisco, Peru earthquake: Implications for seismogenic behavior of subduction megathrusts. *Journal of Geophysical Research: Solid Earth*, *115*(B2).

Soloviev, S. L., & Go, C. N. (1984). Catalog of tsunamis on the western shore of the Pacific Ocean. *Canadian Translation of Fisheries and Aquatic Sciences*, (5078).

Suárez-Acosta, P.E., Cañamar-Tipan, C.D., Ñato-Criollo, D.A., Vera-Zambrano, J.D., Galarza-Vega, K.L., Guevara-Álvarez, P.M., Fajardo-Cartuche, C.N., Herrera-Garcés, K. K., Ochoa-Campoverde, C.V., Torres-Orellana, J.S., Rentería, W., Chunga, K., Padilla, O., Sinde-González, I., Simón-Baile, D. and Toulkeridis, T. (2021). Evaluation of seismic and tsunami resistance of potential shelters for vertical evacuation in case of a tsunami impact in Bahia de Caráquez, central coast of Ecuador. Science of Tsunami Hazards, 40(1), 1-37.

Suhr, N., Rojas-Agramonte, Y., Chew, D. M., Pinto, A. J., Villagómez-Díaz, D., Toulkeridis, T., & Mertz-Kraus, R. (2019). Detrital-zircon geochronology and provenance of the El Oro Metamorphic Complex, Ecuador: Geodynamic implications for the evolution of the western Gondwana margin. Journal of South American Earth Sciences, 90, 520-539.

Titov, V. V., Moore, C. W., Greenslade, D. J. M., Pattiaratchi, C., Badal, R., Synolakis, C. E., & Kânoğlu, U. T. (2011). A new tool for inundation modeling: Community Modeling Interface for Tsunamis (ComMIT). Pure and Applied Geophysics, 168(11), 2121-2131.

Titov, V., Kânoğlu, U. and Synolakis, C. (2016). "Development of MOST for Real-Time Tsunami Forecasting." Journal of Waterway, Port, Coastal, and Ocean Engineering 142, no. 6: 03116004.

Toulkeridis, T. (2013). Volcanes Activos Ecuador. Santa Rita, Quito, Ecuador: 152 pp

Toulkeridis, T. (2016). Unexpected results of a seismic hazard evaluation applied to a modern hydroelectric plant in central Ecuador. *J. Struct. Eng*, *43*(4), 373-380.

Toulkeridis, T., Chunga, K., Rentería, W., Rodriguez, F., Mato, F., Nikolaou, S., Cruz D´Howitt, M., Besenzon, D., Ruiz, H., Parra, H. and Vera-Grunauer, X. (2017). The 7.8 M_w Earthquake and Tsunami of the 16th April 2016 in Ecuador - Seismic evaluation, geological field survey and economic implications. Science of tsunami hazards, 36: 197-242.

Toulkeridis, T., Mato, F., Toulkeridis-Estrella, K., Perez Salinas, J.C., Tapia, S. and Fuertes, W. (2018). Real-Time Radioactive Precursor of the April 16, 2016 Mw 7.8 Earthquake and Tsunami in Ecuador. Science of tsunami hazards, 37: 34-48.

Toulkeridis, T., Parra, H., Mato, F., Cruz D´Howitt, M., Sandoval, W., Padilla Almeida, O., Rentería, W., Rodríguez Espinosa, F., Salazar martinez, R., Cueva Girón, J., Taipe Quispe, A. and Bernaza Quiñonez, L. (2017). Contrasting results of potential tsunami hazards in Muisne, central coast of Ecuador. Science of tsunami hazards, 36: 13-40

Toulkeridis, T., Porras, L., Tierra, A., Toulkeridis-Estrella, K., Cisneros, D., Luna, M.,Carrión, J.L., Herrera, M., Murillo, A., Perez-Salinas, J.C., Tapia, S., Fuertes, W. and Salazar, R. (2019). Two independent real-time precursors of the 7.8 Mw earthquake in Ecuador based on radioactive and geodetic processes—Powerful tools for an early warning system. Journal of Geodynamics, 126: 12-22

Toulkeridis, T., Porras, L., Tierra, A., Toulkeridis-Estrella, K., Cisneros, D., Luna, M.,Carrión, J.L., Herrera, M., Murillo, A., Perez-Salinas, J.C., Tapia, S., Fuertes, W. and Salazar, R. (2019). A potential early warning system for earthquakes based on two independent real-time precursors – the case of Ecuador´s 7.8 Mw in 2016. Proceedings of the International Conference on Natural Hazards and Infrastructure 2019, 2nd International Conference on Natural Hazards and Infrastructure, ICONHIC 2019; Chania; Greece; 23 June 2019 through 26 June 2019; Code 257429

Wong, M. M. R., & Said, A. M. (2020). Consequences of the 2004 Indian ocean tsunami in Malaysia. *Safety science*, *121*, 619-631.

Wood, N., Jones, J., Schelling, J., & Schmidtlein, M. (2014). Tsunami vertical-evacuation planning in the US Pacific Northwest as a geospatial, multi-criteria decision

ISSN 8755-6839

SCIENCE OF **TSUNAMI HAZARDS**

Journal of Tsunami Society International

Volume 40 **Number 3** **2021**

3D TOMOGRAPHY OF IONOSPHERIC ANOMALIES AFTER THE 2020 TURKEY EARTHQUAKE AND TSUNAMI USING GNSS-TEC

Mokhamad Nur Cahyadi[1,2*], Ira Mutiara Anjasmara[1], Ihsan Naufal Muafiry[3], Nurrohmat Widjajanti[4], Deasy Arisa[5], Buldan Muslim[6], Meilfan Eka Putra[1]

[1]Geomatics Engineering Department, Institut Teknologi Sepuluh Nopember, Indonesia
[2]Research Center of Science-Technology of Marine and Earth, Directorate of Research and Community Service, Sepuluh Nopember Institute of Technology, Surabaya, Indonesia
[3]Survey and Mapping Department, Politeknik Sinar Mas Berau Coal, Indonesia
[4]Geodetic Engineering, Universitas Gadjah Mada, Indonesia
[5]Research Center for Geotechnology, Indonesian Institute of Sciences, LIPI, Bandung, Indonesia
[6]National Institute of Aeronautics and Space, LAPAN, Bandung, Indonesia;
*email correspondence: cahyadi@geodesy.its.ac.id

ABSTRACT

Global Navigation Satellite System (GNSS) satellite observations can obtain Total Electron Content (TEC) values in the ionosphere layer. The TEC value is obtained by decreasing the phase difference of the GNSS satellite's two carrier waves (L-band). The calculation of the TEC value using GNSS can be used in disaster phenomena such as earthquakes observed in this study. The earthquake phenomenon can cause vertical deformation in the Earth's crust, resulting in the appearance of acoustic waves propagating towards the ionosphere layer and changes in the ionosphere density in a moment. A propagating gravity wave has a speed of 0.3 km/ s towards the ionosphere layer. This disturbed ionosphere layer was detected within minutes of the mainshock. The anomaly in this study was detected by Global Positioning System (GPS) Pseudo Random Noise (PRN) 16 from 16 observation GNSS stations on the mainland of Turkey. The observed ionosphere anomalies were then modeled

using tomography modelling to obtain spatial information from these anomalies. The tomography results found that the PRN 16 GPS satellites contained positive and negative anomalies located northeast of the epicenter.

Keywords: *3D Tomography, Earthquake, GNSS, Total Electron Content, Turkey Earthquake*

---

1. INTRODUCTION

The study of earthquake and tsunami disaster mitigation in geodesy and geomatics can be done by utilizing GNSS (Global Navigation Satellite System) system technology. This GNSS system is conducted to position a particular point on the Earth's surface accurately. GNSS is usually also used to monitor land subsidence (Anjasmara et al., 2018) and monitoring water vapor in the atmosphere (Cahyadi et al., 2018). Furthermore, GNSS satellite observations can be used to obtain TEC (Total Electron Content) values in the ionosphere layer. The TEC value obtained can be in the form of electron density along the line of sight (LoS) in the ionosphere layer called Slant TEC (STEC) or in the form of a vertical, which is commonly called Vertical TEC (VTEC). The use of GNSS satellites in obtaining TEC values is often used in observing ionospheric anomalies in earthquake phenomena (Cahyadi & Heki, 2015; Cahyadi & Heki, 2013a; Cahyadi & Heki, 2013b; Cahyadi, 2014; Cahyadi et al., 2018; Heki & Cahyadi, 2012; Sharma et al., 2017; Liu et al., 2011), tsunami (Kakinami et al., 2012; Muslim et al., 2020; Liu et al., 2006; Rolland et al., 2010), and volcanic eruptions (Shults et al., 2016; Nakashima et al., 2016; Cahyadi et al., 2020; Nakashima et al., 2014). Ionosphere disturbances can occur in several natural phenomena such as earthquakes, tsunamis, and volcanic eruptions. These phenomena can send acoustic waves propagating upward to the ionosphere layer, dominated by TEC (Cahyadi & Heki, 2015).

There was a strong earthquake (Mw 7) (USGS, 2020) from the east-west normal fault, which occurred on October 30, 2020 (11:51 UTC) between the offshore Seferihisar Izmir, Turkey, and the island of Samos, Greece. The focal mechanism shows a normal fault oriented in an east-west direction. The earthquake also caused a tsunami 11 minutes after the aftershock [Dogan et al., 2021] to reach a height of 6 meters and caused several coastal towns to be submerged as deep as 2 meters [Yalciner et al., 2020]. The aftershock earthquake happened about three hours later with 5 Mw magnitudes with a depth of about 15 km.

The vertical deformation resulting from the earthquake has caused the acoustic waves to move upward and sideways towards the ionosphere, disturbing electron density (Calais & Minster, 1995). Ionospheric disturbances observation using GNSS satellite have been carried out in the previous research (Cahyadi & Heki, 2015), which studied ionospheric disturbances caused by the 2012 North Sumatra earthquake with a magnitude of M 8.6. The quake was recorded as the largest strike-slip earthquake ever recorded and could destroy the oceanic lithosphere off the Indian Ocean coast of

North Sumatra. In this study, ionosphere anomalies were found 10-20 minutes after the earthquake occurred. Ionosphere disturbances were also observed in another research (Liu et al., 2011) which studied ionospheric disturbances caused by the 2011 Tohoku Japan earthquake with a magnitude of M 9. The quake generated vibrations on the Earth's surface which were very extraordinary and triggered a tsunami. Then the vertical deformation will produce disturbances in the ionosphere layer, which contains TEC assemblies. Ionosphere disturbances were recorded 7 minutes after the earthquake occurred with a velocity from the Earth's surface to the ionosphere layer of 833 m/s. Likewise, tsunami waves (even if only a few centimeters in the deep sea) can generate gravity waves which also move upward and sideways towards the ionosphere layer (Daniels, 1952). (Artru, 2005) observed the tsunami that occurred due to the Peru earthquake Mw = 8.2 in 2001 using GNSS network GEONET in Japan. The tsunami propagated towards the coast of Japan in the range of 20 to 22 hours after the aftershock. The amplitudes found in the traveling ionospheric disturbance show the magnitude of ±1 TECU.

Various observations were done to understand general characteristics of ionospheric disturbances, but imaging the ionospheric layer is still rarely obtained. Land-based 2D tomography modelling was done by Austen et al. (1988), which was then developed to observe traveling ionosphere disturbance (TIDs) by Pryse et al. (995), and Comberiate et al. (2007) used space-based UV tomography to describe plasma depletion at low latitudes. Kunistyn et al. (1997) also discussed the possibility of near-space environment tomography with GPS and ground-based stations. They showed that applying combinations of different satellite systems is beneficial in near-space environment tomography realization. Tomographic modelling was also used by Feng et al. (2021), who studied the phenomenon of the geomagnetic storm on June 17 and June 22, which occurred in Wuhan, China. This study used the TEC value to perform spatial analysis using tomographic modelling of the observed anomalies electron density changes. However, there is no detailed spatial information regarding the anomalies of the ionospheric layer in some of these studies, and it still uses STEC for tomography material.

The ionosphere observation method in this study was done using computerized tomography (CT). The usage of CT began in the previous survey (Austen et al., 1988), which introduced electron density depiction using CT modelling. The CT is beneficial to obtain spatial information on ionosphere disturbances detected in GNSS observations. This study will describe the ionosphere into a 3D tomographic model based on the altitude layer. Tomography 3D modelling requires observational data with different azimuths and elevations obtained from many stations around the earthquake area over a large area. The case of this study was the M 7 earthquake that occurred in Turkey on October 30, 2020. The result of this study is expected to plan an early warning system for the benefit of disaster mitigation.

The TEC value used in the study was obtained by differencing the phase difference of the carrier wave (L1 (~ 1.5 GHz) and L2 (~ 1.2 GHz)) from GNSS satellite observations. The TEC values obtained can be in the form of STEC and VTEC. STEC is the value of electron density contained along the LoS, while VTEC is the value of electron density that corresponds to the vertical direction of the ionosphere. The VTEC value is obtained by multiplying the cosine value of the zenith angle between the vertical direction and the direction of propagation of the GNSS satellite towards the Earth. The value of electron density is usually written as TECU (1TECU = 10^{16} electrons / m^2). The STEC value can be compared with the polynomial number line curve to obtain STEC residual. Significant difference values of TEC changes can be indicated as anomalous values for the ionosphere. The intersection between the ionosphere layer and the LoS is called the Ionospheric Pierce Point (IPP), while the projections on the Earth's surface are called the Sub-ionospheric Point (SIP).

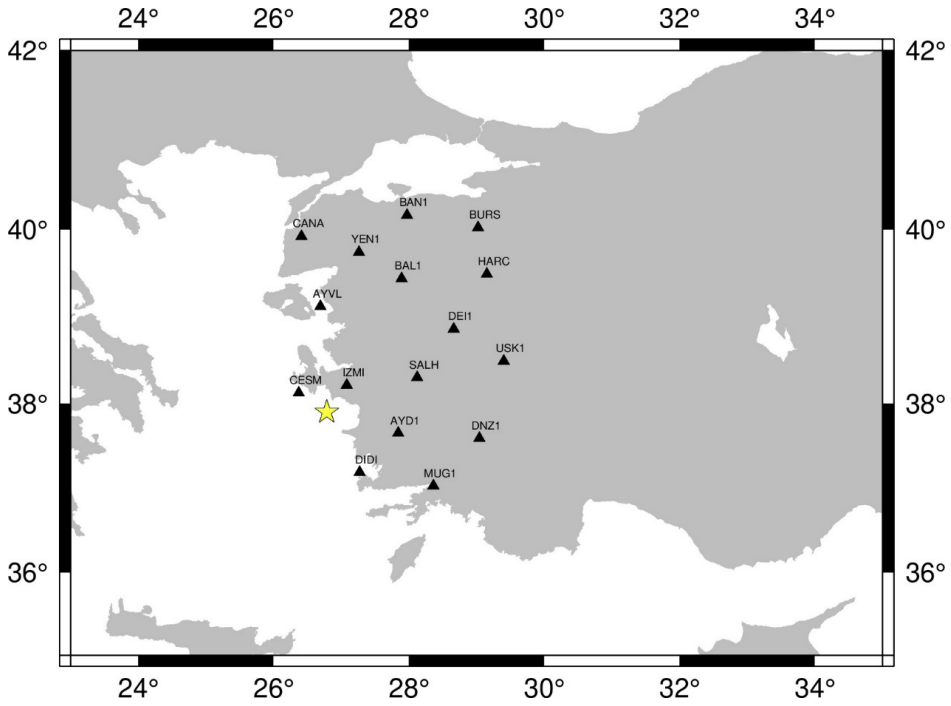

Figure 1. The distribution of GNSS observation stations and epicenter. The black triangle shows the location of GNSS stations, while the yellow star shows the epicenter location of the earthquake.

The tomography block was settled with the dimensions of 1° east-west direction, 1.2° north-south direction, and 75 km on the top-bottom side. Tomography blocks are assumed to be homogeneous. The division of ionosphere value for each LoS was done to get the electron density value in each tomography block based on the length of LoS penetration in a tomography block. The

length of LoS penetration is obtained from the length calculation of 2 LoS intersections with the sides of the tomography block. The value of density in the tomography block is obtained using the equation (He & Heki 2018):

$$\Delta \mathrm{STEC_i} = \sum_{j=1}^{n} A_{ij} x_j + e_i$$

This equation is used to obtain the density value of each tomography block passed by LoS using the LoS penetration length component in each block, the total TEC anomalous density value, and considering the measurement error value (it is assumed that 0.05 TECU originates from the typical error of differential GNSS measurements (Coster et al. 2013)).

3. RESULTS

3A. Ionosphere Anomaly Shortly After an Earthquake and Tsunami

The calculations were carried out using the equation of ionosphere linear combination to obtain TEC value on GNSS observations in the ionosphere layer along the observation path. The TEC value obtained will then be combined with the comparison value using a reference curve from the polynomial number with 6th order polynomial based on the best fitting line. Ionospheric anomalies can be detected at a STEC residual value which is significantly different from the reference curve. The anomaly value is obtained by calculating TEC changes and reducing the TEC value with the polynomial value of order 6. Anomaly changes in ionosphere density that experience disturbances were detected about 45 minutes after the mainshock or about 35 minutes after the tsunami on the PRN GPS satellite 16.

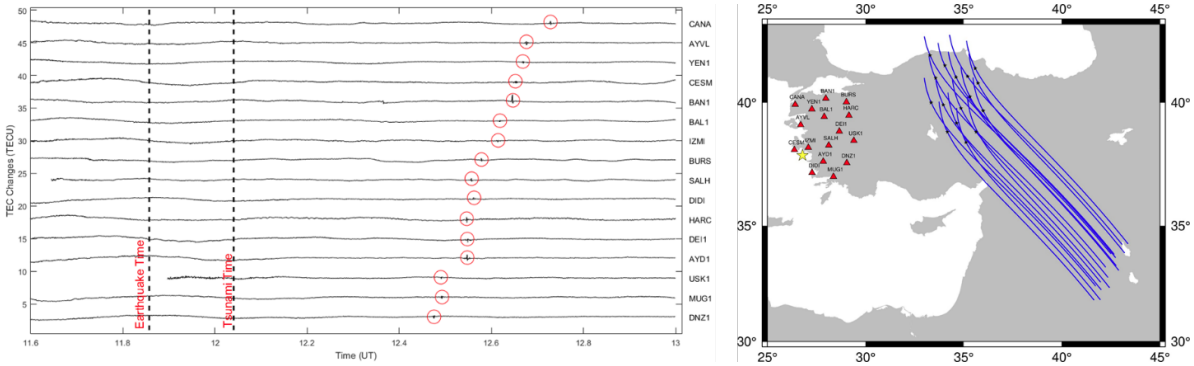

Figure 2. (Left) TEC time series from 2020 Turkey earthquake observed by PRN16 satellite. Two vertical lines indicate the time of earthquake and tsunami detected by USGS at 11.51 UT and 12.02UT, respectively. (Right) SIP trajectory at 11.00 – 14.00 UT, the small black star shows the time of the earthquake, the red triangle shows the observation station's location, and the yellow star shows the epicenter location.

Figure 2 shows ionosphere disturbances that occurred shortly after the mainshock repeatedly. The ionosphere anomaly was detected about 35 minutes after the tsunami, which was detected by 16 observation stations scattered around the epicenter. Then, GPS PRN 16 observed the gravity wave velocity at the tsunami traveling ionospheric disturbance (TTID) propagation of 0.3 km s-1. This propagation is consistent with the velocity of the gravity wave.

The deformation of Turkey's 2020 earthquake on October 30 at 11:51 UT is detected as strike-slip type. The Okada modelling calculation results based on the dip, strike and slip parameters obtained from the Global Centroid Moment Tensor (GCMT) are 246°, 67°, and -9 °. Figure 3 shows an uplift component for about 8 cm following the observation of Evelpidou et al. (2021). The vertical deformation of about 13 cm even mechanism of the earthquake is detected as strike-slip. Land subsidence was found more often compared to the uplift in this earthquake mechanism.

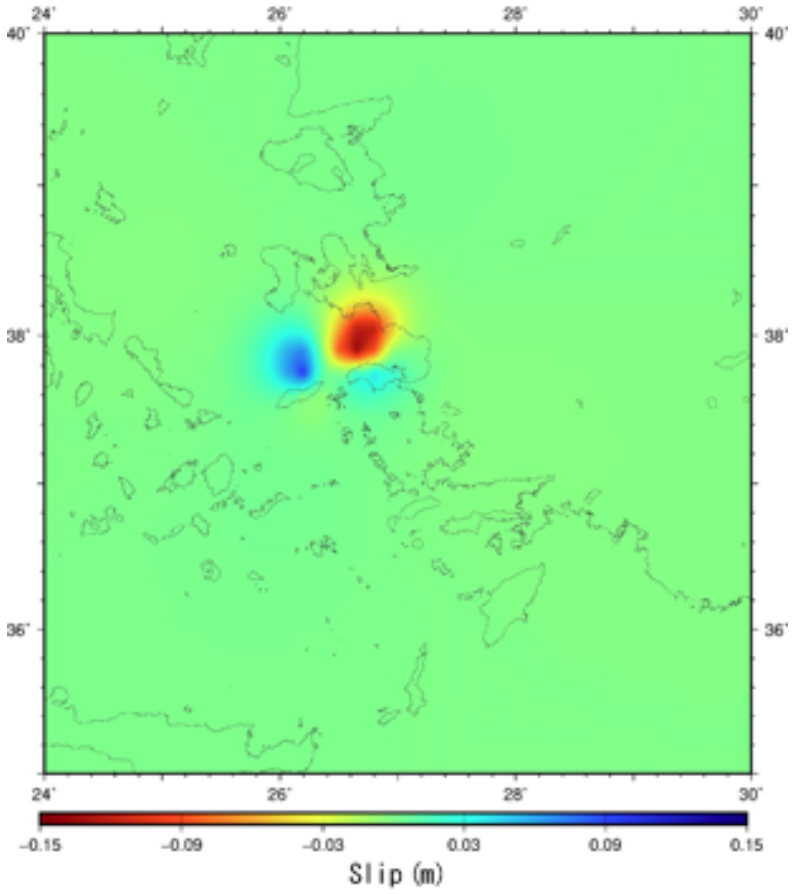

Figure 3. The vertical movement of the Earth's crust from 2020's Turkey earthquake. The earthquake was calculated using the Okada model (1992) and using fault geometry from GCMT.

3B. Tomographic model from Ionospheric Disturbance

The PRN 16 GPS satellites detected several ionospheric anomalies a few minutes after the earthquake. Anomalies were seen within 35 minutes after the tsunami. The anomaly was detected by 16 observation stations located around the epicenter of the quake.

The tomographic model (Figure 4) reports the density distribution of the ionospheric anomaly at each altitude at 100 Km intervals. In each tomographic model, the voxels containing the most anomalous payloads are at an altitude of 300 – 400 Km. In Figures 4(a-c), the positive anomaly appears at a lower altitude of about 200 km. In comparison, the negative anomaly appears in the east at a higher altitude, i.e., from 300 Km – 400 Km. Figure 4b is the tomographic model that has the largest value. It can be seen from the dense voxel color; this is because many stations detect anomalies at 32 minutes after the tsunami or 42 minutes after the earthquake.

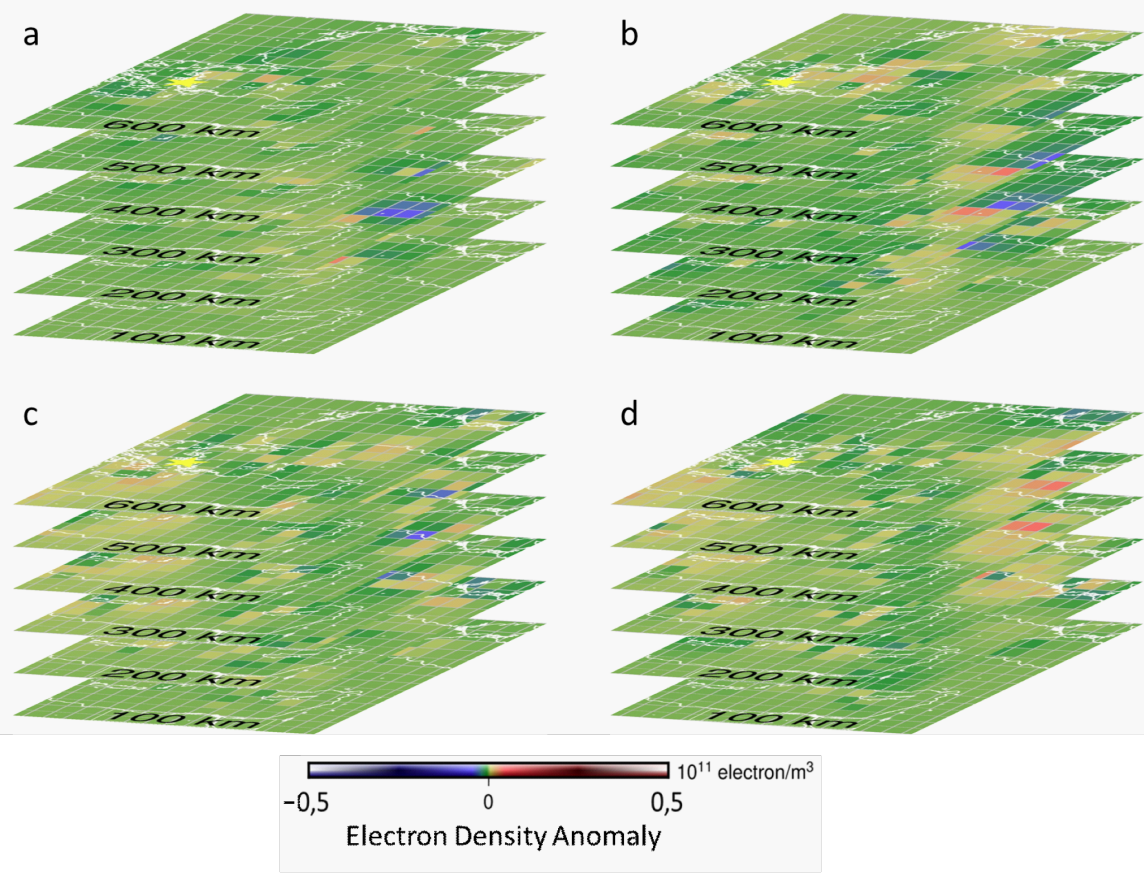

Figure 4. Tomographic model of (a) 29 minutes, (b) 32 minutes, (c) 40 minutes, and (d) 43 minutes after the tsunami. The small yellow star indicates the location of the epicenter, while the blue color tomographic voxel indicates a negative anomaly, while the red color indicates a positive anomaly.

3C. Accuracy Test

The checkerboard resolution test is used to analyze the reliability of electron density using a 3D tomography model. In this research, the investigation of ionospheric changes was conducted on the 2020 Turkish earthquake. STEC LoS anomaly data were synthesized, assuming a checkerboard-like distribution of electron density anomalies with 0.10 and –0.10 TECU/100 km.

Figure 5 (output) shows the anomaly distribution recovered from the synthesis model of checkerboard data. The picture shows that the 3D tomography finishes the high structure perfectly, as shown on the input image. By comparing both output displays, it can be concluded that the resolution on the higher altitudes (~200 km) is slightly worse than those with lower altitudes (~100 km). It is reflected by better coverage (more availability) of LoS for lower blocks. The output image shows that the resolution is higher over land and worse over the ocean.

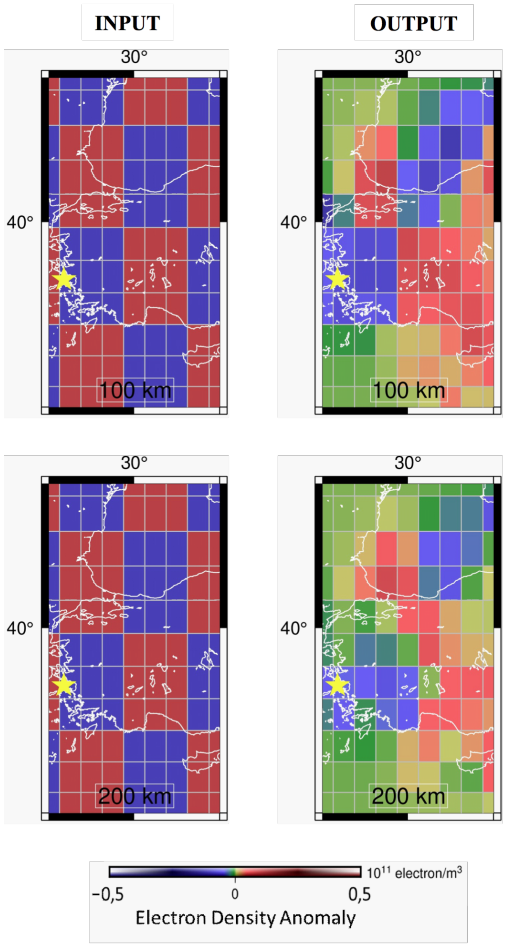

Figure 5. 3D anomaly pattern of electron density was used for checkerboard resolution with the height of 100 km (left) and 200 km (right). The alternating pattern of positive and negative anomalies was given at 0,15 and –0,15 TECU/100 km.

The comparison of STEC post-fit residual was conducted (Figure 6 on the lower panel) using STEC residual observation (Figure 6 on the top panel). The post-fit residue in each case shows much smaller dispersion, and the deviation standard is similar to the assumed error of STEC observation.

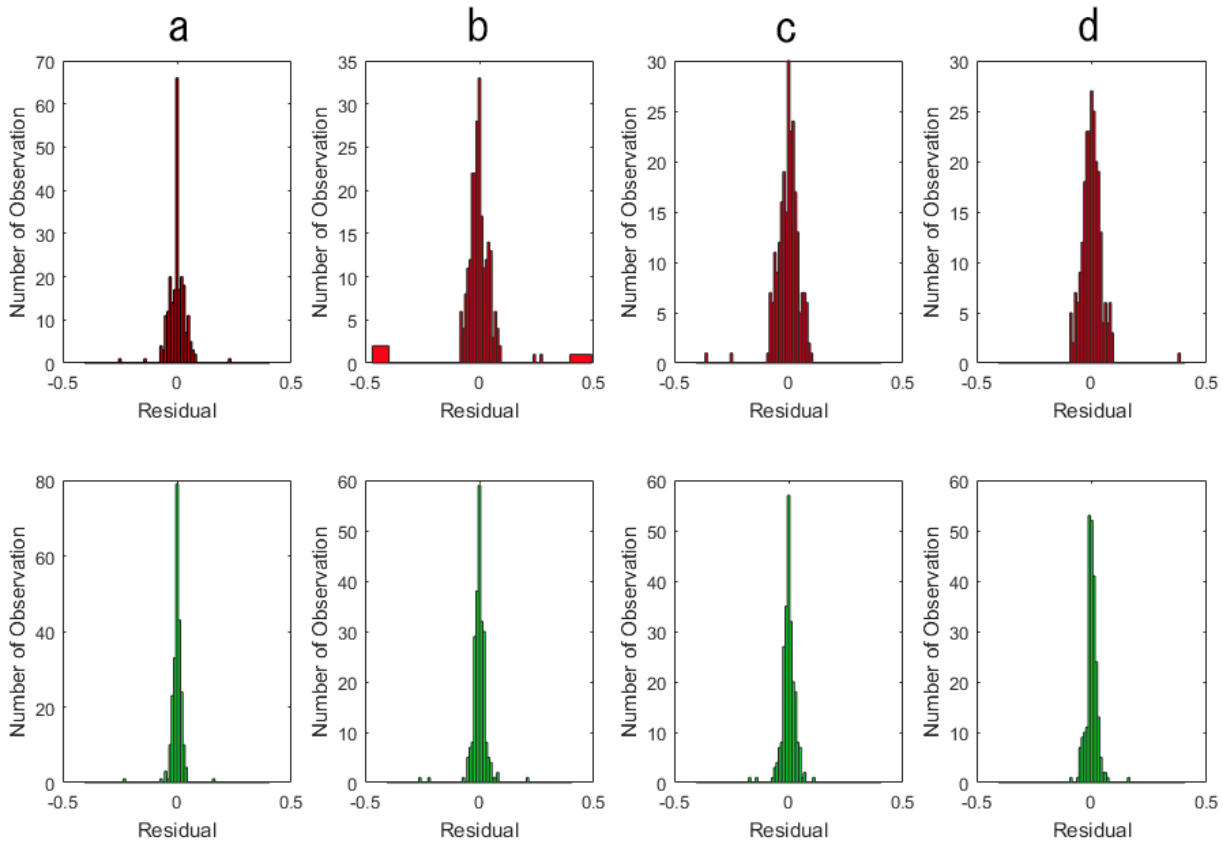

Figure 6. The input of STEC residual anomaly distribution (red) and the post-fit residual (x10^{11} electron/m^3) (green) for tomography model of (a) 29 minutes, (b) 32 minutes, (c) 40 minutes, and (d) 43 minutes after the tsunami. The post-fit residual becomes smaller than the observation, indicating that the tomography result has reproduced the observations adequately.

4. CONCLUSIONS

This study observed the 3D structure of the ionosphere's electron density anomaly immediately after the 2020 Turkey earthquake (Mw7.0) using GNSS-TEC data taken from mainland Turkey as the data input for the 3D tomography program. The appearance of ionosphere anomalies was detected by satellite GPS PRN 16 and happened about 45 minutes after the mainshock, around 35

minutes after the tsunami. It was found that the tsunami waves triggered atmospheric disturbances, which then propagated at an average speed of about 0.3 km/s into the ionosphere layer and significantly disrupted the electron density. This propagation speed is consistent with gravity waves and caused by tsunamis (Artru et al., 2005; Tsugawa et al., 2011; Cahyadi & Heki, 2015; Rolland et al., 2010; Savastano et al., 2017).

The visualization of ionospheric disturbances was done using tomography modelling to provide spatial information from the location of anomalies detected by GPS satellites PRN 16. Tomography offers information on the anomaly density of each voxel that has been arranged. The anomalies in this study were detected using PRN 16 GPS satellites were positive and negative anomalies located in the northeast of the epicenter. The usage of tomography can obtain spatial information from detected anomalies. The anomalies induced by gravity waves mainly distributed from 100 to 600 km in altitude, and their magnitude decreased with altitude. They showed similar orders of magnitude at the altitudes of 300 km and 400 km, and the magnitude decreased from 500 km with height. The performance of the tomography result was also confirmed using a resolution test, which is a checkerboard test. The result shows that the resolution at higher altitudes was slightly worse than at lower altitudes. The checkerboard test also indicates that the resolution is higher over land and worse over the ocean.

REFERENCES

Anjasmara, I. M., Yulyta, S. A., Cahyadi, M. N., Khomsin, Taufik, M., & Jaelani, L. M. (2018, July). Land subsidence analysis in Surabaya urban area using time series InSAR method. In AIP Conference Proceedings (Vol. 1987, No. 1, p. 020071). AIP Publishing LLC.

Artru, J., Ducic, V., Kanamori, H., Lognonné, P., & Murakami, M. (2005). Ionospheric detection of gravity waves induced by tsunamis. Geophysical Journal International, 160(3), 840-848.

Austen, J. R., Franke, S. J., & Liu, C. H. (1988). Ionospheric imaging using computerized tomography. Radio Science, 23(3), 299-307.

Cahyadi, M. N. (2014). Near-Field coseismic ionospheric disturbances of earthquakes in and around Indonesia. The Degree of Doctor of Philosophy. Dept. Natural History Sciences, Graduate School of Science, Hokkaido University.

Cahyadi, M. N., & Heki, K. (2013a). Ionospheric disturbances of the 2007 Bengkulu and the 2005 Nias earthquakes, Sumatra, observed with a regional GPS network. Journal of Geophysical Research: Space Physics, 118(4), 1777-1787.

Cahyadi, M., & Heki, K. (2013b). The Scaling Law of The Near-Field Coseismic Ionospheric Disturbances. In AGU Fall Meeting Abstracts (Vol. 2013, pp. NH13C-1625).

Cahyadi, M. N., & Heki, K. (2015). Coseismic ionospheric disturbance of the large strike-slip earthquakes in North Sumatra in 2012: M w dependence of the disturbance amplitudes. Geophysical journal international, 200(1), 116-129.

Cahyadi, M. N., Anjasmara, I. M., Khomsin, Yusfania, M., Sari, A., Saputra, F. A., ... & Rwabudandi, I. (2018, July). Coseismic ionospheric disturbances (CID) after West Sumatra earthquake 2016 using GNSS-TEC and possibility of early warning system during the event. In AIP Conference Proceedings (Vol. 1987, No. 1, p. 020019). AIP Publishing LLC.

Cahyadi, M. N., Audah, S., Mutia, N., & Aliyan, S. A. (2017, July). Analysis of weather changes in the region of Surabaya in 2015 and 2016 using water vapor data from GPS and terra MODIS satellite image. In AIP Conference Proceedings (Vol. 1857, No. 1, p. 080003). AIP Publishing LLC.

Cahyadi, M. N., Rahayu, R. W., Heki, K., & Nakashima, Y. (2020). Harmonic ionospheric oscillation by the 2010 eruption of the Merapi volcano, Indonesia, and the relevance of its amplitude to the mass eruption rate. Journal of Volcanology and Geothermal Research, 405, 107047.

Calais, E., & Minster, J. B. (1995). GPS detection of ionospheric perturbations following the 17 January 1994, Northridge earthquake. Geophysical Research Letters, 22(9), 1045-1048.

Comberiate, J. M., Kamalabadi, F., & Paxton, L. J. (2007). A tomographic model for ionospheric imaging with the Global Ultraviolet Imager. Radio Science, 42(02), 1-12.

Coster, A., Williams, J., Weatherwax, A., Rideout, W., & Herne, D. (2013). Accuracy of GPS total electron content: GPS receiver bias temperature dependence. Radio Science, 48(2), 190-196.

Daniels, F. B. (1952). Acoustical energy generated by the ocean waves. The Journal of the Acoustical Society of America, 24(1), 83-83.

Evelpidou, N., Karkani, A., & Kampolis, I. (2021). Relative sea level changes and morphotectonic implications triggered by the Samos earthquake of 30 October 2020. Journal of Marine Science and Engineering, 9(1), 40.

Feng, J., Zhou, Y., Zhou, Y., Gao, S., Zhou, C., Tang, Q., & Liu, Y. (2021). Ionospheric response to the 17 March and 22 June 2015 geomagnetic storms over Wuhan region using GNSS-based tomographic technique. Advances in Space Research, 67(1), 111-121.

He, L., & Heki, K. (2018). Three−dimensional tomography of ionospheric anomalies immediately before the 2015 Illapel earthquake, Central Chile. Journal of Geophysical Research: Space Physics, 123(5), 4015-4025.

Heki, K., & Cahyadi, M. N. (2012, December). Precursory changes in ionosphere immediately before mega-thrust earthquakes. In AGU Fall Meeting Abstracts (Vol. 2012, pp. NH43C-04).

Kakinami, Y., Kamogawa, M., Tanioka, Y., Watanabe, S., Gusman, A. R., Liu, J. Y., ... & Mogi, T. (2012). Tsunamigenic ionospheric hole. Geophysical Research Letters, 39(13).

Kunitsyn, V. E., Andreeva, E. S., & Razinkov, O. G. (1997). Possibilities of the near−space environment radio tomography. Radio Science, 32(5), 1953-1963.

Liu, J. Y., Chen, C. H., Lin, C. H., Tsai, H. F., Chen, C. H., & Kamogawa, M. (2011). Ionospheric disturbances triggered by the 11 March 2011 M9. 0 Tohoku earthquake. Journal of Geophysical Research: Space Physics, 116(A6).

Liu, J. Y., Tsai, Y. B., Ma, K. F., Chen, Y. I., Tsai, H. F., Lin, C. H., ... & Lee, C. P. (2006). Ionospheric GPS total electron content (TEC) disturbances triggered by the 26 December 2004 Indian Ocean tsunami. Journal of Geophysical Research: Space Physics, 111(A5).

Muslim, B., Cahyadi, M. N., Sunardi, B., & Kumalasari, C. J. (2020). THE SIMULATION STUDY OF GNSS SIGNAL REFLECTION IN MONITORING SEA LEVELS AND TSUNAMI. Science of Tsunami Hazards, 39(4).

Nakashima, Y., Heki, K., Takeo, A., Cahyadi, M. N., & Aditiya, A. (2014, December). Ionospheric disturbances by volcanic eruptions by GNSS-TEC: Comparison between Vulcanian and Plinian eruptions. In AGU Fall Meeting Abstracts (Vol. 2014, pp. NH33C-05).

Nakashima, Y., Heki, K., Takeo, A., Cahyadi, M. N., Aditiya, A., & Yoshizawa, K. (2016). Atmospheric resonant oscillations by the 2014 eruption of the Kelud volcano, Indonesia, observed with the ionospheric total electron contents and seismic signals. Earth and Planetary Science Letters, 434, 112-116.

Pryse, S. E., Mitchell, C. N., HEATON, J. T., & Kersley, L. (1995). Travelling ionospheric disturbances imaged by tomographic techniques. In Annales geophysicae (1988) (Vol. 13, No. 12, pp. 1325-1330).

Rolland, L. M., Occhipinti, G., Lognonné, P., & Loevenbruck, A. (2010). Ionospheric gravity waves detected offshore Hawaii after tsunamis. Geophysical Research Letters, 37(17).

Sharma, G., Mohanty, S., & Kannaujiya, S. (2017). Ionospheric TEC modelling for earthquakes precursors from GNSS data. Quaternary International, 462, 65-74.

Shults, K., Astafyeva, E., & Adourian, S. (2016). Ionospheric detection and localization of volcano eruptions on the example of the April 2015 Calbuco events. Journal of Geophysical Research: Space Physics, 121(10), 10-303.

Tsugawa, T., Saito, A., Otsuka, Y., Nishioka, M., Maruyama, T., Kato, H., Nagatsuma, T. & Murata, K.T., 2011. Ionospheric disturbances detected by GPS total electron content observation after the 2011 off-the-Pacific coast of Tohoku Earthquake, Earth Planets Space, 63, 875–879.

United States Geological Survey (USGS). 2020. M 7.0 - 13 km NNE of Néon Karlovásion, Greece. Accessed February 14, 2021, <https://earthquake.usgs.gov/earthquakes/eventpage/us7000c7y0/executive>

Yalciner, A. C., Dogan, G. G., Ulutas, E., Polat, O., Tarih, A., Yapa, E. R., & Yavuz, E. 2020. The October 30, 2020 (11:51 UTC) Izmir-Samos earthquake and tsunami: posttsunami field survey preliminary results.

ISSN 8755-6839

SCIENCE OF TSUNAMI HAZARDS

Journal of Tsunami Society International

Volume 40 Number 3 2021

EARTHQUAKE OF 30 OCTOBER 2020 IN THE AEGEAN SEA: NUMERICAL SIMULATION OF THE GENERATION AND PROPAGATION OF TSUNAMI WAVES

Mazova R.Kh.[1,2], Kurkin A.A.[1], Giniyatullin A. R.[1], Tyuntyayev C.M.[3]

[1]Nizhny Novgorod State Technical University n.a. R.E. Alekseev, 24, Minin str., 603950 Nizhny Novgorod, Russia. e-mail address: raissamazova@yandex.ru; aakurkin@gmail.com; adel.giniyatullin@gmail.com
[2]Moscow Institute of Physics and Technology (MIPT), Moscow Region, Russia
[3]Nizhny Novgorod , HARMAN, 8, Kovalikhinskaya st., 603006 Nizhny Novgorod, Russia., e-mail address: ser.tyuntyaev@gmail.com

ABSTRACT

The paper considers the earthquake in Samos on October 30, 2020 and the subsequent tsunami. Based on the data on both intensity of the earthquake and localization of the epicenter of the earthquake and aftershocks, taking into account the tectonic setting for this region, where active tension and shear deformations coexist, two possible sources of the earthquake were considered. Virtual sources have been constructed along the fault zone north of Samos. Using the keyboard model of the earthquake, the optimal kinematic movements of the keyboard blocks in the earthquake source were found, which most adequately describe the generation of the tsunami source and the propagation of tsunami waves to the coastal zone. 3D histograms of the distribution of the maximum wave heights along the coast were constructed and compared with the available field data and data from other authors.

Keywords: *tsunamigenic earthquakes, keyboard model, tsunami waves, numerical simulation.*

1. INTRODUCTION

The Eastern Mediterranean Sea is one of the most seismically active areas, including the Aegean Sea and Western Anatolia. The cause for this activity is the movement of the Anatolian block towards the Aegean Sea. The expansion rate of the Earth's crust between Samos and Western Anatolia (the wider region of Izmir) is 7.4 mm/yr based on GNSS data simulations [1-6]. Seismic activity is mainly focused on normal faults, which are formed due to the active expansion of the West Anatolian plate in the southern and northern directions (white arrows in Fig.1). Active parts of the North Anatolian fault act as a source of strike-slip faults in the North Aegean Sea, which are located up to the island of Samos [11]. The earthquake on Samos on October 30, 2020 occurred in the region between the eastern islands of the Aegean Sea and Western Turkey, where there is an active tectonic regime (Fig.1) [1-6]. The available mechanisms of earthquake sources clearly confirm the coexistence of deformations along the coastal region of Western Anatolia and the Aegean Sea [5,6,11,38,40].

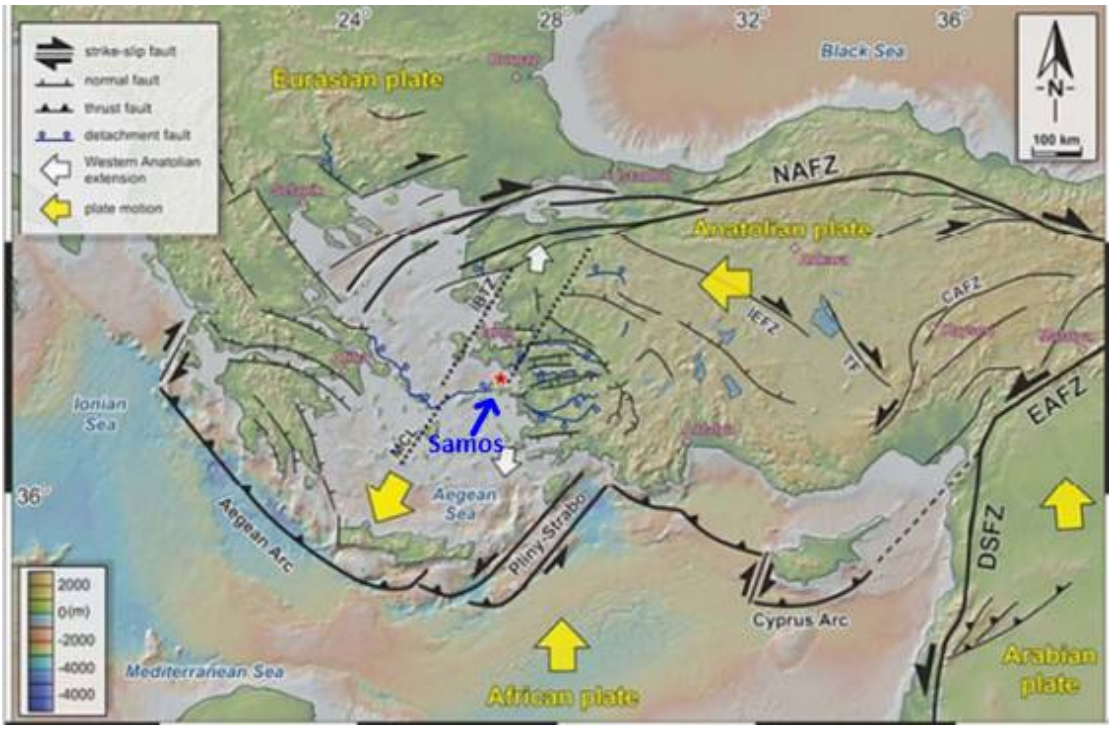

Fig. 1. Tectonic Map of Western Anatolia Region and the Aegean Sea [5, 6]. Yellow arrows indicate the motion of tectonic plates. The blue arrow points to the Samos Island. The red asterisk corresponds to the epicenter of the October 30, 2020 submarine earthquake**.**

The occurrence of large earthquakes in the 21st century and the associated tsunamis in the Mediterranean Sea is a great danger [39]. Turkey is crossed by large fault lines (see Fig.1), and is among the most earthquake-prone countries in the world [41-43]. For example, on August 17, 1999, off the coast of the Sea of Marmara in Turkey, there was an earthquake of magnitude $M = 7.5$. This earthquake caused great destruction, affecting even part of Istanbul. The tsunami that emerged after the earthquake (wave height 2.9 meters) hit the coastal areas of Turkey and led to their flooding [2,3].

It is well known that densely populated coastal areas in the Aegean Sea have been subject to several devastating tsunamis in the past (see, e.g., Altınok & Ersoy, 2000; Altınok et al., 2011; Ambraseys, 1962; Ambraseys & Synolakis, 2010; Dominey-Howes, 2002; Galanopoulos, 1960;

Kuran & Yalciner, 1993; Minoura et al., 2000; Papadopoulos & Chalkis, 1984; Papadopoulos et al., 2014; Soloviev et al., 1997; Tinti et al. 2001) [5,6]. The most famous tsunami in the region is the 1956 Amorgos event ($M \sim 7.8$), which caused waves up to 25 m high (Beisel et al. 2009; Okal et al. 2009; Papadopoulos & Pavlides, 1992; Papazachos, 1985; Yalciner et al. 1995) [5,6]. On October 30, 2020, a strong earthquake with a magnitude $M = 7.0$ occurred in the Aegean Sea, which was felt both in Greece and in Turkey [1,2, 21-23]. This earthquake epicenter was located north of the island of Samos in the area of the North Samos fault or the Kaistrios fault (Greece), with coordinates (37.88 N, 26.70 E) [5]. Initial estimates of magnitudes by various agencies ranged from 6.6 to 7.0 and the epicenter near (37.8919N; 26.8066E) [6,24]. The event with a magnitude of $M = 7.0$ slightly exceeds the maximum value expected for this subduction zone. Historical archives do not indicate an event of this magnitude on one or another local fault in the last 19 centuries (since 47 AD) [11-14]. Figure 2 shows a map of the water area with the epicenter of the earthquake and aftershocks, as well as the fault zone during the earthquake of October, 30, 2020 in the Aegean Sea [1-6].

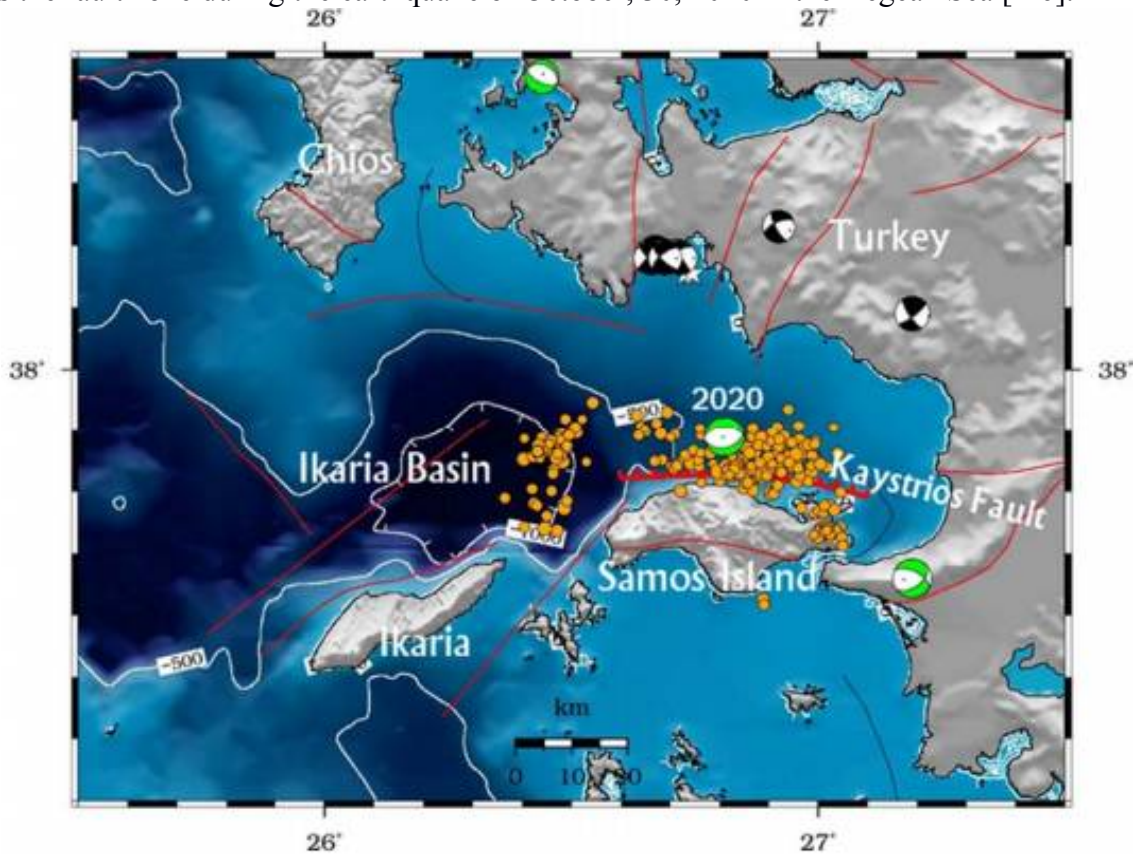

Fig. 2. Map of aftershocks and the epicenter of the earthquake on October 30, 2020. Samos, Greece. Bold red line north of Samos is the fault line [6]

As is known, aftershocks usually occur in the same fault or close to it at a distance of about twice the length of the fault zone, and the location of aftershock epicenters covers the zone of rupture of the main shock. It follows from the distribution of the aftershock sequence (Fig.2) that the fault occurred during the main shock $M = 7.0$, located off the northern coast of Samos Island. This fault in the region of Western Anatolia and the Aegean Sea can be identified as an oblique subduction zone [11].

Both countries experienced high tidal waves that led to flooding in parts of the Izmir coastline. The earthquake-triggered tsunami struck many nearby coastal areas. According to available materials, the water first receded from the coast, then soon the water returned, flooding low-lying coastal areas up to 1-2 meters high, including many coastal cities [5,6].

The tsunami generated by this earthquake was recorded in both Greece and Turkey [1]. The tsunami occurred as a sequence of sea level sink and surge [5]. The results of field studies following this event, carried out by a team of researchers along the 110 km coastline, demonstrated "… a significant tsunami impact. The maximum tsunami height in the area of pp. Kaleici in Sigacik was 2.3 m, " [5]. The results of this field study provide insight into the impact of near-field tsunamis on the coasts of the Aegean Sea.

In this work, based on both data on the intensity of the earthquake and the localization of the epicenter of the earthquake and aftershocks, taking into account the data on the subduction zone [1-6] (Table 1), two possible model sources of the earthquake were constructed.

Table 1. Parameters of the earthquake of October 30, 2020 in the Aegean Sea [6]

Earthquake Magnitude	**7.0M**
Depth	**21 km**
Lat/Lon	**37.9175, 26.7901**
Event Data	**30 Oct 2020 11:51 UTC** **30 Oct 2020 13:51 Local**

The two-block and three-block earthquake sources located along the fault zone running to the north of the island of Samos are considered. Using keyboard model of the earthquake [27], which is briefly described in the next section, the optimal kinematic movements of the keyboard blocks in the earthquake source were found, which most adequately describe the generation of the tsunami source and the propagation of tsunami waves to the coastal zone.

2. ANALYSIS OF THE TSUNAMI SOURCE GENERATION MECHANISM

It is well known that the strongest earthquakes occur in fault zones, which are clearly visible on the bathymetric map (Fig.2), where the earthquake in question occurred. Since a strong earthquake as a result of the rapid movement of the seabed triggers a tsunami over its source zone, the vertical component of the dynamic displacement of rocks (schematically represented by the keyboard blocks) gives the displacement at the ocean surface, i.e. a tsunami source is formed [25]. The formation of a tsunami is influenced by the nature and dynamics of displacements in the zone of the earthquake source [26]. To compute the generation of tsunami waves, as a rule, seismic data are used, which make it possible to determine the orientation of the rupture in the source and the energy of the tsunami (see, for example, [44]).

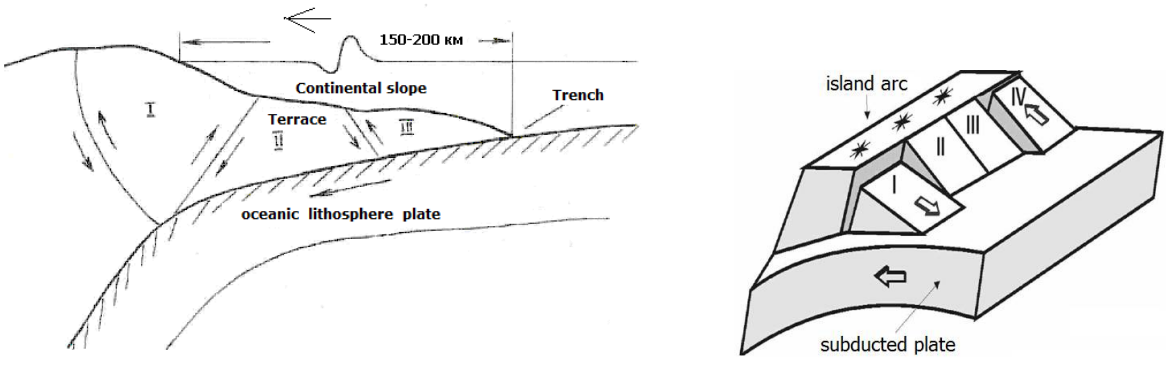

a) **b)**

Fig. 3. a) Schematic representation of the frontal part of the island arc; b) Keyboard model of the blocks structure in the frontal part of the island arc [27].

In this paper, we consider the final fault with parameters obtained on the basis of the data given in [5]. The earthquake source is considered within the framework of a simplified keyboard model of the subduction zone [27]. Figure 3 shows a schematic representation of the block structure of the frontal part of the continental slope and the interaction of its main elements with the driven plate and with each other [27]. In Fig. 3a, one can see transverse faults - ruptures and movements in the source of tsunamigenic earthquakes. Figure 3b shows a model image of a subduction zone - a keyboard model of an earthquake source [27].

Since the question of the mechanism of the seismic source for an earthquake is still open [25], then setting the source mechanism from tectonic considerations, and using the Wells formula [33], based on the magnitude of the earthquake of a given event, we get an opportunity to calculate approximate data on the length of the rupture in the source and the width of the rupture plane. The vertical component of the wave surface displacement above the source of the earthquake is found via the Iida formula (see, for example, [26]). Thus, using formulas (1) and (2), the characteristics of the seismic source and the displacement of the water surface above the source of the earthquake were obtained (Table 2).

$$\lg L\,(km) = 0{,}59\,M - 2{,}44 \pm 0.16 \quad , \qquad (1)$$

$$\lg W(km) = 0{,}32\,M - 1{,}01 \pm 0.15$$

$$\lg(H, m) = 0{,}8M - 5{,}6 \pm 0.4 \qquad (2)$$

where M is the magnitude of the earthquake, L is the length of the rupture in the source (km), W is the width of the rupture plane (km), H is the maximum height of the vertical displacement of the water surface above the seismic source (m). Since the processes occurring in the seismic source during a strong earthquake (up thrust or fault) are ultimately recalculated into vertical displacement, then, due to the hydrodynamic problem under consideration, with an instantaneous piston movement, the ocean surface will rise by the same amount as the block at the bottom [26]. Depending on the speed of movement of the keyboard blocks in the seismic source, various scenarios for the formation of a tsunami source on the water surface can be realized. Using (2), the estimated displacements of the Earth's crust in the earthquake source were obtained (see Table 2).

Table 2. Characteristic parameters of the earthquake source and displacement of the Earth's crust in the source during the earthquake on October 30, 2020 in the Aegean Sea.

Parameter	Characteristic parameters of earthquake 10.30.2020
Magnitude of the earthquake	**7**
The length of the rupture plane (km)	**34**
Width of the rupture plane (km)	**12**
Water surface displacement (m)	**1,2**

So, for the earthquake under consideration at $M = 7$, the approximate values of the size of the earthquake source obtained by (1) and the maximum displacement height in the earthquake source of about 1.2 m found by (2) are used to simulate the generation of the tsunami source and further propagation of waves across the water area.

Figure 4 shows the water area under consideration with the marked epicenter of the earthquake and aftershocks of the first day of the earthquake, as well as with points located on the continental and island coasts of the water area, where tsunami waves were recorded.

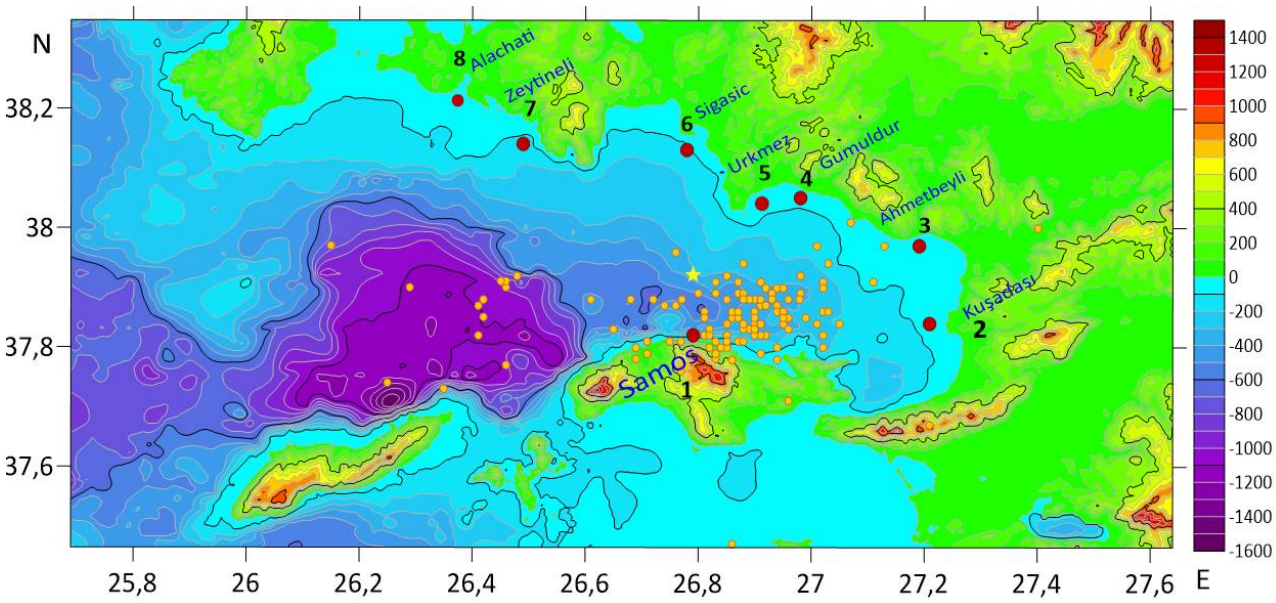

Fig. 4. The considered water area, the epicenter of the earthquake and aftershocks of the first day of the earthquake on October 30, 2020 in the Aegean Sea. The red dots mark the position of the virtual tide gauges.

3. MATHEMATICAL FORMULATION OF THE PROBLEM

To consider the process of generating tsunami waves in the keyboard model of a seismic source and their propagation over the water area, we will use the shallow water equations (see, e.g. [35]). The geometry of the problem is shown in Fig. 5. The schematic sketch at the bottom is presented in the form of a rectangular keyboard block, height B (x, y, t) and transverse dimensions, limited by the vertical sides of the rectangle; α is the angle of inclination of the shelf to the horizon, L_{sh} is the shelf length [28-32].

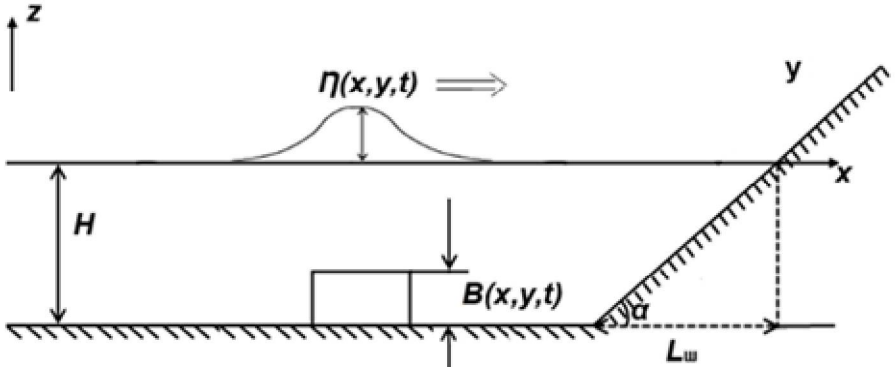

Fig. 5. Schematic representation of wave generation.

In 2D case, the system of nonlinear shallow water equations can be written as [35]

$$\begin{cases} \dfrac{\partial u}{\partial t}+u\dfrac{\partial u}{\partial x}+v\dfrac{\partial v}{\partial y}+g\dfrac{\partial \eta}{\partial x}=0 \\ \dfrac{\partial v}{\partial t}+u\dfrac{\partial v}{\partial x}+v\dfrac{\partial v}{\partial y}+g\dfrac{\partial \eta}{\partial y}=0 \\ \dfrac{\partial \eta}{\partial t}+\dfrac{\partial}{\partial x}[(\eta+H-B)u]+\dfrac{\partial}{\partial y}[(\eta+H-B)v]=\dfrac{\partial B}{\partial t} \end{cases} \quad (3)$$

here $u\ (x, y, t)$, $v\ (x, y, t)$ are the velocity components, $h\ (x, y, t)$ is the disturbance of the free surface, $H\ (x, y)$ is the depth of the basin, $B\ (x, y\ , t)$ is the change in the bottom of the basin (taking into account the characteristics of the dynamic seismic source), g is the acceleration of gravity. In this work, $B(x,y,t)$ is the function describes the sequential movement of the keyboard blocks. The modeling of such a process in the earthquake source, which would most fully correspond to possible movements occurring in the vicinity of the earthquake source in the first minutes after the onset of the earthquake, is considered.

4. NUMERICAL SIMULATION

From the set of difference schemes approximating Eqs. (3), the numerical scheme of Sielecki and Wurtele was taken [34], modified for computation the generation of a long wave by a dynamic underwater source, which has a second order of approximation. The paper presents two possible scenarios for the realization of the movements of the Earth's crust in the seismic source during the earthquake of October 30, 2020 in the water area of the Aegean Sea.

SCENARIO 1

In Scenario 1, a virtual earthquake source is considered, segmented into 2 blocks, located along the island zone where the earthquake occurred. Based on the data obtained on the earthquake source size (Table 2), as well as the data on the localization of the epicenter of the earthquake and aftershocks [6] and also, taking into account the tectonic setting for this region, where active tension and shear deformations coexist [5], the bathymetry of the considered water area there were built two possible sources of the earthquake. Figure 6 shows a bathymetric map of the computed water area. The red line outlines the virtual seismic source of the earthquake, segmented into 2 blocks. The burgundy line marks the fault line during the earthquake of October 30, 2020 in the Aegean Sea. Blue dots mark points on the coast for which there is documentary data on the tsunami run-up.

Table 3 shows the characteristics for the kinematic motion of two blocks in the earthquake source. The movement begins with the first block, moving vertically upward for 15 s to a height of 1.2 m. 5 s after the beginning of the movement of the first block, the second block begins to move vertically downward at a distance of 1m, the movement occurs for 10 s, and ends simultaneously with the rise of the first block. Then, after 3 s, the same block is shifted upward to a height of 0.8 m. The total movement time of the blocks is 24 s [6].

Table 3. Characteristics of the kinematic movement of blocks for Scenario 1.

Block number	1	2	2
Start time (s)	0	5	18
Final time of movement (s)	15	10	6
Height of movement (m)	1,2	-1	0,8

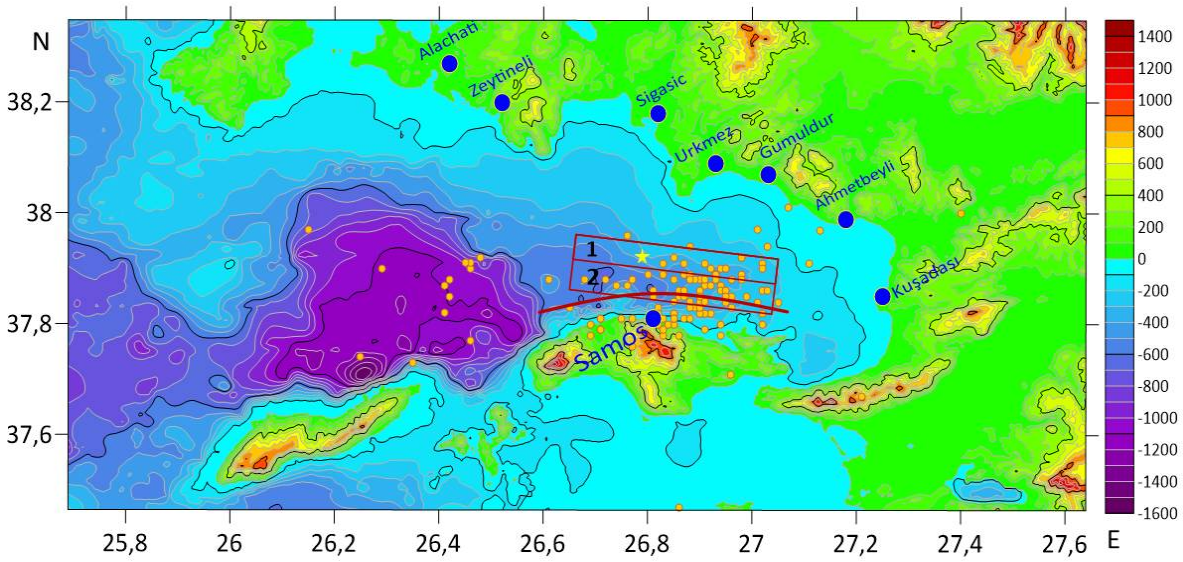

Fig. 6. Schematic representation of a two-block earthquake source on October 30, 2020 in the Aegean Sea (Scenario 1). The bold red line is the fault line. Blue points indicate localization of 8 points under consideration on the coast.

Fig.7-9 show the simulation results for Scenario 1. Fig.7 shows the generation of the tsunami source. Since, due to the incompressibility of the liquid and the hydrostatic pressure, the ocean surface will rise by the same amount by which the block at the bottom has been displaced [26], then, according to the parameters of Table 3, panel 1 (Fig. 6) shows the displacement of the water surface when the first block rises. 5 s after the start of the movement, block 2 begins to move downward, which corresponds to the displacement of the wave surface above the second block (panel 2). The movement of block 2 ends in 10 s simultaneously with the stop of block 1. After a 3 s delay, block 2 begins to move upward, which leads to an upward shift (panel 4). Thus, the source of the tsunami, i.e. displacement of the wave surface, is formed in 24 s, after which the wave propagates over the sea area.

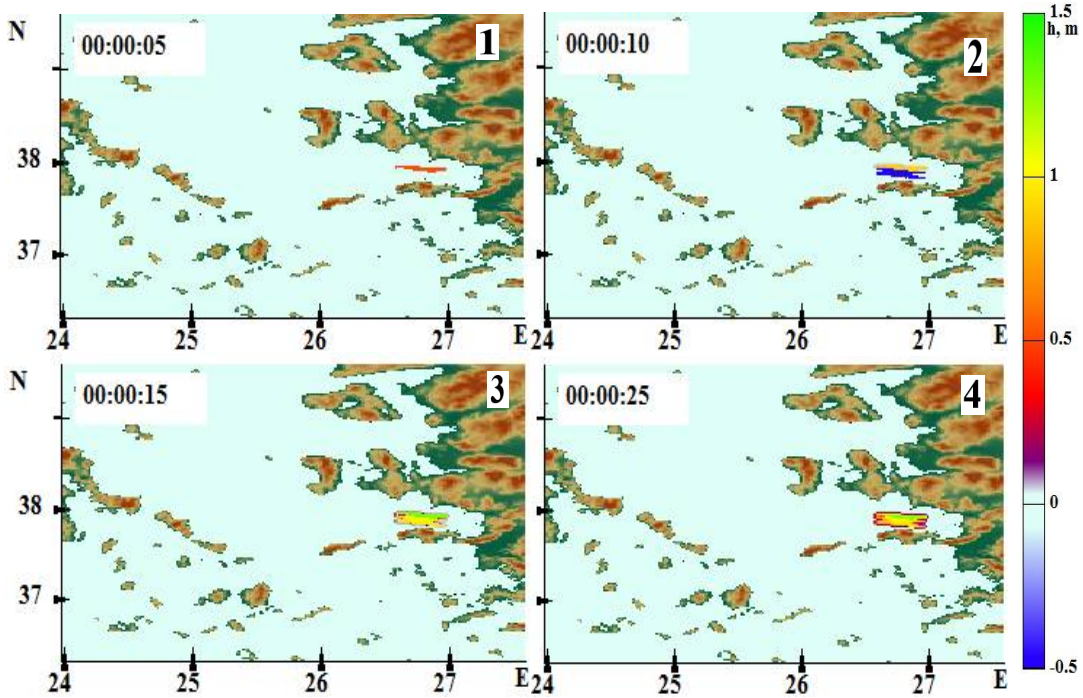

Fig. 7. Generation of a tsunami source during the implementation of Scenario 1 for four time points.

Figure 8 (panels 1-8) shows the position of the wave fronts. It is clearly seen that after about 2min 30s (panel 1) waves with a height of 1.25m reach the Samos Island.

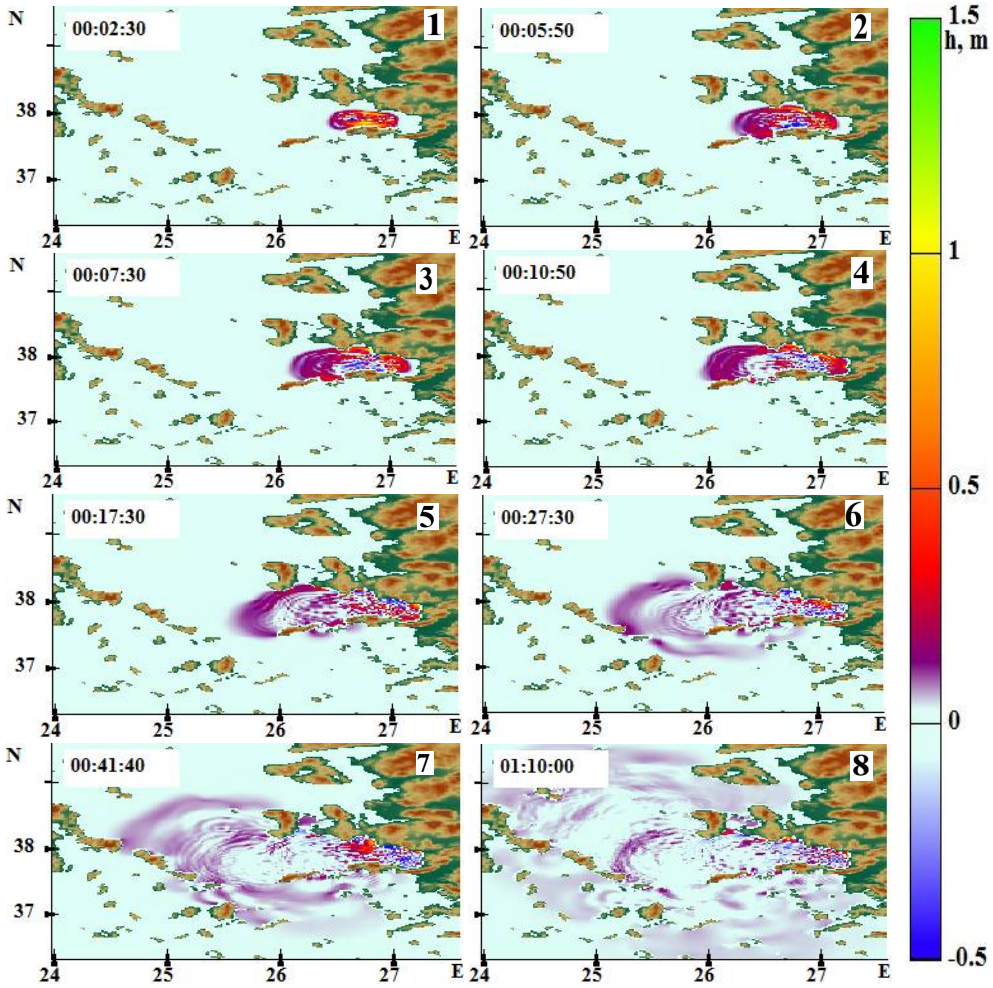

Fig.8. Propagation of wave fronts in the implementation of Scenario 1 for eight time points.

After 5min 50s (panel 2), the wavefront reached the coastal city of Urkmez. For 7 min 30 s (panel 3) a wave with a height of 1.06 m reached the city of Ahmetbeyli, and after about 10 min and 50 s, the front reached the largest city on the coast - Kusadasi 1.2 m (panel 4). At 17.5 min, we see a height of about 1.31m in the area of the city of Zeytineli (panel 5). In 27.5 min in the coastal town of Alacati, the height reached 0.92 m (panel 6).

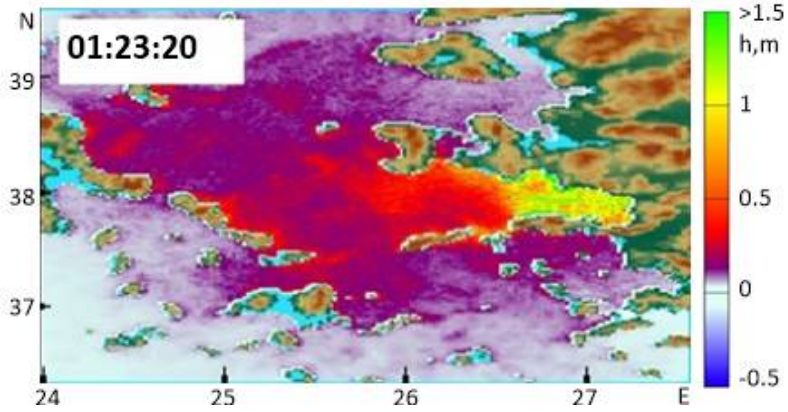

Fig. 9. Distribution of maximum wave heights over the water area during the implementation of Scenario 1.

Figure 9 shows the distribution of the maximum wave heights over the entire computed area. The distribution of the maximum wave heights clearly shows that the most dangerous areas are near-field points, namely the island, the cities of Izmir and Kusadasi. Fig.10 shows a 3D histogram of the distribution of the maximum heights of tsunami waves along the coasts of the computed water area. It can be seen that the maximum wave height in the area of Kusadasi does not exceed 0.6 m. On the island of Samos, heights vary from 0.6 to 1.7 m from west to east. On the coast of the city of Urkmez, the maximum wave height reached 1.3 m, but decreases towards the Pamudjak beach to 0.5 m.

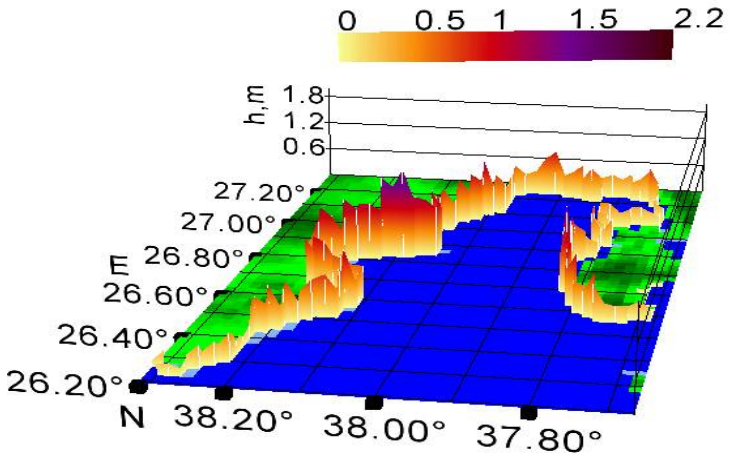

Fig. 10. 3D histogram for a two-block source in the implementation of Scenario 1.

It should be noted that the observed maximum wave heights near the coast, which are closer to the source, are many times higher than those located at more distant points from the earthquake source.

SCENARIO 2

In Scenario 2, a virtual earthquake source is considered, segmented into 3 blocks, located along the fault zone where the earthquake occurred. It can be seen that the arrangement of the blocks follows the line of the oblique subduction zone (Fig. 11). Table 4 shows the characteristics for the motion of three blocks in the earthquake source. The movement begins with the second block, moving vertically upward for 15 s to a height of 1.2 m in 15 s. 5 s after the start of the movement of the first block, the third block begins to move upward at a distance of 1 m in 15 s. 5 s after that, the third block begins its downward movement by 0.8 m in 14 s. The total movement time of the blocks is 24 s [6].

Table 4. Characteristics of the kinematic movement of blocks for Scenario 2.

Block number	2	3	1
Start time (s)	0	5	10
Final time of movement (s)	15	15	14
Height of movement (m)	1,2	1	-0,8

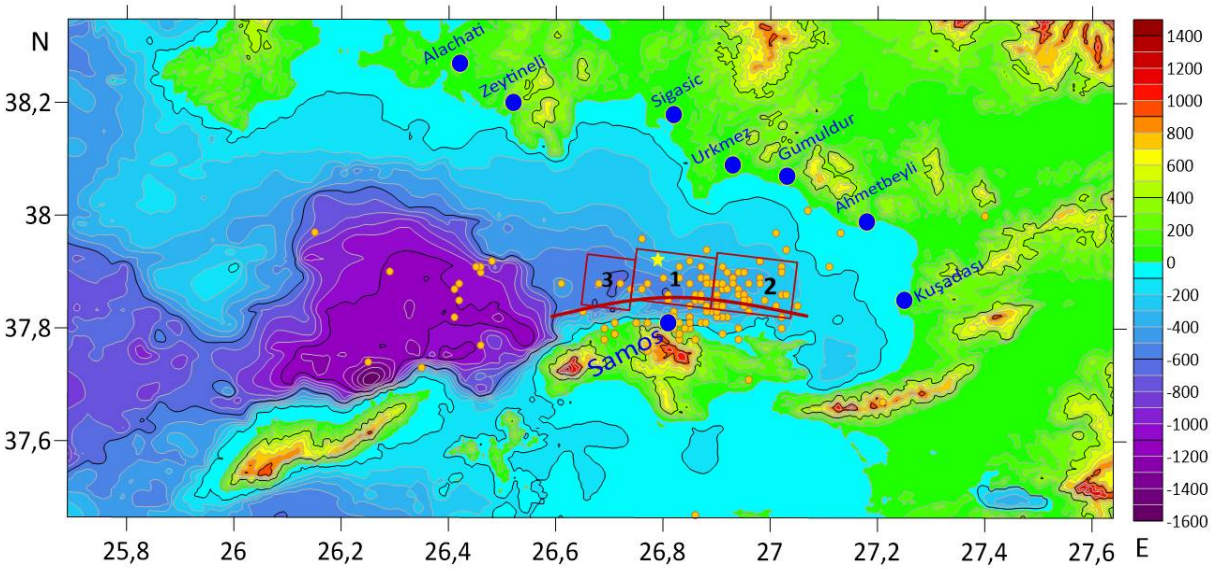

Fig. 11. Schematic representation of the three-block source of the earthquake on October 30, 2020 in the Aegean Sea. The bold red line is the fault line. Blue points indicate localization of 8 points under consideration on the coast.

The computation results for a three-block source are shown in Figures 11-13. In Fig. 12 it can be seen that, according to the dynamics of the movement of blocks in the earthquake source: first, block 2 moves up, then, 5 s after the beginning of the movement of the first block, block 3 begins to move and then, block 1 moves down (Table 4), occurs displacement of the water surface above the blocks and the formation of a tsunami source.

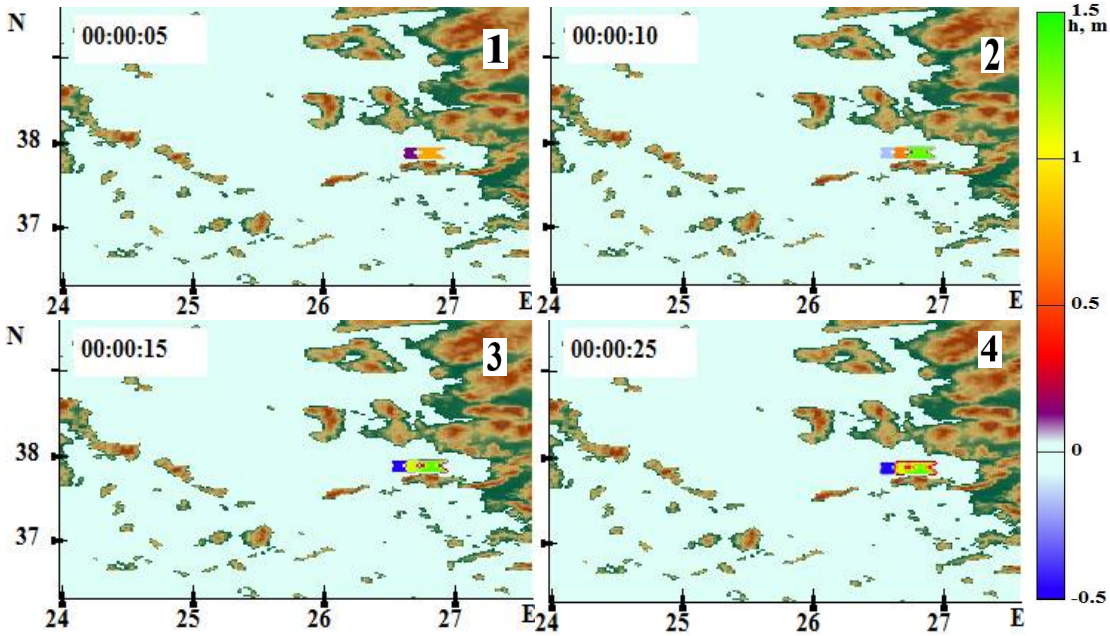

Fig. 12. Generation of the tsunami source in the implementation of Scenario 2 for 4 time points.

Figure 13 shows the propagation of wave fronts in the implementation of this scenario over the computed water area.

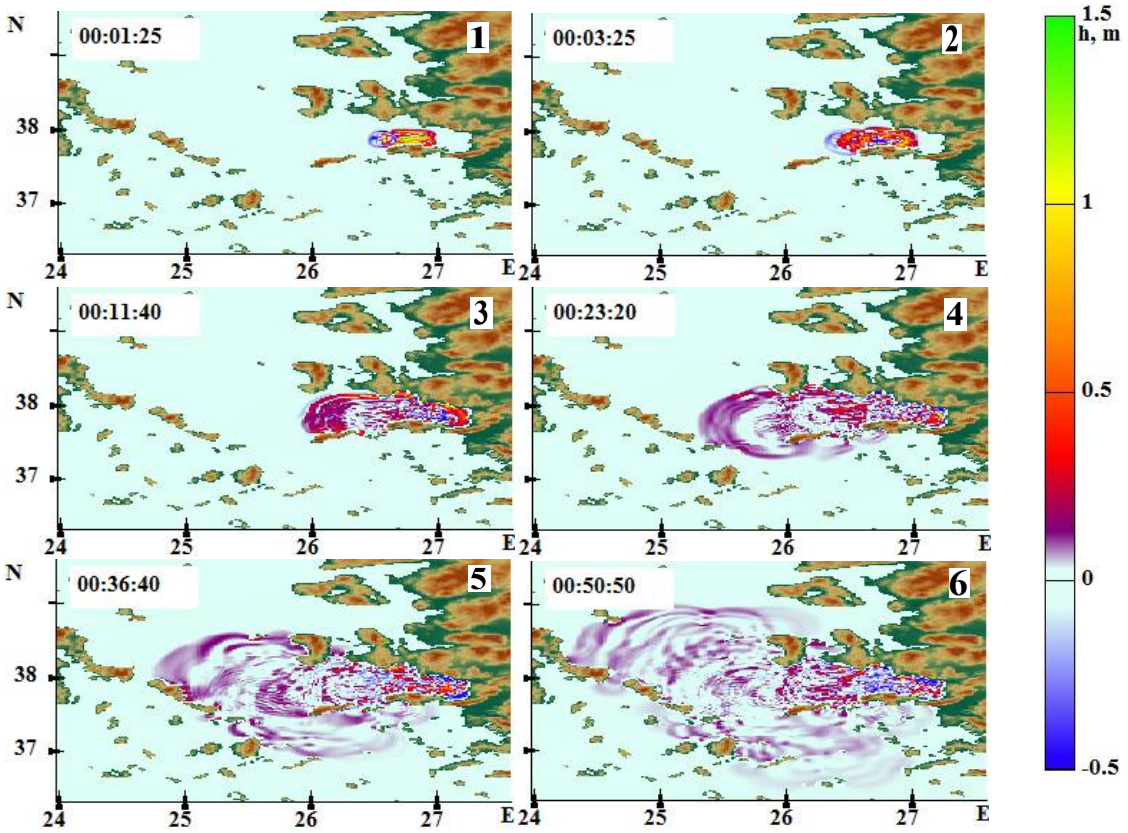

Fig. 13. Propagation of wave fronts in the implementation of Scenario 2 for 6 time moments.

It is clearly seen that after about 1 min 25 s (panel 1) waves with a height of 1.31 m reach the Samos Island. After 3 min 25 s (panel 2), the wave front reached the coastal town of Urkmez 1.65 m. At 11:40 a.m. (panel 3) a wave with a height of 1.26 m reached the city of Ahmetbeyli, and after about 23:20 min the front reached the largest city on the coast - Kusadasi 1.14m (panel 4). At 36:40, a height of about 1.0 m is seen in the area of the city of Zeytineli (panel 5). At 55:50 the wave reached the entire coastline, in the coastal town of Alacati the height reached 0.6 m (panel 6).

Figure 14 shows the 3D distribution of the maximum wave heights along the coasts of the considered water area. It can be seen that the most dangerous areas are near-field points, namely the island of Samos, the cities of Izmir and Kusadasi. The maximum wave height in the area of Kusadasi does not exceed 0.5 m. On the island of Samos, heights vary from 0.5 to 1.8 m from west to east. On the coast of the city of Urkmez, the maximum wave height reached 1.03 m, but decreases towards the Pamudjak beach to 0.36 meters. The observed maximum wave heights near the coast, which are closer to the source, are many times higher than those located at more distant points from the source of the earthquake.

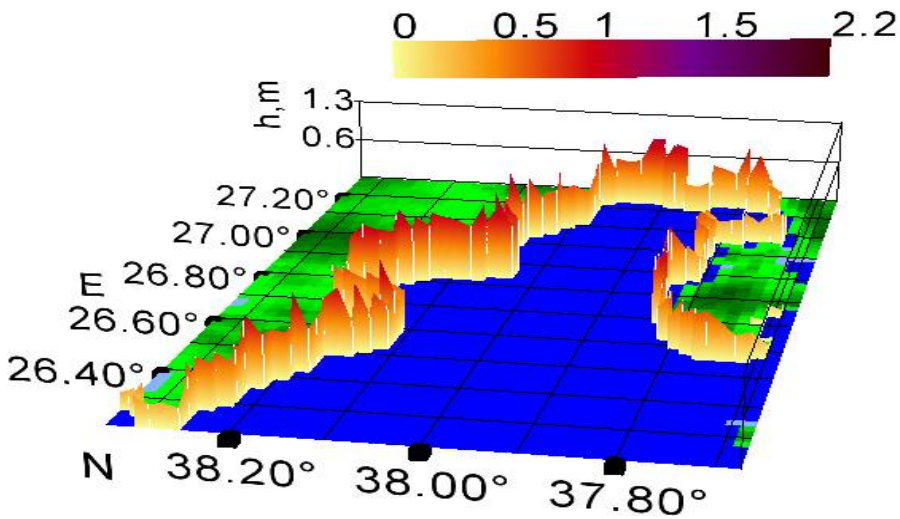

Fig. 14. 3D histogram for a three-block source in the implementation of Scenario 2.

Fig. 15 shows data from virtual tide gauges when computed according to Scenario 2. It is clearly seen that the first displacement on tide gauges corresponds to the character of the tsunami wave run up to this point (see, for example, [5,6]).

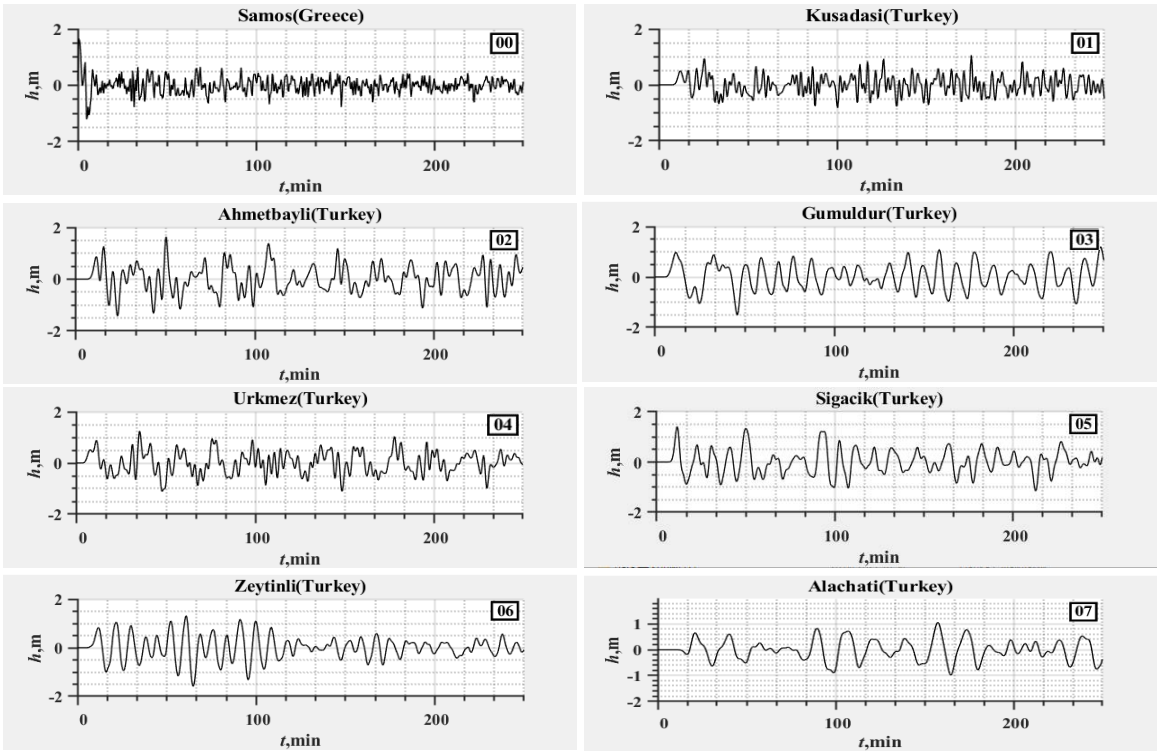

Fig. 15. The virtual tide-gauge records for points 1-8 (Scenario 2).

5. COMPARISON OF COMPUTATION RESULTS WITH REAL DATA AND DATA OF OTHER AUTHORS

Table 5 shows a comparison of computed data with real ones taken from work [6]. It is clearly seen that the results of the first computation (Scenario 1) for a two-block source are rather far from real data. Taking into account the presence of an oblique subduction zone (see Fig. 5, red fault line), the earthquake source was considered in more detail describing this fault zone (see Fig. 10). Using the available characteristics of the earthquake and manifestations of tsunami waves at specific points on the coast (see, for example, [6]), a number of scenarios for the kinematic movement of blocks in the earthquake source of this form were considered, one of which is given in this work (Scenario 2). The results of numerical simulations for Scenario 2 show a closer agreement with field data than for Scenario 1. Some difference between arrival times observed is due to problem with location of real and virtual tide gauges in computations and real event. Moreover, the arrival time in several points was estimated during post-event field survey only from eyewitness accounts and photos.

Table 5. Comparison of computation results with documentary data.

Point	Real data on wave height on the beach, м	Wave height at 3m isobate (Scenario 1), м	Wave height at 3m isobate (Scenario 2), м
1.Samos (Greece)	1.8 [24]	1.23	1.65
2.Kusadasi (Turkey)	1.5 [6]	1.05	1.06
3.Ahmetbayli(Turkey)	1.34 [6]	1.04	1.64
4.Gumuldur (Turkey)	1.86 [6]	1.14	1.20
5.Urkmez (Turkey)	1.68 [6]	1.16	1.24
6. Sigacik (Turkey)	1.5 [6]	1.44	1.40
7.Zeytinli (Turkey)	1.5 [6]	1.24	1.31
8. Alachati (Turkey)	1.00 [6]	0.60	1.05
9.Bodrum (Turkey)	0.04 [5]	0.048	0.061
10.Kos (Greece)	0.10 [5]	0.042	0.061
11.Syros (Greece)	0.080 [5]	0.066	0.083
12.Plomari (Greece)	0.05 [5]	0.082	0.075

The distribution of the maximum wave heights over the computation water area is clearly seen in Figures 16 and 17, which show the data of numerical simulation according to scenario 2 and data from [6]. It can be seen that the distribution pattern along the coastal zone is fairly close.

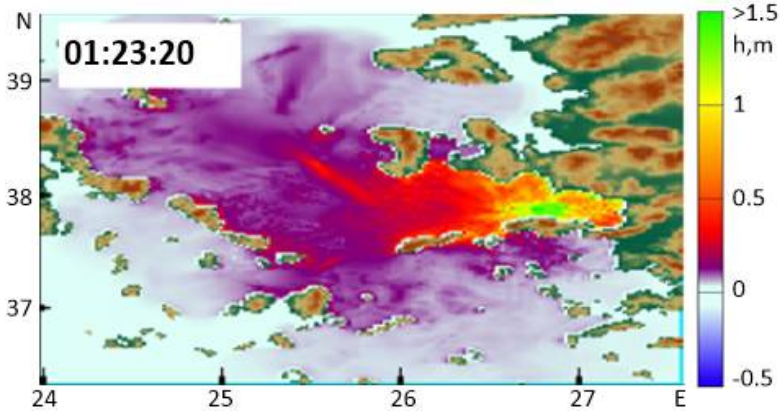

Fig. 16. Distribution of maximum water surface elevations in Eastern Aegean computed in the far-field simulations within the keyboard model of the earthquake source.

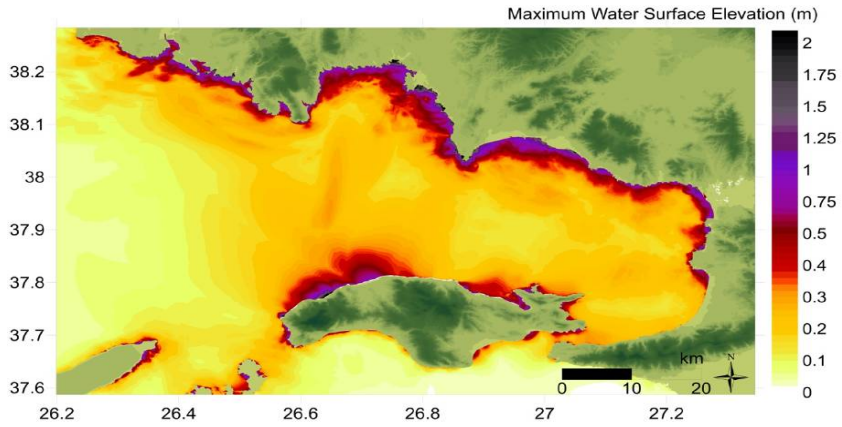

Fig. 17. Distribution of maximum water surface elevations in Eastern Aegean computed in the far-field simulations via NAMI DANCE [6].

6. CONCLUSIONS

The paper considers one of the strong tsunamigenic earthquakes that occurred in the Aegean Sea in the 21st century. Using the keyboard model of the earthquake source, two variants of seismic sources were considered: two-block and three-block sources, localized along the fault zone. Based on the data of available tide gauge records [5] and works on the analysis of tsunami wave manifestations on a number of coasts of the Aegean Sea [1], a dynamic process in the earthquake source generating tsunami waves was numerically simulated. The closest results were obtained when considering the generation of a tsunami by a three-block source (Scenario 2). The computations were carried out up to the 3-meter isobath, which is associated with complex coastal bathymetry and which made it possible to reduce the computation time. Since the goal of numerical modeling is to obtain an adequate distribution of the maximum wave heights along the considered coasts, it can be seen that the data obtained agree with this process well. It should be noted that when modeling according to Scenario 2, for a number of points under consideration, where tide gauge data were absent, but coastal survey data are well represented, the results obtained showed somewhat underestimated values. However, taking into account that, when recalculated from the isobath to the dry coast, the height of the maximum tsunami run-up may increase (see, for example, [36,37], it can be concluded that the numerical simulation data are in good agreement with the documented data (see Table 5).

ACKNOWLEDGEMENTS

The authors acknowledge the funding of this study provided by grant of President of the Russian Federation for the state support of Leading Scientific Schools of the Russian Federation (Grant No. NSH-2485.2020.5).

REFERENCES

1. http://www.ioc-sealevelmonitoring.org/ Tsunami Bulletin Board, Tsunami Information Center (ITIC)
2. http://www.en.unesco.org
3. http://www.gdacs.org
4. https://accelnet.gein.noa.gr/2020/11/09/the earthquake of october 30th 2020 atsamos eastern aegean sea greece preliminary report/
5. Dogan G.G., A.C.Yalciner, Y.Yuksel, E.Ulutaş, O.Polat, I.Güler, C.Şahin, A.Tarih, U.Kânoğlu *The 30 October 2020 Aegean Sea Tsunami: Post-Event Field Survey Along Turkish Coast //* Pure Appl Geophys 178, No.3, 785–812 (2021);
6. Cetin, K.O.; Mylonakis, G.; Sextos, A.; Stewart, J.P. Seismological and Engineering Effects of the M 7.0 Samos Island (Aegean Sea) Earthquake; Report GEER-069; Geotechnical Extreme Events Reconnaissance Association: Alameda County, CA, USA, 2021.
7. Altınok, Y., Alpar, B., Ozer, N., & Vardar, H. (2011). Revision of the tsunami catalogue affecting Turkish coasts and surrounding regions. Natural Hazards and Earth System Sciences, 11(2), 273–291.
8. Altınok, Y., & Ersoy, S. (2000). Tsunamis observed on and near the Turkish coast. Natural Hazards, 21, 185–205
9. Ambraseys, N. N. (1962). Data for the investigation of the seismic sea-waves in the Eastern Mediterranean. Bulletin of the Seismological Society of America, 52(4), 895–913.
10. Ambraseys, N., & Synolakis, C. (2010). Tsunami catalogs for the Eastern Mediterranean, revisited. Journal of Earthquake Engineering, 14(3), 309–330.
11. Kuran, U., & Yalciner, A. C. (1993). Crack propagations, earthquakes and tsunamis in the vicinity of Anatolia. In S. Tinti (Ed.), Tsunamis in the world. Advances in natural and technological hazards research (Vol. 1, pp. 159–175). Springer. https://doi.org/ 10.1007/978-94-017-3620-6_13
12. Minoura, K., Imamura, F., Kuran, U., Nakamura, T., Papadopoulos, G. A., Takahashi, T., & Yalciner, A. C. (2000). Discovery of Minoan tsunami deposits. Geology, 28(1), 59–62.
13. Papadopoulos, G. A., & Chalkis, B. J. (1984). Tsunamis observed in Greece and the surrounding area from antiquity up to the present times. Marine Geology, 56(1–4), 309–317.
14. Papadopoulos, G. A., Gra`cia, E., Urgeles, R., Sallares, V., De Martini, P. M., Pantosti, D., et al. (2014). Historical and prehistorical tsunamis in the Mediterranean and its connected seas: geological signatures, generation mechanisms and coastal impacts. Marine Geology, 354, 81–109.
15. Tinti, S., Maramai, A., & Graziani, L. (2001). A new version of the European tsunami catalogue: updating and revision. Natural Hazards and Earth System Sciences, 1, 255–262.
16. Beisel, S., Chubarov, L., Didenkulova, I., Kit, E., Levin, A., Pelinovsky, E., et al. (2009). The 1956 Greek tsunami recorded at Yafo, Israel, and its numerical modeling. Journal of Geophysical Research Oceans, 114, C09002. https://doi.org/10.1029/ 2008JC005262
17. Okal E.A., Synolakis C.E., Uslu B., Kalligeris N., & Voukouvalas E. (2009). The 1956 earthquake and tsunami inAmorgos, Greece. Geophysical Journal International, 178(3), 1533–1554.
18. Papadopoulos, G. A., & Pavlides, S. B. (1992). The large 1956 earthquake in the South Aegean: macroseismic field configuration, faulting, and neotectonics of Amorgos Island. Earth and Planetary Science Letters, 113(3), 383–396.

19. Papazachos, B. C., Koutitas, C., Hatzidimitriou, P. M., Karacostas, B. G., & Papaioannou, C. A. (1985). Source and short-distance propagation of the July 9, 1956 southern Aegean tsunami. Marine Geology, 65(3–4), 343–351.
20. Yalciner, A. C., Kuran, U., Akyarli, A., & Imamura, F. (1995). An investigation on the propagation of tsunamis in the Aegean Sea by mathematical modeling. In Y. Tsuchiya & N. Shuto (Eds.), Tsunami: progress in prediction, disaster prevention and warning. Advances in natural and technological hazards research (Vol. 4, pp. 55–70). Springer. https://doi.org/10.1007/978-94-015-8565-1_4
21. Kalogeras I., N.S. Melis, N. Kalligeris, *The earthquake of October 30th, 2020 at Samos, Eastern Aegean Sea, Greece,* https://accelnet.gein.noa.gr/ Reports/Samos_ Preliminary_ Report_EN.pdf (last access 16/2/2021).
22. Triantafyllou, I, Gogou, M, Mavroulis, S, Katsetsiadou, KN, Lekkas, E, and Papadopoulos, G, 2020. The tsunami caused by the 30 October 2020 Samos (Greece), East Aegean Sea, Mw6.9 earthquake: impact assessment from post□event field survey and video records. Report published at EMSC: https://edcm.edu.gr/images/docs/2020/Samos2020□TSUNAMI□REP/ pdf
23. Tani O., E.E. Papadimitrious, Z. Pabuccu, V.Karakostas, A.Yoruk, and K.Leptokaropoulos A *Detailed Analysis of Microseismicity in Samos and Kusadasi (Eastern Aegean Sea) Areas* // Acta Geophysica (2014) 62(6), 1283-1309. DOI: 10.2478/s11600-013-0194-1.
24. Triantafyllou I., M.Gogou, S.Mavroulis, E.Lekkas, G.A.Papadopoulos, M.Thravalos *The Tsunami Caused by the 30 October 2020 Samos (Aegean Sea)Mw7.0 Earthquake: Hydrodynamic Features, Source Properties and Impact Assessment from Post-Event Field Survey and Video Records* // J. Mar. Sci. Eng. (2021), 9, 68. https://doi.org/10.3390/jmse9010068
25. Garagash I.A., L.I. Lobkovski, (2006). *An analysis of the dynamic displacement process of the sea bottom due to a subduction zone earthquake*. In: Proc. of 4th International FLAC Symposium on Numerical Modeling in Geomechanics (eds. Hart & Varona). Paper: 06-01 © 2006 Itasca Consulting Group, Inc., Minneapolis, ISBN 0-9767577-0-2
26. Pelinovsky, E.N. Hydrodynamics of Tsunami Waves (1996) // IAP RAS, Nizhny Novgorod, Russia.
27. Lobkovsky L.I., Baranov B.V. Keyboard model of strong earthquakes in island arcs and active continental margins, (1984) // Doklady. V.75. No. 4. S. 843-847.
28. Lobkovsky L.I., R.Mazova, Baranov B.V., Kataeva L.U. (2006), Generation and propagation of tsunamis in the Sea of Okhotsk: possible scenarios // Doklady, pp.528-532.
29. Lobkovsky L.I., R.Mazova, Baranov B.V., Kataeva L.U. (2006). Tsunami modeling in the Sea of Okhotsk based on the keyboard model of the subduction zone // in the book: Fundamental research of the oceans and seas (edited by N. Laverov), Moscow: Nauka, book 1, p. 292-303.
30. Lobkovsky L.I., Mazova R.Kh., Kolchina E.A. (2014) *Estimation of Maximum Heights of Tsunami Waves for the Sochi Coast from Strong Submarine Earthquakes*, Doklady. Earth Sciences V.456, PP. 749–754. DOI:10.1134/S1028334X14060269
31. Lobkovsky L., R.Mazova, S.Tyuntyaev, I.Remizov, (2016). *Features and Problems with Historical Great Earthquakes and Tsunamis in the Mediterranean Sea* // Journal Science of Tsunami Hazards, Vol. 35, .No. 3, pp. 167 – 188.
32. Mazova R.Kh., Moiseenko T., Kurkin A.A., Jorge Van Den Bosch F., Gustavo Oses A. (2021). *Numerical Simulation of a Catastrophic Earthquake and Strong Tsunami of April 1, 2014 near the Northwestern Part of the Chilian Coast.* Journal Science of Tsunami Hazards V.40,N.2,pp.83-100.
33. Wells D.L., Coppersmith K.J. (1994), *New empirical relationships among magnitude, rupture length, rupture width, rupture area, and surface displacement* // Bull. Seism. Soc. Am. Vol. 84. P. 974-1002 .

34. Sielecki A., Wurtele M. (1970), *The numerical integration of the non-linear shallow-water equations with sloping boundaries* // J. Comp. Phys. V.6, P.219-236.
35. Voltzinger N.E., Klevanny K.A., Pelinovsky, E.N. Long-wave dynamics of the coastal zone, Leningrad: Gidrometeoizdat, 1989.- 272 p
36. Mazova, R.Kh. (1984). *On the approximate boundary conditions at the shoreline, convenient for the numerical calculation of the run-up of tsunami waves* // in the book: Generation of tsunami waves and the emergence of waves on the coast, (Radio and Communication Press, Moscow, USSR), 54-57.
37. Pelinovsky E.N., Mazova R.Kh. *Exact analytical solutions of nonlinear problems of tsunami wave runup on slopes with different profiles* // Natural Hazards V.6, P.227-241, 1992.
20. Dogan, G. G., Annunziato, A., Papadopoulos, G. A., Guler, H. G., Yalciner, A. C., Cakir, T. E., et al. (2019). The 20th July 2017 Bodrum-Kos Tsunami field survey. Pure and Applied Geophysics, 176, 2925–2949. https://doi.org/10.1007/s00024-019-02151.
37. Papadopoulos, G.A.; Gràcia, E.; Urgeles, R.; Sallares, V.; De Martini, P.M.; Pantosti, D.; González, M.; Yalciner, A.C.; Mascle, J.; Sakellariou, D.; et al. (2014), Historical and pre-historical tsunamis in the Mediterranean and its connected seas: Geological signatures, generation mechanisms and coastal impacts. Mar. Geol., 354, 81–109.
38. Heidarzadeh, M.; Necmioglu, O.; Ishibe, T.; Yalciner, A.C. Bodrum–Kos (Turkey-Greece) (2017), Mw6.6 earthquake and tsunami of 20 July 2017: A test for the Mediterranean tsunami warning system. Geosci. Lett., 4, 31.
39. Cankaya ZC, Suzen ML, Yalciner AC, Kolat C, Zaytsev A, and Aytore B.(2016), A new GIS-based tsunami risk evaluation: MeTHuVA (METU tsunami human vulnerability assessment) at Yenikapı, Istanbul. Earth, Planets and Space, 68(1), 133.
40. England, P, Howell, A, Jackson, J, and Synolakis C, (2015), Palaeotsunamis and tsunami hazards in the Eastern Mediterranean. Philosophical Transactions of the Royal Society A: Mathematical, Physical and Engineering Sciences, 373(2053), p. 20140374.
41. Okal, EA, Synolakis, CE, Uslu, B, Kalligeris, N, and Voukouvalas, E, (2009), The 1956 earthquake and tsunami in Amorgos, Greece. Geophysical Journal International, 178(3), 1533-1554.
42. UNESCO, 2014. International Tsunami Survey Team (ITST) Post□Tsunami Survey Field Guide. 2nd Edition. IOC Manuals and Guides No.37, Paris: UNESCO 2014 (English).
44. Yalciner, AC, Imamura, F, and Synolakis C. (2008). *Amplitude evolution and eunup of long waves; Comparison of experimental and numerical data on a 3D complex topography*. In Advanced Numerical Models for Simulating Tsunami Waves and Runup (ed. by: Philip L-F Liu, H.Yeh, C.Synolakis): Advances in Coastal and Ocean Engineering: V10, pp.243-247. https://doi.org/10.1142/6226.
45. Soloviev S.L., Gu Ch.N., Kim Kh.S., Solovieva O.N., Shchetnikov N.A. Tsunami in the Mediterranean. 2000 BC - 1991 (Moscow: Scientific world, 1997).

ISSN 8755-6839

SCIENCE OF **TSUNAMI HAZARDS**

Journal of Tsunami Society International

Volume 40 **Number 3** **2021**

TSUNAMI FAULTING MODEL ANALYSIS FOR THE 30 OCTOBER 2020 NORMAL EARTHQUAKE OCCURRED IN IZMIR-TURKEY

Madlazim[1,*], Eko Hariyono[1], Muhammad Nurul Fahmi[1], Dyah Permata Sari[1]

[1] Department of Physics, Faculty of Mathematics and Natural Sciences, Universitas Negeri Surabaya, Surabaya 60231, Indonesia
*Correspondence: madlazim@unesa.ac.id

ABSTRACT

This study aims to analyse the M_w 7.0 normal faulting type earthquake that occurred on October 30, 2020, in Izmir-Turkey. After the earthquake, a tsunami was followed with a maximum water level of 3.8 meters in the Aegean Sea. The used method in this study is the measurement of the tsunami faulting model parameters by using a direct procedure. The measured tsunami parameters are the dominance period (T_d), rupture duration (T_{dur}), and rupture duration more than 50 seconds (T_{50Ex}) as well as the results of the multiplication between T_d and T_{50Ex} (T_dT_{50Ex}). In this study, we used seismogram velocity of vertical component recorded by the Global Seismographic Networks (GSN) network stations and the GEOFON (GE) network with an epicenter distance of 0 to 40°, totaling 66 seismic stations. Based on the measurement results, the tsunami discriminants T_{dur} = 65.11 seconds, T_d = 9.28 seconds, T_{50Ex} = 1.43 and T_dT_{50Ex} = 13.27 seconds > 10 seconds (threshold). The value of the tsunami discriminants T_dT_{50Ex} that exceeds this threshold strengthens that the normal type earthquake is the cause of the tsunami.

Key words: *Normal earthquake, dominant period, rupture duration, rupture duration more than 50 seconds, tsunami faulting model.*

Vol. 40, No. 3, page 196 (2021)

1. INTRODUCTION

Worldwide tsunamis caused by earthquakes are more often caused by reverse fault earthquakes than those caused by normal earthquakes and strike-slip earthquakes. This is understandable because the vertical displacement component of a reverse earthquake is much larger than that of a normal and strike-slip earthquake. Large tsunamis are rarely generated by strike-slip or normal-faulting events. This is because strike-slip faults that trigger local tsunamis may only be correlated with the size of the localized seafloor deformation insignificantly (Gusman, et al., 2017; Lay et al., 2017). However, records of past tsunamis initiated by strike-slips are reported as, for example, in 1906 in San Francisco, California (Ma, et al., 1991; Thatcher, et al., 1997) and in 1994 in Mindoro, Philippines (Imamura et al., 1995). These examples are complemented by relatively recent events in 2016 in Kaikoura, New Zealand (Power et al., 2017; Ulrich, et al., 2019a), and in Palu on 28 of September 2018, Indonesia (Carvajal, et al., 2019; Ulrich et al., 2019b; Madlazim, et al., 2020). From the total 35 events used in the study, Madlazim et al. (2021), found that 74% (26 events of normal and strike-slip earth quakes), have been validated to cause tsunamis, of which 11 strike-slips and 15 normal earthquakes. Therefore, these two mechanisms can be a potential source of tsunami generation.

On the coast near the Aegean Sea, densely populated coastal areas have been affected by several tsunamis in the past, some of them were devastating (Altinok et al., 2011; Altinok & Ersoy, 2000; Ambraseys & Synolakis, 2010; Papadopoulos et al., 2014; Dogan et al., 2021). The most famous tsunami in this region was the 1956 Amorgos event (M_w 7.8) which caused a maximum run up water level of up to 25 m (Beisel et al., 2009; Okal, el al., 2009). More recently, the eastern Aegean Sea was the site of two tsunamis that followed by the occurrence of earthquakes measuring M_w 6.3 and 6.6 respectively in June and July 2017. Both at Lesvos on 12 of June 2017 and at Bodrum-Kos on July 212020,, 2017, which was followed by a tsunami from a medium-magnitude earthquake in the region. The latter event caused a significant impact on the southern coast of the Bodrum Peninsula in Turkey and the Port of Kos on Kos Island in Greece (Dogan et al., 2019, 2021).

A strong earthquake that occurred on October 30, 2020, with a magnitude of M_w 6.6 has hit Samos Island in Greece and Izmir Province in Turkey in the eastern Aegean. Based on information from the Kandilli Observatory and Earthquake Research Institute (KOERI) and Anadolu Agency that this Tsunami occurred after the earthquake and caused significant damage in Cesme and Seferihisar Districts in Izmir and the coast of the Samos Island, and resulted in one victim and several injured people due to the tsunami on the Turkish side. The national tsunami warning centre and tsunami service for the North-East Atlantic, the Mediterranean Ocean Tsunami Warning System and the Ocean Connected System (NEAMTWS), issues a tsunami warning 11 minutes after the earthquake (Dogan et al., 2021). In this paper, we present the results of the velocity seismogram of vertical component data analysis from the 30 of October 2020 earthquake that occurred in Izmir-Turkey to confirm that the tsunami was caused by the earthquake. Our results include: measurement of dominance period (T_d), rupture duration (T_{dur}), and rupture duration more than 50 seconds (T_{50Ex}) as well as the results of the multiplication of T_d and T_{50Ex} (T_dT_{50Ex}). Next, we discuss the findings in this study to deeply understand the behavior of the tsunami and its impact on nearby coastal areas.

2. TECTONIC SETTING

The cause of the Turkish earthquake on October 30 include the many shifts in tectonic plates and other seismic forces that play a major role in the region for frequent earthquakes (National Geographic, 31/10/2020). An earthquake with an earlier estimated magnitude of 7 struck near the city of Izmir in 1688. It changed the landscape so much that the surface dropped by more than a foot, and the shaking buildings collapsed and started fires and killed up to 16,000 people. The eastern Aegean Sea region is characterized as dominated by dip-slip extensional tectonic (Aktar, et al., 2007). The Aegean Sea coasts of Turkey and Greece were struck by a moderate tsunami on 30 October 2020, which was generated by an M_w 7.0 normal-faulting earthquake (Fig. 1).

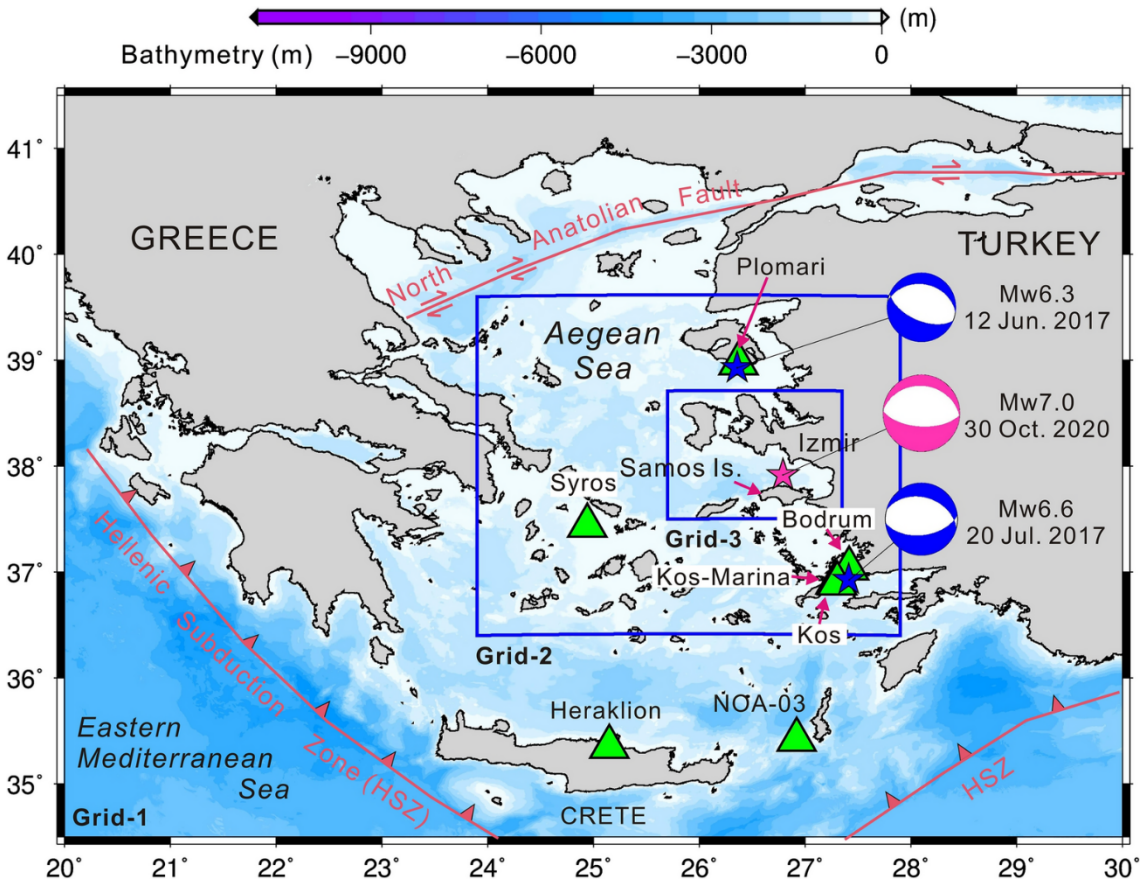

Figure 1. Tectonic setting of the Aegean Sea region and the epicentral area of the 30 October 2020 Mw 7.0 earthquake. Data of epicenters and focal mechanisms belong to the United States Geological Survey (USGS) earthquake catalogue. Green triangles show the locations of tide gauges. The blue boxes show the geographical areas of Grid-2 (spatial resolution = 10.8 arc-sec) and Grid-3 (spatial resolution = 3.6 arc-sec), which form the nested grid system that we used for numerical modelling of the tsunami (Heidarzadeh et al., 2021).

These include faults trending E–W according to their area extending in the N–S direction and showing a dextral (right-lateral) or sinistral (left-lateral) component (Emre, et al., 2011; Tan et al., 2014; Tepe & Sözbilir, 2017). Therefore, the tsunami threat in the study area is mainly associated with the dominant normal fault which indicates a high potential risk for the coastal area. On October 30, 2020, 12:51 UTC (14:51 local time), an underwater earthquake (M_w 6.6) occurred in north of Samos Island, Greece, and off the coast of Seferihisar-Izmir, Turkey, with an epicenter (37.88 N , 26.70 E) at a depth of 15 km (AFAD, 2020). More than 4600 aftershocks have occurred by the end of November 2020, 50 of them had a magnitude of M_w 4.0. The largest was with a magnitude of M_w 5.1 occurred at 16:14 (UTC), about 4 hours after the earthquake, about 10 km southeast of the epicenter at a depth of about 7 km. From the conjugate-type aftershock distribution between the Dilek Peninsula (DP) in Turkey and the northern Greek Island of Ikaria, about 80–100 km long rupture crack in the E–W direction is clearly visible in four segments with visible seismic gaps. Three segments are located in the northern part of Samos, while the eastern part of the swarm is aligned in the NNE–SSW direction, which is parallel to the Buyuk Menderes Graben (BMG) alignment. north of Kusadasi Bay (KB) and western part of Samos reveal a diffuse type of seismic activity (Dogan et al., 2021).

3. METHOD

There are two models of earthquake faults that have been used to explain the source of earthquakes.

Examination of the first examine earthquake faulting model: This theory explains the relationship between the strength (magnitude, M_w or seismic moment, M_0) of the earthquake source and the fault length, L, fault width, W, slip, D and shear modulus, as written in the equation M_0 = LWD. This model inspired seismologists that M_0 or M_w could be used as an early warning for earthquakes and tsunamis. The use of M_w or M_0 based on this model for earthquake early warning is quite accurate, but for tsunami early warning it still needs to be evaluated. The second model is the tsunami faulting model. After finding that the earthquake faulting model was not accurate for tsunami early warning, Lomax & Michelini (2011) developed a tsunami faulting model inspired by Satake's (1994) theory. This model provides the basis that not all earthquakes with a moment magnitude, M_w > 7 cause tsunamis because tsunami events still depend on the parameters of rupture length (L) and rupture width (W). This model also illustrates that the longer the earthquake rupture (L), the shallower the depth (z) of the earthquake centre. This can be explained based on the relationship between depth, density of the earth's medium and the shear modulus. The shallower the earth medium, the sparser the density and the smaller the value of the shear modulus, so that the rupture length is greater for certain earthquakes. The rupture length (L) is proportional to the rupture duration (T_{dur}). The rupture length is difficult to be measured directly, while T_{dur}, T_d and T_{50Ex} can be measured directly from a seismogram,

so tsunami early warning is very possible by using the tsunami parameters T_{dur}, T_d and T_{50Ex}. Threshold T_d 10 s, T_{dur}=65 s, T_{50Ex}, T_d*T_{dur}= 650 s^2 and T_d*T_{50Ex}= 10 s (Madlazim, 2013; Madlazim, et al. 2015). If the measurement results of the tsunami parameters exceed the threshold, then the earthquake has the potential to cause a tsunami.

3.1. *Rupture Duration of* P Wave (T_{dur})

High-frequency seismograms contain a larger number of P wave phase groups, so that the search for earthquake rupture duration represented by P wave groups fulfills the representative requirements in estimating the wave rupture duration for P tele-seismic earthquakes (Lomax & Michelini, 2009c). The algorithms used to estimate the rupture duration of a regional earthquake seismogram are: (1) providing a seismogram of the vertical component of the ground motion velocity in miniseed format as raw data; (2) applying a 4-pole and a 5–20 Hz Butterworth band-pass filter to obtain a vertical seismogram recording speed on HF for each Indonesian local station network; (3) converting the HF seismogram into velocity-squared envelopes to get the rms amplitude; (4) picking the arrival time of the P wave automatically on the HF seismogram; (5) measuring the time delay after the arrival of the P wave for 90%($T^{0,9}$), 80%($T^{0,8}$), 50%($T^{0,5}$) and 20% ($T^{0,2}$) of the peak value; and (6) calculating the rupture duration, T_{dur} for that station by using the equation:

$$T_{dur} = (1 - w)T^{0.9} + wT^{0.2} \quad (1)$$

with,

$$w = \left[\left(T^{0.8} + T^{0.5}\right)/2 - 20\right]/40\ s \quad (2)$$

and the value of w is constrained $0 \leq w \leq 1$ (Lomax & Michelini, 2009a) ; (7) plot $T^{0,2}$, $T^{0,5}$, $T^{0,8}$, $T^{0,9}$ and T_{dur} in the seismogram.

3.2. *Rupture Duration of* P Wave (T_{dur})

First of all, calculate the time domain (tc) by using the following equation :

$$\tau_c = 2\pi \int_{T_2}^{T_1} v^2(t)dt / \int_{T_2}^{T_1} \acute{v}^2(t)dt \quad (3)$$

(Nakamura, 1988; Wu & Kanamori, 2005: Lomax & Michelini, 2013)

With T_1 = 0 seconds (P onset) and T_2 = 55 seconds for tele seismic earthquake seismograms (Lomax and Michelini, 2009). Detailed steps of T_d estimation are as follows: (1) preparing raw earthquake data records from the vertical velocity component of broadband seismogram in a miniseed format, (2)

applying 4-poles and a corner frequency of 0.05 Hz Butterworth band pass filter to obtain the high-frequency, vertical component of velocity records for each seismic station; (3) picking *P*-wave arrival times automatically at the high-frequency, vertical-velocity seismogram; (4) integrating the seismogram and comparing it with vertical acceleration component of broadband seismogram times 2π of arrival times of *P*-waves automatically picked up from the vertical-velocity records on the high-frequency seismogram; and (5) the final results were values of T_d.

3.3. Exceed Duration More Than 50 Seconds (T_{50Ex})

T_{50Ex} estimation was carried out by using a direct procedure for tele seismic earthquakes, namely (1) filtering the seismogram velocity of vertical component by using a high frequency (1–5 Hz) Butterworth filter, (2) automatically picking P wave arrival times, (3) calculating rms amplitude (Ar) and T_{50}, (4) calculating T_{50Ex} which is the ratio between T_{50}/A_r (Lomax & Michelini, 2009a). Furthermore, the equations generated from the faulting tsunami model are integrated into the Jokotingkir software (Madlazim, 2017).

4. FAULTING MODEL APPLICATION FOR THE 30 OCTOBER 2020 EARTHQUAKE IN TURKEY

Measurement of three tsunami parameters from the faulting tsunami model (T_{dur}, T_d, and T_{50Ex}) for the M_w 7.0 normal faulting type earthquake that occurred in Turkey on October 30, 2020 by using seismogram velocity of vertical component data recorded by 61 to 64 seismic stations on the GSN network and GE with a regional epicentral distance of 4° to 40° as shown in Figure 2.

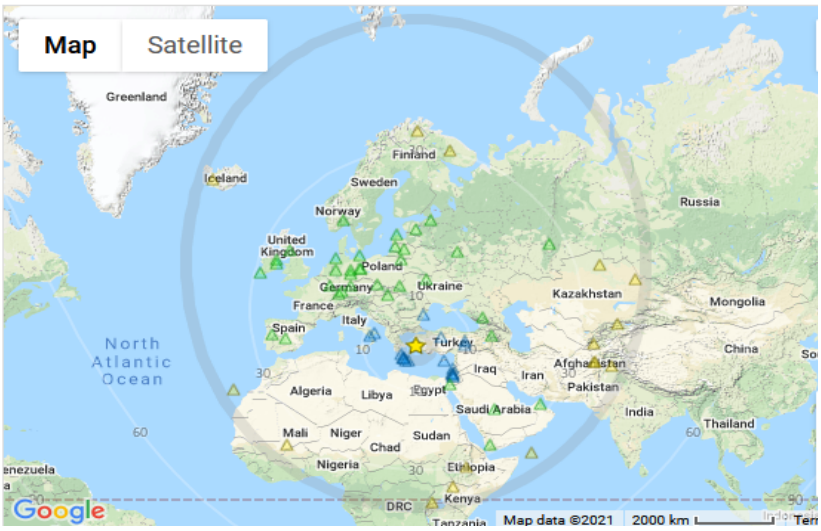

Figure 2. Distribution of seismic stations on the GSN network (green) and GE network (blue) and the epicenter of the M_w = 7 earthquake that occurred in Turkey on October 30, 2020.

5. RESULTS AND DISCUSSION

The results obtained in this study are the results of measuring three tsunami parameters from the tsunami faulting model (T_{dur}, T_d, and T_{50Ex}) for the M_w 7.0 normal faulting type earthquake that occurred in Turkey on October 30, 2020. From the results of the tsunami parameters calculation by using software Jokotingkir (Madlazim, 2017) whose real time application system can be accessed at http://predik-tsunami.unesa.ac.id/www/, the results are as shown in Table 1 below.

Table 1. Result of tsunami parameters calculation by using Joktingkir software

Tsunami Parameter	Number of Used Station	Value	Threshold	Decision
T_{dur}	61	65.11 s	50 s	-
T_d	64	9.28 s	10 s	-
T_{50Ex}	63	1.43	1	-
T_dT_{50Ex}	-	13.28 s	10 s	Tsunami

The number of stations used by each tsunami parameter is different because there are seismograms that do not meet the minimum requirements for each seismogram recorded by these seismic stations. Almost all tsunami parameter values exceed the threshold value, except for the dominant period (T_d) which is slightly smaller than the threshold. For the purposes of predicting a tsunami 4 minutes after the earthquake, T_{dur} is represented by T_{50Ex} because the computational T_{50Ex} turns out to be more accurate (Lomax & Michelini, 2013). However, the discriminant tsunami (T_dT_{50Ex}) exceeds the threshold, so it can be concluded that the M_w 7.0 earthquake is a normal faulting type. The one occurred in Turkey on October 30, 2020, was caused by the seismic energy of the earthquake, not a landslide or others (Dogan et al., 2021). This evidence confirms that normal fault earthquakes can cause tsunamis (Lomax & Michelini, 2013; Madlazim et al., 2021). The tsunami caused by this earthquake can also be validated from the Tsunami Event Validity (TEV) published at http://dx.doi.org/10.7289/V5PN93H7.

Large shallow earthquakes produce the most destructive tsunamis where the epicenter is on a fault line along the seabed. Tectonic subduction and tectonic plate boundaries are areas that have the most potential to cause tsunamis. These collisions of tectonic plates in these highly seismic regions cause large earthquakes when the plates are moving and passing one another, tilting, offsetting, or displacing large areas of the ocean floor from just a few kilometers to 1,000 or more. This sudden,

large vertical displacement of the seabed disturbs the sea level and generates a destructive tsunami as the water is displaced. The earthquake lifts or lowers the seabed. A tsunami can occur when an earthquake causes a sudden vertical deformation of the seabed, displacing the overlying water from its equilibrium position. When a reverse earthquake moves suddenly, a tsunami can be generated if it is associated with a destructive or convergent plate boundary. This is due to the vertical component of the movement and sudden displacement.

Movements on normal faults (normal earthquakes) can also cause seafloor displacement, but if the ground moves from side to side, not much will happen to the water. Because the size of such an event is usually too small to produce a large tsunami. Conversely, if the land moves up or down, it displaces a large body of water. As the water tries to equalize itself, this displaced water will try to adjust itself in the form of waves. Earthquakes associated with subduction zones are very effective in generating tsunamis. Although most tsunamis are caused by underwater earthquakes, it should be noted that not all underwater earthquakes cause tsunamis: typically, an earthquake must be greater than 7.0 on the Richter scale in order to produce a destructive tsunami. Only from this intensity upwards, it is enough energy released to rapidly displace enough water to create a tsunami and the earthquake must have the epicenter near the earth's surface. The abnormally slow deformation (represented by rupture duration, dominant period, and rupture duration more than 50 seconds) at the earthquake tsunami source may be a manifestation of the weak zone viscoelasticity below the deep trench boundary.

Heidarzadeh et al., 2021 described that the arrival times of the maximum tsunami wave were up to 14.9 h after the first tsunami arrivals at each station. The duration of tsunami oscillation was from 19.6 h to > 90 h at various tide gauges. Spectral analysis revealed several peak periods for the tsunami; we identified the tsunami source periods as 14.2–23.3 min. The weak zone implied by large normal earthquakes such as the October 30, 2020, Turkish earthquake and other normal earthquakes may be the result of heating friction at the interface between boundaries of lithosphere (Kanamori, 1972). The structure here can be modeled by the thin lithosphere which is thickly lined in the weak zone. This structure offers an explanation, via speculative one, for such a slow earthquake (rupture duration exceeding the threshold). The thin lithosphere above the weak zone can rupture, possibly under its own weight, causing a tsunami.

Figures 3, 4, and 5 are Schematic of a single-station, each of which describes the process of measuring the rupture duration (T_{dur}), dominant period (T_d), and rupture duration more than 50 s (T_{50Ex}) processing for the 2020.10.30, M_w = 7.0, Dodecanese Island, Greece earthquake recorded by station GE.PSZ. at 11.19° GCD.

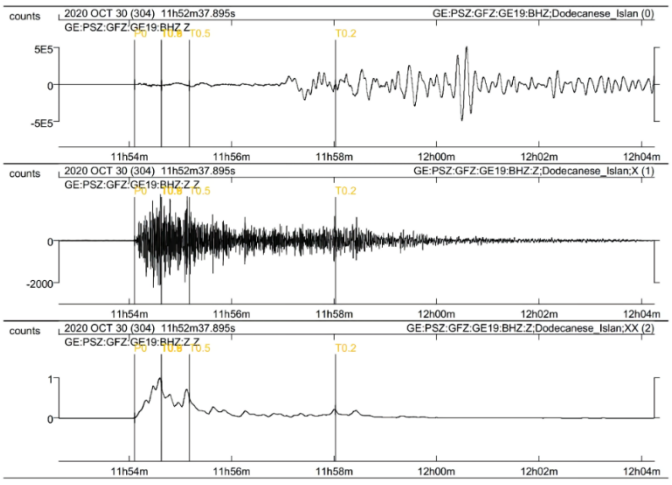

Figure 3. Schematic of a single-station, rupture duration (T_{dur}) processing for the 2020.10.30, M_w = 7.0, Dodecanese Island, Greece earthquake recorded by station GE.PSZ. at 11.19° GCD. Top panel represents raw, broadband velocity and the second panel is HF seismogram. The bottom panel is showing an estimation of T_{dur} = 82.69 s.

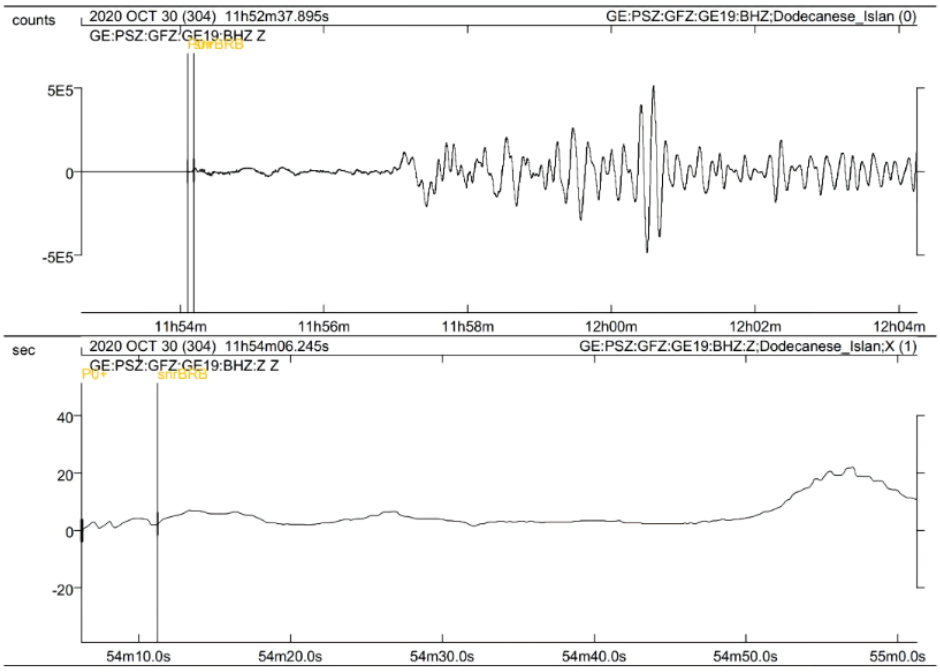

Figure 4. Schematic of a single-station, dominant period (T_d) processing for the 2020.10.30, M_w = 7.0, Dodecanese Island, Greece earthquake recorded by station GE.PSZ. at 11.19° GCD. Top panel represents raw broadband velocity. The bottom panel is showing an estimate of T_d = 22.35 s.

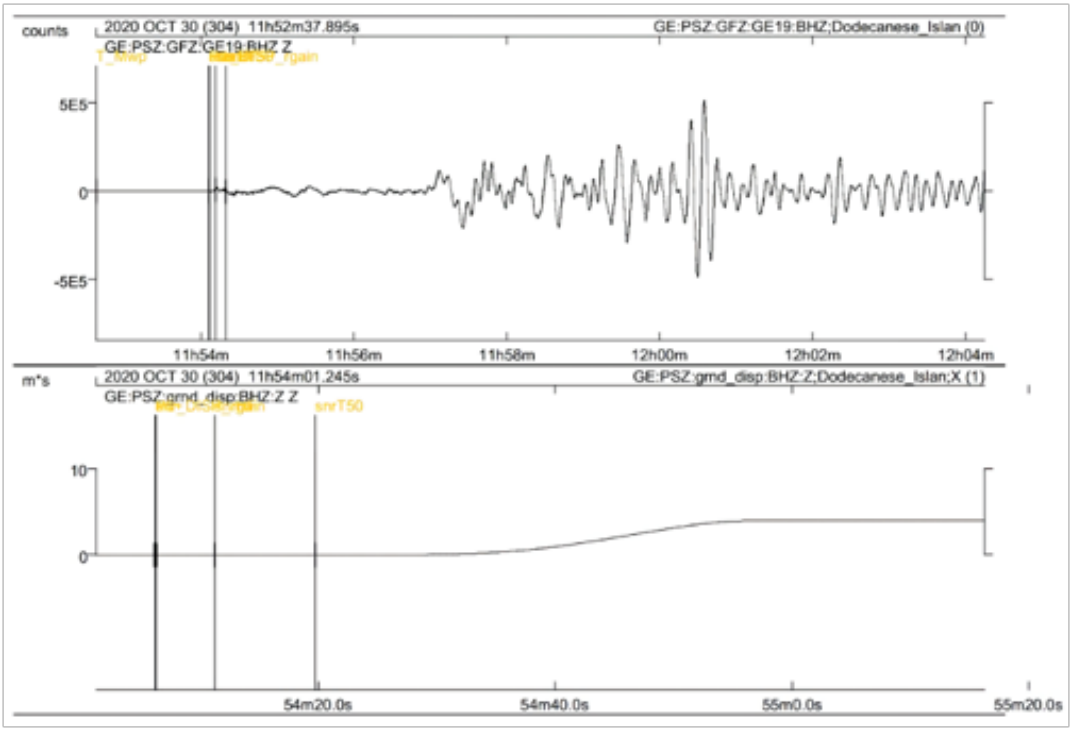

Figure 5. Schematic of a single-station, rupture duration more than 50 s (T_{50Ex}) processing for the 2020.10.30, M_w = 7.0, Dodecanese Island, Greece earthquake recorded by station GE.PSZ. at 11.19° GCD. Top panel represents raw broadband velocity. The bottom panel is showing an estimation of T_{50Ex} = 4.25 s.

6. CONCLUSIONS

Almost all tsunami parameter values exceed the threshold value, except for the dominant period (T_d) which is slightly smaller than the threshold. For the purpose of predicting a tsunami 4 minutes after the earthquake, T_{dur} is represented by T_{50Ex} because the computational T_{50Ex} turns out to be more accurate (Lomax, A. and Michelini, A., 2012). However, the discriminant tsunami (T_dT_{50Ex}) exceeds the threshold, so it can be concluded that the M_w 7.0 normal faulting type earthquake that occurred in Turkey on October 30, 2020, was caused by the seismic energy of the earthquake. Normal earthquakes can cause tsunamis because the thin lithosphere is thickly lined in the weak zone for very slow earthquakes (rupture duration, dominant period, and rupture duration exceeding the threshold). The thin lithosphere above the weak zone can rupture, possibly under its own weight, causing a tsunami.

ACKNOWLEDGEMENTS

The authors would sincerely like to thank the GEOFON GFZ and Incorporated Research Institutions for Seismology (IRIS) for which seismic data were freely available at http://eida.gfz-potsdam.de/webdc3/ and http://www.iris.edu/wilber3/find. This article is also beneficial from constructive reviews from two anonymous reviewers.

REFERENCES

AFAD (2020). Disaster and Emergency Management Authority (AFAD), Ministry of Interior, Ankara-Turkey. http://deprem. afad.gov.tr.

Aktar M, Karabulut H, Özalaybey S, Childs, D (2007). A conjugate strike-slip fault system within the extensional tectonics of Western Turkey. Geophysical Journal International 171(3): 1363–1375. https://doi.org/10.1111/j.1365-246X.2007.03598.x

Altinok Y, Alpar B, Özer N, Aykurt H (2011). Revision of the tsunami catalogue affecting Turkish coasts and surrounding regions. Natural Hazards and Earth System Science 11(2): 273–291. https://doi.org/10.5194/nhess-11-273-2011

Altinok Y, Ersoy Ş (2000). Tsunamis Observed on and Near the Turkish Coast. Natural Hazards 21(2): 185–205. https://doi.org/10.1023/A:1008155117243

Ambraseys N, Synolakis C (2010). Tsunami Catalogs for the Eastern Mediterranean, Revisited. Journal of Earthquake Engineering 14: 309–330. https://doi.org/10.1080/13632460903277593

Beisel S, Chubarov L, Didenkulova I, Kit E, Levin A, Pelinovsky E et al. (2009). The 1956 Greek tsunami recorded at Yafo, Israel, and its numerical modeling. Journal of Geophysical Research: Oceans 114(C9). https://doi.org/https://doi.org/10.1029/2008JC005262

Carvajal M, Araya-Cornejo C, Sepúlveda I, Melnick D, Haase JS (2019). Nearly Instantaneous Tsunamis Following the Mw 7.5 2018 Palu Earthquake. Geophysical Research Letters 46(10): 5117–5126. https://doi.org/https://doi.org/10.1029/2019GL082578

Dogan GG, Annunziato A, Papadopoulos GA, Guler HG, Yalciner AC, Cakir TE et al.2019). The 20 July 2017 Bodrum–Kos Tsunami Field Survey. Pure and Applied Geophysics 176(7): 2925–2949. https://doi.org/10.1007/s00024-019-02151-1

Dogan GG, Yalciner AC, Yuksel Y, Ulutaş E, Polat O, Güler I et al. (2021). The 30 October 2020 Aegean Sea Tsunami: Post-Event Field Survey Along Turkish Coast. Pure and Applied Geophysics 178(3): 785–812. https://doi.org/10.1007/s00024-021-02693-3

Emre Ö, Ozalp S, Duman TY (2011). 1:250,000 scale active fault map series of Turkey, I˙zmir (NJ 35-7) Quadrangle. In Serialnumber: 6. General Directorate of Mineral Research and Exploration, Ankara.

Gusman AR, Satake K, Harada T (2017). Rupture process of the 2016 Wharton Basin strike-slip faulting earthquake estimated from joint inversion of teleseismic and tsunami waveforms. Geophysical Research Letters 44(9): 4082–4089. https://doi.org/https://doi.org/10.1002/2017GL073611

Heidarzadeh, M., Pranantyo, I.R., Okuwaki, R. *et al.* Long Tsunami Oscillations Following the 30 October 2020 M_w 7.0 Aegean Sea Earthquake: Observations and Modelling. *Pure Appl. Geophys.* **178,** 1531–1548 (2021). https://doi.org/10.1007/s00024-021-02761-8

Imamura F, Synolakis CE, Gica E, Titov V, Listanco E, Lee, HJ (1995). Field survey of the 1994 Mindoro Island, Philippines tsunami. Pure and Applied Geophysics 144(3): 875–890. https://doi.org/10.1007/BF00874399

Kanamori H (1972). Mechanism of tsunami earthquakes. Physics of the Earth and Planetary Interiors 6(5): 346–359. https://doi.org/https://doi.org/10.1016/0031-9201(72)90058-1

Lay T, Ye L, Bai Y, Cheung KF, Kanamori H, Freymueller J et al. (2017). Rupture Along 400 km of the Bering Fracture Zone in the Komandorsky Islands Earthquake (MW 7.8) of 17 July 2017. Geophysical Research Letters 44(24): 12,112-161,169. https://doi.org/https://doi.org/10.1002/2017GL076148

Lomax A, Michelini A (2009a). Mwpd: A duration-amplitude procedure for rapid determination of earthquake magnitude and tsunamigenic potential from P waveforms. Geophysical Journal International 176(1): 200–214. https://doi.org/10.1111/j.1365-246X.2008.03974.x

Lomax A, Michelini A (2009b). Tsunami early warning using earthquake rupture duration. Geophysical Research Letters 36(9). https://doi.org/https://doi.org/10.1029/2009GL037223

Lomax A, Michelini A (2011). Tsunami early warning using earthquake rupture duration and P-wave dominant period: the importance of length and depth of faulting. Geophysical Journal International 185(1): 283–291. https://doi.org/10.1111/j.1365-246X.2010.04916.x

Lomax A, Michelini A (2013). Tsunami Early Warning Within Five Minutes. Pure and Applied Geophysics 170(9): 1385–1395. https://doi.org/10.1007/s00024-012-0512-6

Ma K-F, Satake K, Kanamori H (1991). The Origin Of The Tsunami Excited By The 1906 San Francisco Earthquake. Bulletin of the Seismological Society of America, 81(4): 1396–1397.

Madlazim (2017). Use of The Joko Tingkir Software for Rapid Determination of Tsunami Faulting Parameters Resulting From the Mw-7.8 Earthquake of March 2, 2016, in Southern Sumatra. Science of Tsunami Hazards 36(1): 41–48.

Madlazim (2013). Assessment of tsunami generation potential through rapid analysis of seismic parameters: Case study: Comparison of the Sumatra Earthquakes of 6 April and 25 October 2010. Science of Tsunami Hazards 32(1): 29-38.

Madlazim Prastowo T, Fahmi MN (2020). Estimation of rupture directivity, CMT and earthquake tsunami parameters and their correlation with the main source of the first tsunami wave, September 28, 2018. Science of Tsunami Hazards 39(4): 228–242.

Madlazim, Prastowo T, Fahmi MN, Sari DP, Melianda E, Koesoema S. (2021). Tsunamis from strike-slip and normal earthquakes and its relation with the product of dominant period and duration more than 50 seconds of earthquake P-wave. Science of Tsunami Hazards (Accepted).

Madlazim, Prastowo T, Hardy T (2015). VALIDATION OF JOKO TINGKIR SOFTWARE USING TSUNAMI IMPORTANCE. Science of Tsunami Hazards 34(3): 189–198.

Nakamura Y. (1988). On the urgent earthquake detection and alarm system (UrEDAS). In Proc. of the 9th World Conference on Earthquake Engineering; Tokyo-Kyoto, Japan.

Okal EA, Synolakis CE, Uslu B, Kalligeris N, Voukouvalas E (2009). The 1956 earthquake and tsunami in Amorgos, Greece. Geophysical Journal International 178(3): 1533–1554. https://doi.org/https://doi.org/10.1111/j.1365-246X.2009.04237.x

Papadopoulos GA, Gràcia E, Urgeles R, Sallares V, De Martini PM, Pantosti, D et al. (2014). Historical and pre-historical tsunamis in the Mediterranean and its connected seas: Geological signatures, generation mechanisms and coastal impacts. Marine Geology 354: 81–109. https://doi.org/https://doi.org/10.1016/j.margeo.2014.04.014

Power W, Clark K, King DN, Borrero J, Howarth J, Lane E et al. (2017). Tsunami runup and tide-gauge observations from the 14 November 2016 M7.8 Kaikōura earthquake, New Zealand. Pure and Applied Geophysics 174(7): 2457–2473. https://doi.org/10.1007/s00024-017-1566-2

Satake K (1994). Mechanism of the 1992 Nicaragua Tsunami Earthquake. Geophysical Research Letters 21(23): 2519–2522. https://doi.org/https://doi.org/10.1029/94GL02338

Tan O, Papadimitriou EE, Pabucçu Z, Karakostas V, Yörük A, Leptokaropoulos K (2014). A detailed analysis of microseismicity in Samos and Kusadasi (Eastern Aegean Sea) areas. Acta Geophysica 62(6): 1283–1309. https://doi.org/10.2478/s11600-013-0194-1

Tepe Ç, Sözbilir H (2017). Tectonic geomorphology of the Kemalpaşa Basin and surrounding horsts, southwestern part of the Gediz Graben, Western Anatolia. Geodinamica Acta 29(1): 70–90. https://doi.org/10.1080/09853111.2017.1317191

Thatcher W, Marshall G, Lisowski M (1997). Resolution of fault slip along the 470-km-long rupture of the great 1906 San Francisco earthquake and its implications. Journal of Geophysical Research: Solid Earth 102(B3): 5353–5367. https://doi.org/https://doi.org/10.1029/96JB03486

Ulrich T, Gabriel A-A, Ampuero, J-P, Xu W (2019a). Dynamic viability of the 2016 Mw 7.8 Kaikōura earthquake cascade on weak crustal faults. Nature Communications 10(1): 1213. https://doi.org/10.1038/s41467-019-09125-w

Ulrich T, Vater S, Madden EH, Behrens J, van Dinther Y, van Zelst I et al. (2019b). Coupled, Physics-Based Modeling Reveals Earthquake Displacements are Critical to the 2018 Palu, Sulawesi Tsunami. Pure and Applied Geophysics 176(10): 4069–4109. https://doi.org/10.1007/s00024-019-02290-5

Wu Y, Kanamori H (2005). Rapid Assessment of Damage Potential of Earthquakes in Taiwan from the Beginning of P Waves. Bulletin of the Seismological Society of America 95. https://doi.org/10.1785/0120040193.

ISSN 8755-6839

SCIENCE OF TSUNAMI HAZARDS

Journal of Tsunami Society International

Volume 40 Number 3 2021

BUSINESS PLAN DEVELOPMENT FOR SCIENTISTS: CASE STUDY TSUNAMI WARNING

Madlazim, M*. Fida Rachmadiarti, Masriyah, Sifak Indana, Dyah Permata Sari

Universitas Negeri Surabaya, INDONESIA

*Corresponding author:madlazim@unesa.ac.id

ABSTRACT

In order to start a company and commercialize a great technological innovation, it is necessary to develop an effective business plan. The present study proposes the scientific development of such a business plan named "Educational Design Research" (EDR). This EDR plan aims to produce a 2021-2025 methodology for the Faculty of Mathematics and Natural Sciences of the Surabaya State University to address, among other things, the analysis, design, preparation, evaluation, and final reporting, for use in issuing and implementing effectively tsunami warnings in Indonesia. At the design stage of this project, the researchers involved in the present study compiled a business plan based on theory, and provided examples of procedures that could be readily accessed, evaluated and implemented in issuing tsunami warnings. The business plan was developed in close cooperation and thorough discussions with other units of the Faculty of Mathematics and Natural Sciences of the University. The revised business document plan was subsequently provided to a consultant for additional evaluation, recommendations, and revisions. The results of the present study are in the form of a business plan document for adoption in more effective earthquake and tsunami warnings,using the "Jokotingkir" technology.

Keywords: *Business plan, tsunami warning, entrepreneurship, Jokotingkir, disability.*

1. INTRODUCTION

Developing a good business plan before implementing a company's business operations is essential for long-term success. Garcia, R., F., et al (2019) found evidence that the process of making a business plan resulted in highly valued entrepreneurial competencies, and whether the business plan was real or fictitious, it did not affect the level of entrepreneurial competence. Several researchers who have studied entrepreneurial competence are Man et al. (2002), and Bakkali et al. (2010). Indeed, rare research comes with knowledge of analyzing students' perceptions of the attainment of these competencies (Tounés et al., 2014). However, to the authors' knowledge, no studies have examined the effect of such perceptions on the achievement of the competencies in question. Therefore, further research is needed to identify the benefits of business plans in terms of developing entrepreneurial competencies, especially for scientists (Momete D. C., 2018).

The present study discusses key elements of a business plan approach which could help scientists reach realistic estimates of potential revenue, that could offset operational expenses of an effective management program of added protection from tsunamigenic hazards in Indonesia. As stated, in order to start a company and commercialize a great technological innovation, it is necessary to develop first an effective business-type plan. Especially, if investment capital and resources are needed - as in this case – the preparation of a proper operational document is needed, to validate the experience of those involved as it is done for business start-up companies. This approach is supported by the results of research by Kiznyte J., et al., (2016), in order to ensure that the goals of the company are viable and that there is an understanding of what needs to be done for a program to become successful. However, most scientists rarely have such experience in creating plan documents and most likely don't know how to properly structure them.

Therefore, by using a business-like approach, the present study focuses on the plan that is most relevant to innovations related to science, such as the "Jokotingkir" technology, which is an externally-focused business plan for start-up companies. Since every business plan is different, it should not be necessary to follow a certain rigid format in formulating, if changes may lead to better results. After all, the point of any business plan is to state what approach will lead to more successful outcomes. Thus, making a document look like a standard business plan is second to none. Whatever approach is used in formulating a plan of action, it is important to include all the necessary information, and this can also increase the entrepreneurial competence of scientists (Momete D. C., 2018). In the present paper, we focus on developing a business plan type of document using the Jokotingkir technology that can function for the effective dissemination of earthquake and tsunami warnings.

2. LITERATURE REVIEW

As indicated, a business plan is a typical part of entrepreneurship courses. In almost all entrepreneurship courses, a business plan is the typical end product. According to Katz (2014), it is an excellent task and method to increase the level of student learning related to entrepreneurship. According to Honig (2004), a business plan can be defined as a written document that describes a company's current and future profile; it is a maturation process that facilitates the progression from an idea to a final project. Evidence suggests that business schools teach business plans because they help current and future entrepreneurs manage activities that involve a high degree of complexity and uncertainty (Kahrs, 1995). Although there are different suggestions on how to build a business plan, most include the following (Blenker et al., 2006): description of the business area, description of the management team, description of market segments, marketing plan, business, organizational systems, implementation, assessment of risk, and funding. In general, as in business, a scientific plan should includes the following similar components:

(1) Company Review - A review of one to three sentences of the company description. The description should be to the point in order to effectively grab the reader's attention, then followed by a very brief description of the company and its organizational structure.

(2) Mission Statement - The company's mission statement must effectively state the company's goals. A mission statement must be written that will guide future strategy and high-level decision-making. A mission statement is not a marketing tool, but it should be written well.

(3) Management – This is an introduction of the management team, which sould provide some background information about involved individuals, highlighting their strengths as they relate to the business and their position in the organizational structure. A bad management team can easily repel investors, so it is important to include in the introduction all the positive aspects, making sure the management team looks good in addressing effectively the company's operating plan.

(4) Market Analysis – Analysis and formulation of market/user analysis precludes the understanding by scientists of the technology market generated from plan documents. This market analysis should provide information about the competition, obstacles, market size, trends, challenges, opportunities, and benefits that the marketing approach presents.

(5) Scientific Background – For people involved in the formulation of an effective plan, it is is important for them to have adequate technical knowledge and understanding of needed and specific technology for effective implementation. Since scientific products are highly technical, there is a need to demonstrate the procedures that will meet the identified goals. If possible, reference should be made to published literature. If a working prototype has been completed, some of the test results should be presented.

(6) Marketing Plan – Such a plan must discuss the means of promoting information dissemination and reiterate the benefits to designated recipients, as well as the means to help achieve the neeeded goals. Also included should be a projection of how the product – in this case concepts of disaster mitigation – should be presented in order to reach maximum response and achieve maximum effectiveness. Such approach must utilize all available channels of effective dissemination and on how managers of the plan must interact with the public.

(7) Operation Plan – This aspect of the plan should deal with the means by which the new technology will operate, in general, but also with emphasis on more important considerations.

(8) Projections – Such inclusion of future "financial plans", will indicate projected goals and should emphasize the need for added worthwhile investements and improvements. These projections will be different for each participant, and will be based on the project's development time, on how long it will take to effectively reach recipients, on how long its product life cycle will be, and other relevant factors. Revenue resources for effective implementation will always involve some guesswork, so attention should be given that the sure your cost estimations are very close. It is better to have a slightly worse, but defensible financial outlook.

(9) Long Term Vision – The plan sould include important long-term goals and expected achievements for life science start-up that are important to participating partners or investors. In order to build on the success of the earlier years, the plan should include careful long-term vision, and projections for expansion into new areas.

(10) Disclaimer - you need to include The plan must include a statement which must protect participants from potential liability. It will not be part of the full section but should included as an Appendix in smaller print at the end of the document's body. Basically, the disclaimer must state that some of the projections may be risky, not guaranteed, and that individuals or organizations they represent will not be liable if some of the information turns out to be somewhat incorrect (Hoyt, C. accessed from http://biobm.com/2011/06/business-plans- for-life-scientist-inventors/.)

3. METHOD

The design used to develop the business plan is named "Educational Design Research" (EDR) (Hogue, R.J., 2013). This EDR study is related to the motive of improving practice, which can be done mainly for the following goals:

1) Solving the problem: As stated in general terms, to reduce to some extent the gap between disciplines of STEM-related career.

2) Using acquired knowledge to create innovative work: This is achieved through the design, piloting and implementation of programs aimed at familiarizing instructors with the potentials of technology;

3) Improving the robustness and systematic nature of design practice: Establishing a set of design principles for implementing programs of instructor professional development to teach STEM-related topics through an inquiry-based approach by using specific technologies.

This EDR method adapted in this study aims to produce a technology Business Plan or resources' management for the Faculty of Mathematics and Natural Sciences, Surabaya State University for the years 2021-2025. As previously stated, the different stages of the EDR include and address the needs for analysis, design, preparation, evaluation, and reporting. At the design stage, the researcher-compiled business plan design is based on theory and on examples of business plans that were accessed. At the stage of preparing a business plan, and in close cooperation and discussions with other units of Surabaya State University, a plan was prepared. Subsequently, several of the inputs for revising the business plan document were provided for evaluation to the designated consultant, in order to revise it and improve its functionality.

4. RESULTS AND DISCUSSION

The results of the business plan document development in this study are presented as follows:

1) Executive Summary - A reminder of daily seismic activity in areas of various countries in the region or globally, that have the potential for earthquakes and tsunamis, which can result in both physical and non-physical losses in Indonesia. However, most of the risk of earthquakes and tsunamis can be reduced with proper planning and preparation. In addition to strengthening buildings and encouraging residents to prepare for potential earthquakes and tsunamis, the Jokotingkir's technology is now available to provide warnings in four (4) minutes after an earthquake strikes, and in approximately thirty (30) minutes before the first tsunami waves hit a coast. This technology consists of a seismometer detecting the earthquake waves, satellites receiving and transmitting the seismic data, a server receiving and processing the earthquake information, which by using the available Jokotingkir software, can analyze and evaluate the seismographic data, which subsequently disseminates the earthquake and tsunami parameters – as shown by the illustration below (Fig. 1).

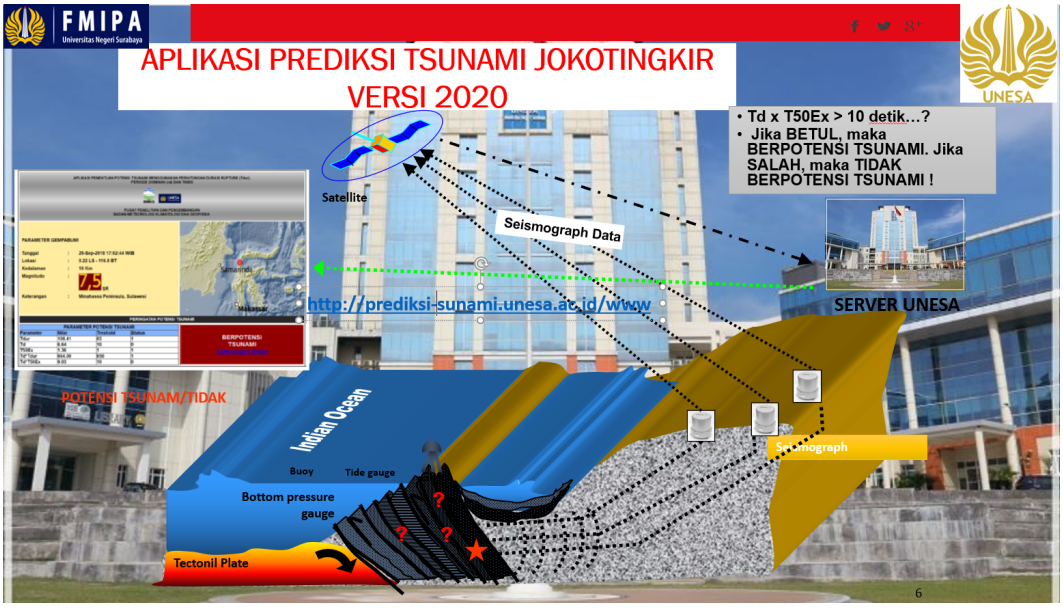

Figure 1. Performance scheme of the Jokotingkir technology

This Jokotingkir technology can also be used for people with special needs because it is equipped with a voice transmission capability which explains the earthquake and tsunami parameters, so that appropriate measures of disaster mitigation can be activated immediately. Furthermore, the Jokotingkir system can disseminate warnings, as well as instructions for evacuation or other nethods of public safety protection.

2. Vision-Mission Statement Vision: The main role and mission of the Jokotingkir technology is to create faster and more accurate earthquake and tsunami warnings and provide the best service to the potentially threatened public**.**

3. Management: The management of Jokotingkir's organization is carried out transparently with the PDCA (Plan, Do, Check, and Action) stages with the following organizational structure: Manager, Treasurer, Marketing, Production quality control division staff, and Information and communication system division staff. The management team is very compact and good in running the Jokotingkir Organization, as they have good training and understanding of its functions and goals.

4. Market Analysis and Strength: (a) Includes the Jokotingkir's technology which - as stated - provides a fast and more accurate information for earthquake early warnings and tsunami prediction and is equipped with voice notification about information on earthquake and tsunami parameters, making it more suitable for people with special needs. (b) Permits quick response to all interested parties, thus avoiding time-consuming bureaucratic delays. (c) Results in low overhead costs, thus offering recipients best possible price. (d) Provides close attention to all recipients's requests and needs. (e) Allows flexible handling of each each case and request. (f). Enjoys a good reputation by satisfied recipients.

Weaknesses include: (a) Lower ability of staff response for certain areas, (b) Limited capital availability, (c) Occasional cash flow shortages, (d) Less strategic location of managing office.

Opportunities consist of: (a) Improving efficiency in the working sector, (b) Good governmental support of our program and goals , (c) Absence of intense competition in the sector we are engaged in, (d) Low initial capitalization for the start of our operations.

Threats consist of: (a) Keeping up and quick adopting with the rapid development of technology in this field, (b) Changing competitors' strategies which threaten our position in this area. (c) Lack of banking interest in financing funding for the industry we are currently working on.

Target Market: The majority of Jokotingkir's technology target market is state or private institutions that have duties and responsibilities for earthquake and tsunami disaster mitigation.

Table 1. The results for assessment of tsunami potential by using M_w and τ_{50} discriminants.

Discriminant	Available (minutes after OT)	Threshold Value	True Warning (TW)			False warning (FW)		
			$TEV \geq 3$	$TEV < 3$	%**	$TEV \geq 3$	$TEV < 3$	%**
M_w	15	7.0	36	0	71%	13	2	29%
τ_{50} ex	4	10.0 s	39	2	76%	12	0	24%

*51 events classified; 39 occurrences have $TEV \geq 3$; ** percentage of True Warning or False Warning (Madlazim et al., 2021)

5. Scientific Background: The speed, accuracy and performance of the Jokotingkir technology have been tested through real-time earthquake data since 2012 until now. The Jokotingkir technology website can be accessed on the following website: (predict-tsunami.unesa.ac.id) and can also be accessed via android with the keyword (jokotingkir tsunami prediction). The results of the Jokotingkir technology trials have been published in several articles published in reputable international scientific journals (Table 1) (Madlazim et al., 2015; 2021). In addition, the Jokotingkir technology has been registered with IPR and patents.

6. Marketing Plan: In order to attract potential customers for the Jokotingkir Company and make it better known, there will be promotions from the social media. The special social media accounts will carry out promotions complete with websites containing promo-information and viral content. Because most likely users of the Jokotingkir technology are state institutions or seismological institutions, we intent to send brochures to all related institutions.

7. Operational Plan: The operating hours are from 08.00 am to 16.00 pm every day. A 24 - hour 7- day service is also set up specifically for online marketing staff.

8. Budgeting Projections Plan: The development of a financial plan - including identification of funding sources for one-time costs and ongoing costs – includes the development of a set of characteristic criteria and funding source for the Jokotingkir Earthquake Early Warning and Tsunami Prediction which involve: (a) A stable and sustainable source of income must be identified to finance ongoing operation and maintenance costs. (b) Costs for systems that are likely to increase in the future as a result of inflation, technological changes, and replacement of aging existing equipment. (c) Establishing an assessment of costs and benefits of the system. While access to the signal should not be restricted to only those who can pay, the costs for the system should still be borne by those who benefit**.**

9. Long Term Vision: This consists of: (a) Plans for expansion into new markets to build on the company's early years of success; (b) Adding new features of Jokotingkir technology to adapt technological developments to the needs of society.

The last business plan component of Jokotingkir's technology includes a Disclaimer, which states that the use of technology may have risks because earthquakes are one of the most common causes of tsunamis. Until now, there is no science and technology that can predict an earthquake at a certain time. This uncertainty applies to the Jokotingkir technology in predicting tsunami events.

The preparation of the ten components of a business plan from Jokotingkir's technology is based on the concept of a business plan for technological products produced by scientists (Garcia, R., F., et al., 2019; Kiznyte J., et al., 2016), and also on suggestions from a business consultant. All of the makers of these business plans are scientists, but who do not have specific experience in in business. However, by preparing business plans accompanied with inputs from experienced consultants, the level of achievement of entrepreneurial competence increases. Therefore, developing a business plan supports the development of entrepreneurial skills, perhaps because business planners have a special entrepreneurial-oriented attitude (Garcia, R., F., et al., 2019). With the production of a business plan document and increasing entrepreneurial competence, it is hoped that Jokotingkir's technology company can also improve the expected income generation.

6. CONCLUSIONS

A business plan document specifically for earthquake and tsunami early warning technology has been developed in close collaboration and coordination with a professional technology business consultant. This document consists of ten components of a business plan, namely Executive Summary, Vision-Mission Statement, Management, Market Analysis, Scientific Background, Marketing Plan, Operational Plan, Budgeting Projections Plan, Long Term Vision, and a Disclaimer (Disclaimer).

ACKNOWLEDGMENT

We thank the Directorate of Research and Community Service of the Indonesian Higher Education and the State University of Surabaya for supporting this research and its publication.

REFERENCES

Bakkali, C., Messeghem, K. and Sammut, S. (2010), "Les structures d'accompagnement à la creation d'entreprise à l'heure de la gestion des compétences", *Management et Avenir*, Vol. 9 No. 39, pp. 149-162.

Blenker, P., Dreisler, P. and Kjeldsen, J. (2006), "Entrepreneurship education: the new challenge facing the universities", Working Paper No. 2, Department of Management, Aarhus School of Business, Aarhus.

Garcia, R., F., Hernández-Lara A. B., Serradell-López E. Entrepreneurial competences in a higher education business plan course. *Education and Training* (2019) 61(7-8) 850-869. DOI: 10.1108/ET-04-2018-0090

Hogue, R.J. Epistemological foundations of educational design research. In *E-Learn: World Conference on ELearning in Corporate, Government, Healthcare, and Higher Education*; Association for the Advancement of Computing in Education (AACE): San Diego, CA, USA, 2013, pp. 1915–1922.

Honig, B. (2004), "Entrepreneurship education: toward a model of contingency-based business planning", *Academy of Management Learning and Education*, Vol. 3 No. 3, pp. 258-273.

Hwa Kho., PhD, MBAS. Chapter 4 - Business Plan
https://doi.org/10.1016/B978-0-323-67969-5.00004-6

Kahrs, K. (1995), Business Plans Handbook, International Thomson Publishing Company, Detroit, MI.

Katz, J.A. (2014), "Education and training in entrepreneurship", The Psychology of Entrepreneurship, Psychology Press, Mahwah, NJ, pp. 241-268.

Kiznyte J., Welker M., Dechange A. Applying Project Management Methods to the Creation of a Start-up Business Plan: The Case of Blendlee. *PM World Journal Applying Project Management Methods to Start-up Business Plan (2016)*

Madlazim,M., Tjipto Prastowo, Muhammad Nurul Fahmi, Ella Melianda, Soerja Kusuma. (2021). Effective tsunami early warning using the product of *P*-wave dominant period and source rupture duration more than 50 seconds. New Zealand Journal of Geology and Geophysics. Submitted

Madlazim, Tjipto Prastowo and Thomas Hardy. (2015). Validation of Joko Tingkir Software Using Tsunami Importance. *Science of Tsunami Hazards*, Vol. 34 No. 3, pp. 189-198.

Man, T.W., Lau, T. and Chan, K.F. (2002), "The competitiveness of small and medium enterprises: a conceptualization with focus on entrepreneurial competencies", *Journal of Business Venturing*, Vol. 17 No. 2, pp. 123-142.

Momete D. C. Book review: Engineering entrepreneurship from idea to business plan: A guide for innovative engineers and scientists. *International Small Business Journal: Researching Entrepreneurship (2018).*

Tounés, A., Lassas-Clerc, N. and Fayolle, A. (2014), "Perceived entrepreneurial competences tested by business plan pedagogies", *International Journal of Entrepreneurship and Small Business*, Vol. 21 No. 14, pp. 541-557.

ISSN 8755-6839

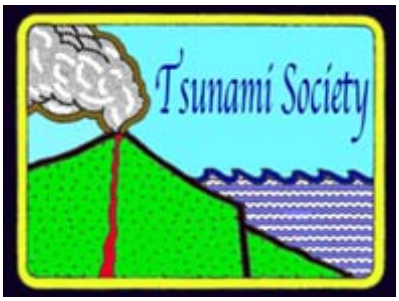

SCIENCE OF **TSUNAMI HAZARDS**

Journal of Tsunami Society International

Volume 40 **Number 3** **2021**

WWW.TSUNAMISOCIETY.ORG

TSUNAMI SOCIETY INTERNATIONAL, 1741 Ala Moana Blvd. #70, Honolulu, HI 96815, USA.

WWW.TSUNAMISOCIETY.ORG